

Rearmed Bifunctional Chelating Ligand for $^{225}\text{Ac}/^{155}\text{Tb}$ Precision-Guided Theranostic Radiopharmaceuticals— $\text{H}_4\text{noneunpaX}$

Published as part of the Journal of Medicinal Chemistry virtual special issue “Diagnostic and Therapeutic Radiopharmaceuticals”.

Luke Wharton, Hua Yang, María de Guadalupe Jaraquemada-Peláez, Helen Merkens, Gokce Engudar, Aidan Ingham, Helena Koniar, Valery Radchenko, Peter Kunz, Paul Schaffer, François Bénard, and Chris Orvig*



Cite This: *J. Med. Chem.* 2023, 66, 13705–13730



Read Online

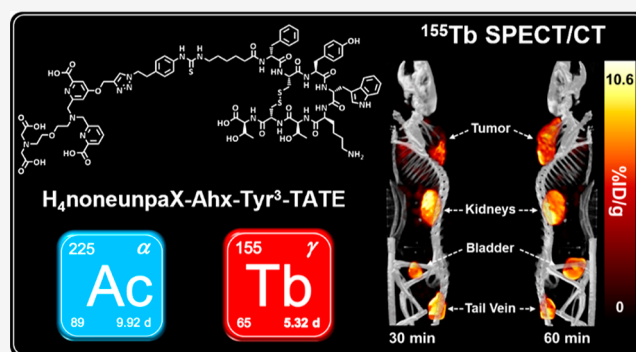
ACCESS |

Metrics & More

Article Recommendations

Supporting Information

ABSTRACT: Superior bifunctional chelating ligands, which can sequester both α -emitting radionuclides (^{225}Ac , ^{213}Bi) and their diagnostic companions (^{155}Tb , ^{111}In), remain a formidable challenge to translating targeted alpha therapy, with complementary diagnostic imaging, to the clinic. $\text{H}_4\text{noneunpaX}$, a chelating ligand with an unusual diametrically opposed arrangement of pendant donor groups, has been developed to this end. $\text{H}_4\text{noneunpaX}$ preferentially complexes Ln^{3+} and An^{3+} ions, forming thermodynamically stable ($\text{pLa} = 17.8$, $\text{pLu} = 21.3$) and kinetically inert complexes—single isomeric species by nuclear magnetic resonance and density functional theory. Metal binding versatility demonstrated in radiolabeling [^{111}In] In^{3+} , [^{155}Tb] Tb^{3+} , [^{177}Lu] Lu^{3+} , and [^{225}Ac] Ac^{3+} achieved high molar activities under mild conditions. Efficient, scalable synthesis enabled in vivo evaluation of bifunctional $\text{H}_4\text{noneunpaX}$ conjugated to two octreotate peptides targeting neuroendocrine tumors. Single photon emission computed tomography/CT and biodistribution studies of ^{155}Tb -radiotracers in AR42J tumor-bearing mice showed excellent image contrast, good tumor uptake, and high in vivo stability. $\text{H}_4\text{noneunpaX}$ shows significant potential for theranostic applications involving $^{225}\text{Ac}/^{155}\text{Tb}$ or $^{177}\text{Lu}/^{155}\text{Tb}$.



INTRODUCTION

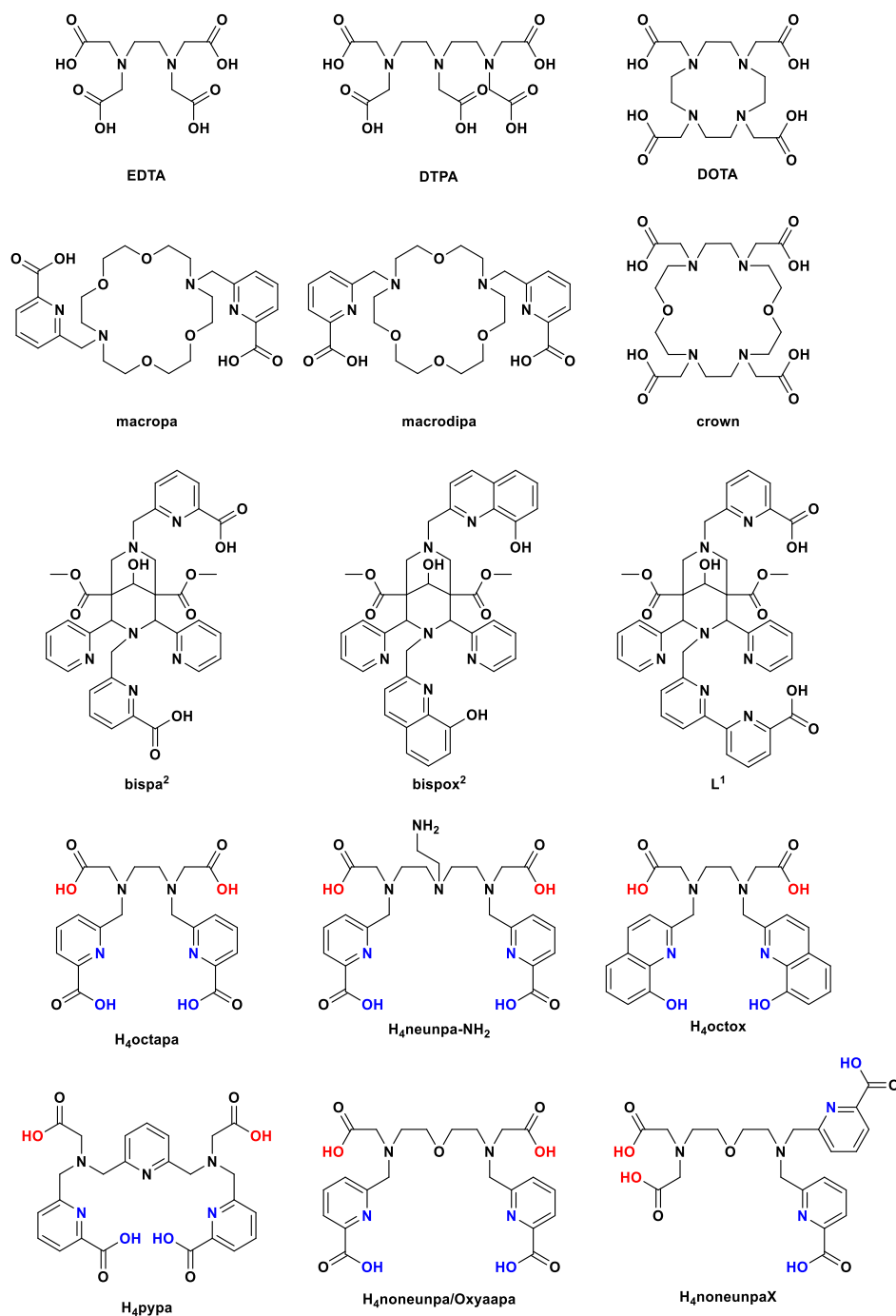
Metal ion chelating ligands are an essential component in numerous medical applications, including magnetic resonance imaging (MRI), heavy-metal detoxification, and nuclear imaging and therapy. Macrocyclic chelating ligands, such as DOTA,¹ Chart 1, are well-established as versatile platforms for sequestering different metal ions, forming thermodynamically stable and kinetically inert metal complexes; however, this is often at the expense of specificity/selectivity and requires high temperatures for metal ion incorporation.² Notably, significant research studies by the groups of Yang et al.^{3,4} and Wilson et al.^{5–13} have discovered macrocyclic ligands with expanded core frameworks (e.g., crown, macropa, macrodipa), which demonstrate more facile complexation characteristics and show interesting size–selectivity relationships. Furthermore, the bispidine class of chelating ligands, which have been extensively explored by Comba et al., have achieved favorable complexation properties with both large and small metal ions under mild conditions.^{14,15} Nonmacrocyclic chelating ligands, such as EDTA and DTPA, have been extensively investigated over decades for metal ion chelation owing to their fast complexation

kinetics under mild conditions, and their widespread application has been found in the medicinal sector in combination with thermally sensitive drug molecules;^{1,2} however, such chelators can exhibit fast decomplexation kinetics, leading to poor in vivo stability. With the growing interest in personalized patient-centered therapies, such as antibody–drug conjugates, there has been a sustained drive in this area of research toward the development of highly effective nonmacrocyclic, bifunctional chelating ligands to take advantage of these facile/biocompatible complexation kinetics. This goal has seen the growth of a new class of ligands incorporating stronger bidentate donor groups (e.g., picolates (pa),^{16–19} oxinates (ox)^{20,21}) appended to the terminal amines in

Received: June 26, 2023

Published: September 22, 2023



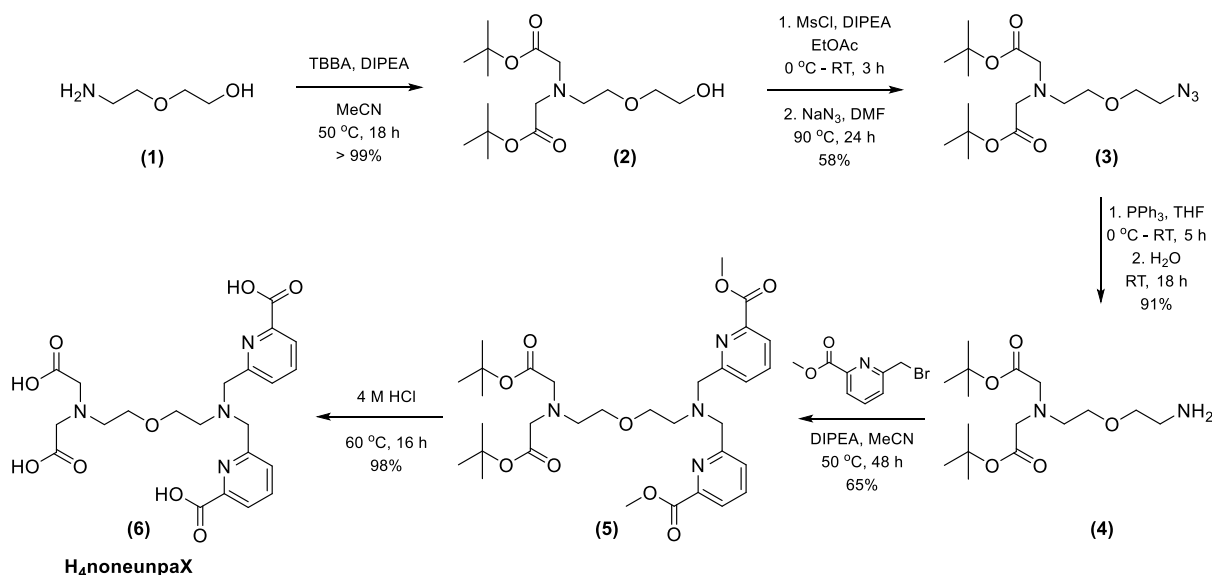
Chart 1. Chemical Structures of Discussed Ligands^{3–20,26,27}

nonmacrocylic scaffolds in place of one or more acetate groups, Chart 1.

With nonmacrocylic ligands bearing pairs of inequivalent pendent donor arms (e.g., two acetates, two picolates), two constitutional isomers exist by varying the substitution pattern at the backbone termini. A classical approach has involved arranging different pendent donor groups such that the terminal amines in a backbone are equivalent, with the same substitution pattern and thereby the same geometric constraints (e.g., H₄octapa, H₄neunpa-NH₂, H₄octox, H₄pypa, H₄noneunpa; Chart 1); to our knowledge, the influence of inverting the configuration to give a diametrically opposed arrangement wherein each pair of equivalent donor groups is bound to the

same terminal amine is yet to be investigated (i.e., H₄noneunpaX). In this context, H₄noneunpaX is designated the “*syn*”-regioisomer, from the Greek prefix meaning “together”, since each equivalent donor arm is bound to the same terminal nitrogen atom. Conversely, its constitutional isomer H₄noneunpa is designated the “*anti*”-regioisomer, from the Greek prefix meaning “opposite”, since each equivalent donor arm is bound to different backbone termini. While all ligands presented in Chart 1 have at least idealized C_{2v} symmetry, H₄noneunpaX is unique in this series with a linear backbone and each nitrogen atom differently substituted.

Given the inherent challenges in the directed synthesis of ligands with symmetric donor substitution and the require-

Scheme 1. Synthesis of H₄noneunpaX·4HCl·5H₂O from Commercially Available 2-(2-Aminoethoxy)ethan-1-ol, over 5 Steps with a Cumulative Yield of 33%

ments to often “break” symmetry in the pursuit of bifunctional derivatives for radiopharmaceutical applications,²² an assessment of the exact impacts of an inverted donor group arrangement on metal ion chelation is warranted. This inverted “*syn*” constitutional arrangement may give several advantages, particularly in regard to synthesis: protecting group strategies can be circumvented through rational synthetic design, and the incorporation of bifunctional handles within the core framework is synthetically more accessible, allowing for streamlined tuning of the pharmacokinetic profile of new radiopharmaceuticals.

In the context of nuclear medicine, significant improvements in the treatment of oncogenic disease have been achieved through the advent of peptide-based radiopharmaceutical agents targeting somatostatin receptor subtype 2 (SSTR2), which is commonly overexpressed in neuroendocrine tumors (NETs).²³ [¹¹¹In]In-DTPA-D-Phe-octreotide (OctreoScan) and [⁶⁸Ga]Ga-DOTA-TATE are two FDA-approved SSTR2 agonists used clinically to diagnose NETs.²³ Most notably, [¹⁷⁷Lu]Lu-DOTA-TATE (Lutathera) achieved clinical approval as a peptide receptor radionuclide therapy agent for the treatment of gastroenteropancreatic NETs in 2018;²⁴ however, as a result of the inherent nuclear decay characteristics of β^- -emitting radionuclides [low linear energy transfer, ~ 0.2 keV/ μm , long-range (0.5–10 mm)], treatment scope in this context is limited to primary tumor sites and large metastases.^{1,25}

Targeted alpha therapy (TAT) is a powerful tool for treatment of both primary and metastatic tumors, with ²²⁵Ac being one of the most prominent candidates for translation into clinical practice, owing to its compatible half-life ($t_{1/2}$ = 9.92 days) and the high therapeutic potency of its decay progeny (E_α = 5–9 MeV, 50–100 μm range).²⁸ For realization of this objective, high denticity, robust chelating ligands are required for stable chelation of the [²²⁵Ac]Ac³⁺ ion, which are further capable of sequestering imaging isotopes for diagnostics and assessment of patient suitability prior to radionuclide therapy. One potential imaging counterpart is the newly more-widely available radio-lanthanide ion [¹⁵⁵Tb]Tb³⁺, which shares similar bonding characteristics to [²²⁵Ac]Ac³⁺ [e.g., CN = 9; ionic radius = 1.095 Å (Tb³⁺), 1.220 Å (Ac³⁺)]^{29,30} and would be

suitable for single photon emission computed tomography (SPECT)/CT diagnostics owing to its low-energy gamma emissions [E_γ = 87 keV (32%), 105 keV (25%)] and comparable half-life ($t_{1/2}$ = 5.32 days).³¹ Additionally, ¹⁵⁵Tb is part of the so-called “terbium theranostic quartet”, encompassing radioisotopes ¹⁴⁹Tb, ¹⁵²Tb, ¹⁵⁵Tb, and ¹⁶¹Tb, in an unusually complete package comprising both positron emission tomography (PET) and SPECT imaging modalities as well as all three therapeutic decay types (α , β^- , Meitner-Auger electrons).^{32–34} Thus, combining different Tb³⁺ radioisotopes would provide a true theranostic radiopharmaceutical with identical pharmacokinetic and biodistribution properties.

With a focus on [²²⁵Ac]Ac³⁺ and *trans*-lanthanide ion chelation, we report H₄noneunpaX, a high-denticity chelating ligand with an unusual inverted donor group arrangement in which each backbone terminus bears a different pair of binding arms, two acetic vs two picolinic acids. Comprehensive assessment of this diametrically opposed constitutional arrangement on metal ion coordination has been undertaken by means of nuclear magnetic resonance (NMR) spectroscopy, mass spectrometry (MS), solution thermodynamic stability studies, density functional theory (DFT) calculations, and radiolabeling studies; also, comparisons to the related constitutional isomer H₄noneunpa/Oxyaapa^{19,27} have been assessed throughout. To further assess the utility of this approach, a bifunctional derivative of H₄noneunpaX was synthesized and conjugated to two structural analogues of Tyr³-octreotate (Tyr³-TATE) for targeting SSTR2-positive NETs. With the aim of seeking a suitable diagnostic partner to ²²⁵Ac therapy, the imaging potentials of the ¹⁵⁵Tb-labeled peptide conjugates were investigated through in vivo SPECT/CT with concurrent biodistribution studies in mice bearing AR42J tumor xenografts. Following a chemical curiosity-driven approach, we describe herein our investigation of a nonconventional aspect in chelate design and the unexpected advantages achieved, which may benefit the future development of ²²⁵Ac/¹⁵⁵Tb theranostic radiopharmaceuticals.

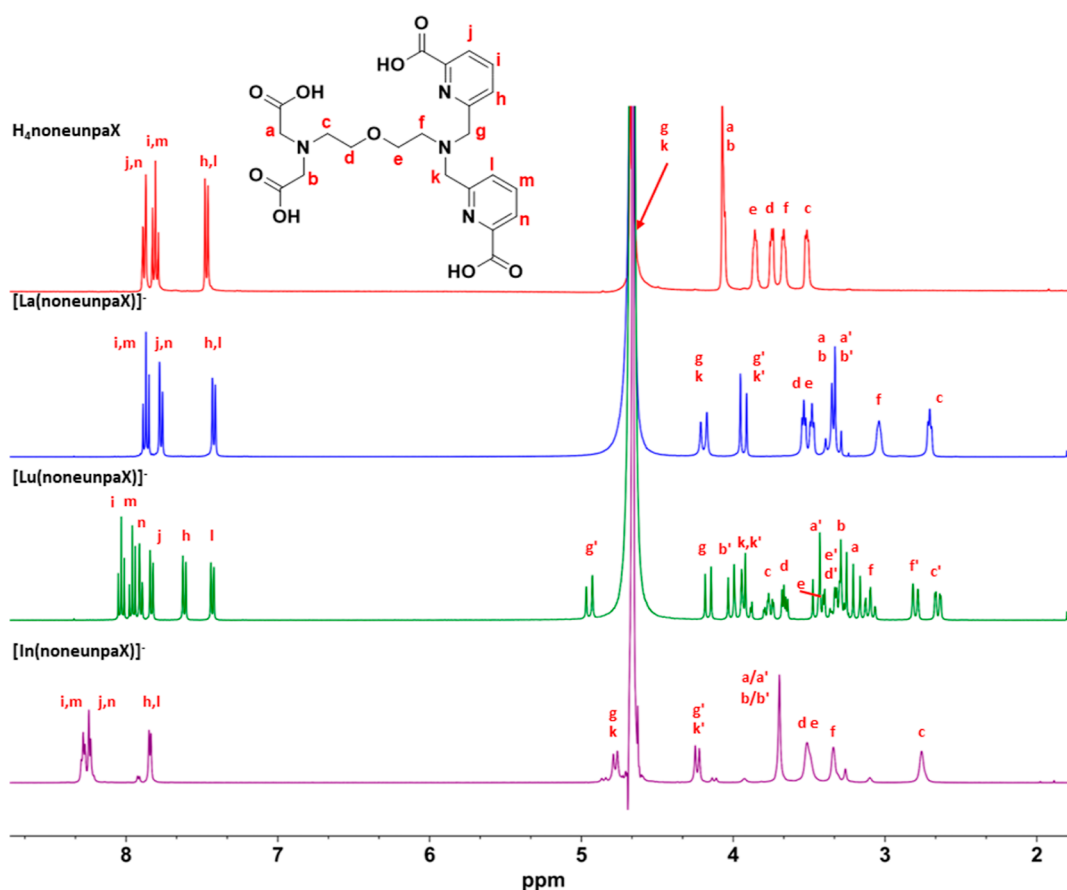


Figure 1. Stacked ^1H NMR spectra of $\text{H}_4\text{noneunpaX}$ and corresponding complexes of La^{3+} , Lu^{3+} , and In^{3+} (400 MHz, D_2O , 298 K, pD 7.0). $[\text{In}(\text{noneunpaX})]^-$ was characterized at pD = 4.5.

RESULTS AND DISCUSSION

Synthesis and Characterization. $\text{H}_4\text{noneunpaX}$ was prepared following the linear synthetic route outlined in Scheme 1, while the previously reported ligand $\text{H}_4\text{noneunpa}/\text{Oxyaapa}^{19,27}$ was synthesized using established procedures.¹⁹

The synthesis of $\text{H}_4\text{noneunpaX}$ proceeds through *N*-alkylation of commercially available 2-(2-aminoethoxy)ethan-1-ol (**1**) with *tert*-butyl bromoacetate (TBBA) under mild conditions to give di-*tert*-butyl ester **2** in high yields. Sequential mesylation of compound **2** followed by displacement with sodium azide proceeded cleanly to give the corresponding azide **3** in good yields. Diisopropylethylamine (DIPEA) was selected as an appropriate base for the mesylation of compound **2** in order to precipitate the HCl equivalent generated in the reaction and minimize formation of the chloride side product. Staudinger reduction of azide **3** generated the corresponding primary amine **4**, which could be used directly without additional purification. Subsequent *N*-alkylation of amine **4** with 2 equiv of methyl 6-(bromomethyl)picolinate afforded the protected ligand **5** in modest yields. DIPEA was a superior base vs K_2CO_3 in this reaction. Attempts to isolate compound **5** while using K_2CO_3 as a base were hampered by difficulties in purification, presumably due to the product chelating free K^+ ions from solution. This difficulty was entirely mitigated by using an organic base to generate a pure product in good yield. Final deprotection of compound **5** was achieved through ester hydrolysis in 4 M HCl, followed by reverse-phase high-performance liquid chromatography (HPLC). Coevaporation of the purified ligand with 3 M HCl afforded $\text{H}_4\text{noneunpaX}$ **6** as

its HCl salt. The purified ligand and all synthetic intermediates were fully characterized by NMR spectroscopy (^1H , $^{13}\text{C}\{^1\text{H}\}$, COSY, HSQC) and mass spectrometry (LR/HR-MS). Elemental analysis and HPLC analysis of the final ligand were performed to confirm the purity of the isolated product; characterization data for all isolated compounds are provided in the Supporting Information.

Metal Complexation and Characterization. The coordination characteristics of $\text{H}_4\text{noneunpaX}$ were investigated through complexation of a series of nonradioactive trivalent metal ions (La^{3+} , Lu^{3+} , and In^{3+}) and assessment of the spectral changes as a function of metal ionic radius using NMR spectroscopy (^1H , COSY). Metal complexes of $\text{H}_4\text{noneunpaX}$ were prepared by mixing equimolar amounts of the ligand with the appropriate metal salts in D_2O and adjustment of the pD to neutral using NaOD (0.1 M). The corresponding solutions were then filtered and analyzed directly via ^1H NMR spectroscopy, Figure 1. Further confirmation of metal complexation was achieved using high-resolution electrospray ionization mass spectrometry (HR-ESI-MS), wherein each metal complex was confirmed by the presence of a monocationic peak corresponding to the $[\text{M} + 2\text{H}]^+$ species, Table 1. The complexation of $\text{H}_4\text{noneunpa}$ with trivalent metal ions (La^{3+} , Lu^{3+} , and In^{3+}) has been thoroughly evaluated in previous studies.^{19,27} Full ^1H NMR characterization data (^1H , COSY) are provided in Figures S71–S82. Attempts to characterize the $[\text{Sc}(\text{noneunpaX})]^-$ complex by NMR were hampered by poor solubility in aqueous solution; spectra suitable for structural interpretation were not obtained.

Table 1. HR-ESI-MS Characterization of Metal Complexes of H₄noneunpaX with La³⁺, Lu³⁺, and In³⁺

metal complex	theoretical mass [M + 2H] ⁺	experimental mass [M + 2H] ⁺
[La(noneunpaX)] [−]	627.0536	627.0600
[Lu(noneunpaX)] [−]	663.0873	663.0946
[In(noneunpaX)] [−]	603.0506	603.0572

The ¹H NMR spectrum of [La(noneunpaX)][−] shows the formation of a single, symmetric isomer in solution, with characteristic diastereotopic splitting for the methylenic protons associated with the four pendent donor arms of the ligand, confirming coordination of all four donor groups to the metal center. Sharply resolved resonances are observed for the protons within the ethylene bridged backbone, which suggests the formation of a metal complex with the central ethereal oxygen coordinated. In contrast, the ¹H NMR spectra for the Lu³⁺ complex reveal a single, asymmetric isomer, wherein chemically distinct resonances for each picolinic acid donor arm are seen in the aromatic region. Notably, one picolinate donor arm (H_b, H_m, H_n) maintains the same chemical shift as seen in the La³⁺ complex, while the second picolinate arm (H_b, H_p, H_i) exhibits a significant downfield shift, which may imply closer coordination to the Lu³⁺ metal center and a change in ligand conformation at this position. This aspect is further observed for the adjacent methylenic hydrogens (H_g and H_{g'}), which exhibit distinctive diastereotopic splitting, with characteristically large coupling constants (²J_{AB} = 15.8 Hz), and appear in two distinct chemical environments (Δδ_{g/g'} = 0.78 ppm). The remaining methylenic hydrogens associated with the pendent donor arms all become inequivalent on metal ion complexation, appearing as diastereotopic doublets, which are clearly distinguished in the ¹H–¹H COSY NMR spectra, Figures S76–S79. In contrast to [La(noneunpaX)][−], the Lu³⁺ complex shows further splitting for all eight protons in the backbone, with large differences in chemical shift for mutually coupled protons (e.g., H_c and H_{c'}), suggesting a rigid complexation environment with close coordination to the metal center.

The data for metal complexes of H₄noneunpaX share similar spectral characteristics to data reported for H₄noneunpa, wherein fully saturated metal coordination spheres were achieved with La³⁺ and Lu³⁺ ions, as indicated by diastereotopic splitting of the pendent donor arm resonances and backbone ethylene bridges. Interestingly, the opposite trend in metal complex symmetry was attained for H₄noneunpa, wherein the [La(noneunpa)][−] complex appears as an asymmetric isomer, while the [Lu(noneunpa)][−] complex was symmetric.¹⁹ Analysis of the [In(noneunpaX)][−] complex by NMR was hampered by low solubility at neutral and basic pH; therefore, the ¹H NMR spectrum in Figure 1 was recorded under acidic conditions (pH ~ 4.0). The spectrum obtained shows the formation of a different symmetric isomer in which both picolinate donors are coordinated to the metal center, while the two acetate donor arms remain unbound, as indicated by the presence of a 4H singlet resonance at 3.50 ppm corresponding to H_{a/a'} and H_{b/b'}. This assignment is also supported by the resonances observed for the backbone methylene hydrogens, which appear as broad signals in the NMR spectrum. At higher pH values (pH ~ 5.0–8.5), a second species was observed, which may correspond to the fully coordinated complex—complete spectral analysis was not possible.

Solution Thermodynamic Stability Studies. Prior to investigation of the thermodynamic stability of different metal complexes, the protonation constants of the unbound ligand must be determined independently due to the competition between a given metal ion and a proton for the same coordinating atom in the metal complexation reaction. Combined potentiometric and UV–vis spectrophotometric titrations were used to evaluate the protonation constants of H₄noneunpaX between pH ~ 2 and 11.5, while acidic in-batch UV–vis spectrophotometric titrations were used to determine the protonation constants for the most acidic protons, which were below the threshold of the pH electrode (pH < 2). All eight protonation constants for H₄noneunpaX were determined through refinement of the experimental data using HyperSpec2014³⁵ and Hyperquad2013,³⁶ Table 2.

Table 2. Protonation Constants (Log K_{HqL})^a of H₄noneunpaX and H₄noneunpa (Oxyaapa)²⁷ at 25 °C and I = 0.16 M NaCl

reaction	H ₄ noneunpaX log K	H ₄ noneunpa (Oxyaapa) ²⁷ log K
L + H ⁺ ⇌ HL	8.84	8.47 (4)
HL + H ⁺ ⇌ H ₂ L	7.08	7.63 (2)
H ₂ L + H ⁺ ⇌ H ₃ L	3.79	3.66 (4)
H ₃ L + H ⁺ ⇌ H ₄ L	2.83	2.90 (1)
H ₄ L + H ⁺ ⇌ H ₅ L	2.38	1.77 (12)
H ₅ L + H ⁺ ⇌ H ₆ L	2.14	n.d.
H ₆ L + H ⁺ ⇌ H ₇ L	1.01	n.d.
H ₇ L + H ⁺ ⇌ H ₈ L	−0.72 ^b	n.d.
Σlog K _{HqL}	27.35 (6)	

^aK_{HqL} defined as [H_qL]/([H][H_{q−1}L]). ^bNot evaluated at constant I = 0.16 M NaCl. Charges omitted for simplicity. Values in brackets are the standard deviations. n.d. not determined.

The protonation constants obtained for H₄noneunpaX follow the trend observed for similar polyaminocarboxylate-based ligands;^{17,26,27} wherein the first two dissociation events (species H₈L⁴⁺ and H₇L³⁺) can be attributed to the protonated pyridyl nitrogen donors. Deprotonation of each successive pyridine donor, with pK_a −0.72 and 1.01, respectively, is concurrent with spectral changes in the absorbance spectrum of the ligand, where a large decrease in the absorptivity of the ligand is observed for the first dissociation event, Figures S83–S86. Sequential deprotonation of the two acetate carboxylic groups (log K₆ = 2.14 and log K₅ = 2.38) is followed by the two picolinate donors (log K₄ = 2.83 and log K₃ = 3.79), while the final two deprotonations are assigned to dipyridyl (log K₂ = 7.08) and iminodiacetate (log K₁ = 8.84) terminal amines, respectively. The protonation constant measured for species HL is comparable to other ligands containing the iminodiacetate moiety [e.g., N-(2-hydroxyethyl)iminodiacetic acid (HEIDA), log K₁ = 8.68].³⁷ In contrast, the second terminal amine in H₄noneunpaX is less basic (log K₂ = 7.08) than the equivalent donor group in H₄noneunpa/Oxyaapa (log K₂ = 7.63),²⁷ which can be attributed to the stronger electron-withdrawing effect induced by placing two picolinate donors on the same nitrogen atom, in addition to the steric constraints at this position, which may disfavor protonation. The larger difference in basicity between the terminal amines of H₄noneunpaX, in comparison to H₄noneunpa/Oxyaapa, may be advantageous for metal ion coordination, whereby the less

Table 3. Stability Constants ($\log K_{ML}$, $\log K_{MHL}$, and $\log K_{M(OH)L}$)^b of H₄noneunpaX with M³⁺ = Sc³⁺, In³⁺, Lu³⁺, Dy³⁺, Gd³⁺, Sm³⁺, La³⁺ Metal Ions at 25 °C and I = 0.16 M NaCl^a

	Sc ³⁺	In ³⁺	Lu ³⁺	Dy ³⁺	Gd ³⁺	Sm ³⁺	La ³⁺
H ₄ noneunpaX							
$\log K_{ML}$	23.57(2)	27.64(2)	21.93(3)	21.99(5)	20.87(4)	21.04(2)	18.45(4)
$\log K_{MHL}$	3.07(1)	6.17(3)	2.28(3)	2.29(2)	2.80(1)	2.77(1)	3.22(2)
$\log K_{M(OH)L}$	10.89(2)	8.58(4)					
$\log K_{M(OH)2L}$		9.06(4)					
pM ^c	22.9	26.5	21.3	21.3	20.2	20.4	17.8
H ₄ noneunpa (Oxyaapa) ²⁷							
$\log K_{ML}$			21.49(4)		20.50(5)		19.06(5)
pM ^c			21.1		19.9		18.5

^aStability contrasts of H₄noneunpa (Oxyaapa) with M³⁺ = Lu³⁺, Gd³⁺, La³⁺ reported by Hu et al.²⁷ ^b K_{ML} defined as $[ML]/([M][L])$; K_{MHL} defined as $[MHL]/([ML][H])$; $K_{M(OH)L}$ defined as $[M(OH)L]/([ML][OH])$ (charges omitted for clarity). ^cpM defined as $-\log[M_{free}]$ when $[L] = 10 \mu M$; $[M] = 1 \mu M$ at pH 7.4.

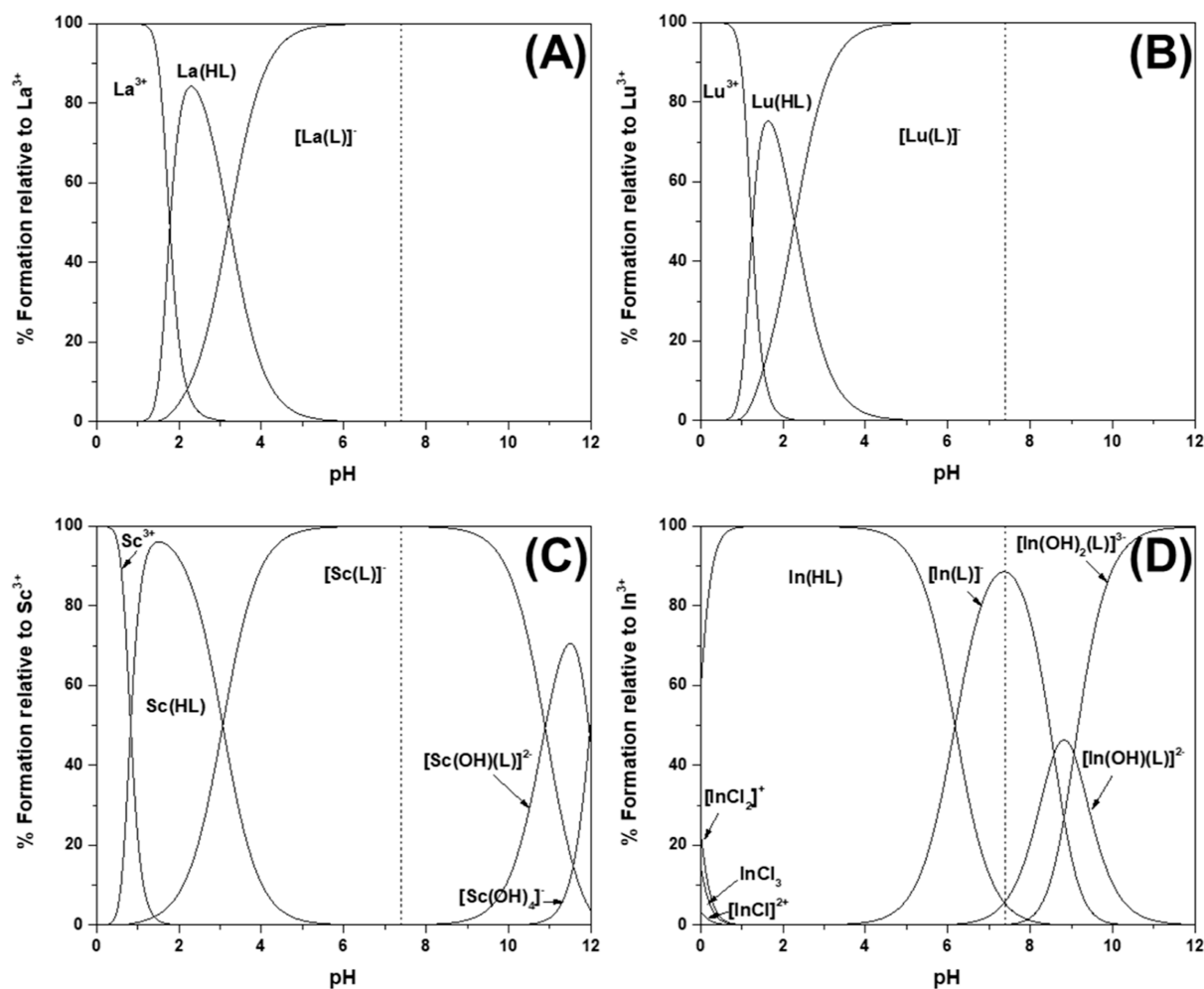


Figure 2. Speciation diagrams for the metal complexes of H₄noneunpaX [(A): La³⁺, (B): Lu³⁺, (C): Sc³⁺, (D): In³⁺], $[M^{3+}] = [H_4noneunpaX] = 1 \times 10^{-3}$ M. Dashed lines indicate physiological conditions (pH 7.4).

basic dipyrldyl nitrogen favors complexation at a lower pH, while the more basic iminodiacetate nitrogen will act as a stronger donor group to metal ions.

Complexation Equilibria with Sc³⁺, In³⁺, Lu³⁺, Dy³⁺, Gd³⁺, Sm³⁺, La³⁺. To evaluate the affinity of H₄noneunpaX for metal ions of medicinal importance—Sc³⁺, In³⁺, Lu³⁺, Dy³⁺, Gd³⁺, Sm³⁺, La³⁺—the complex formation equilibria were studied using both combined potentiometric-spectrophotometric titrations and acidic in-batch UV–vis spectrophotometric

titrations below pH 2. H₄noneunpaX showed a high affinity to all metal ions investigated, with metal complexation observed to begin < pH 1. Full characterization for all complexes is provided in Figures S87–107.

H₄noneunpaX shows a strong thermodynamic preference for complexation with trivalent Ln³⁺ ions, as indicated by the high stability constants ($\log K_{ML}$) and pM values, Table 3. Notably, these values are directly comparable to those previously determined for H₄noneunpa/Oxyaapa,²⁷ with H₄noneunpaX

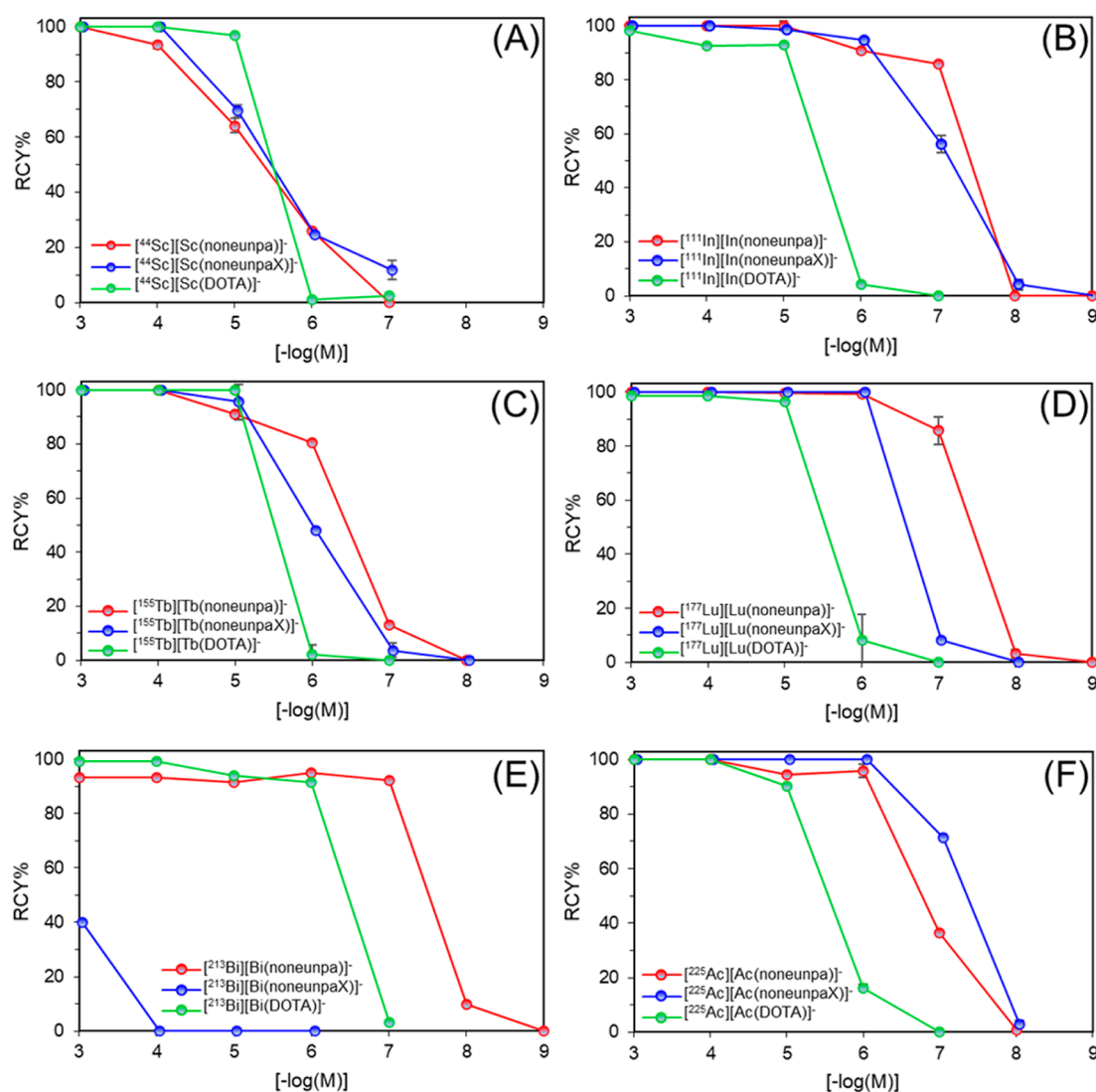


Figure 3. Concentration-dependent radiolabeling studies of $H_4noneunpa$, $H_4noneunpaX$, and DOTA with (A) $[^{44}Sc]Sc^{3+}$ (1.2 MBq) in NaOAc (0.1 M, pH 4.5), (B) $[^{111}In]In^{3+}$ (1.0 MBq) in NH_4OAc (0.5 M, pH 5.8), (C) $[^{155}Tb]Tb^{3+}$ (40 kBq) in NH_4OAc (0.5 M, pH 6.0), (D) $[^{177}Lu]Lu^{3+}$ (150 kBq) in NH_4OAc (0.5 M, pH 6.0), (E) $[^{213}Bi]Bi^{3+}$ (680 kBq) in MES (1.0 M, pH 5.5), (F) $[^{225}Ac]Ac^{3+}$ (40 kBq) in NH_4OAc (1.0 M, pH 7.3). All reactions with $H_4noneunpa$ and $H_4noneunpaX$ were carried out at ambient temperature and monitored after 10 min, with the exception $[^{213}Bi]Bi^{3+}$, which were monitored after 5 min, within 10 min postgenerator elution ($n = 4-8$). Reactions with DOTA were carried out at 85–90 °C and monitored over 30–60 min.

exhibiting marginally higher stability constants with Lu^{3+} and Gd^{3+} , implying a small thermodynamic benefit to this inverted *syn* structural arrangement of pendent donor arms (which may be a result of a degree of preorganization of the binding cavity of the ligand). Furthermore, the pM values obtained for $H_4noneunpaX$ with Ln^{3+} ions exceed those of the current gold-standard chelators DOTA and DTPA by several log units (e.g., pLu = 17.1 and 19.1, respectively).²² While stability constants and pM values are useful parameters for quantitatively comparing the metal scavenging of different chelating ligands, they do not necessarily correlate well with in vivo stability. Another important aspect for consideration is the speciation behavior of a given metal complex as a function of pH. Speciation plots for complexation of $H_4noneunpaX$ with trivalent lanthanide ions show an interesting relationship, with the formation of the protonated MHL species at acidic pH followed by a single transformation to the dominant binary $[ML]^-$ species across a broad pH range and the absence of any

ternary hydroxo complex even under very basic conditions (pH = 11.5), Figure 2. This is contrary to many similar chelating ligands with Ln^{3+} ions previously reported— $H_4octapa$, H_4pypa , H_4octox —which all show one or more hydroxo species (e.g., $[M(OH)L]$, $[M(OH)_2L]$) under basic conditions (pH > 9.0), typically attributed to deprotonation of a metal-ion-coordinated water molecule in the complex.^{18,20,26} Under physiological conditions (pH 7.4), a single species ($[ML]^-$) is observed for all Ln^{3+} complexes of $H_4noneunpaX$, which is highly favorable for in vivo applications since multiple different charged species (i.e., $[M(HL)]$ and $[ML]^-$) at pH 7.4 can exhibit different pharmacokinetic and biodistribution profiles.

Combined potentiometric-spectrophotometric titrations of $H_4noneunpaX$ with smaller trivalent metal ions show a different relationship within the Ln^{3+} series. Higher stability constants were determined for Sc^{3+} and In^{3+} , compared to Ln^{3+} , as is typically observed owing to the higher charge density of these metal centers, Table 3. With Sc^{3+} , complex formation occurs

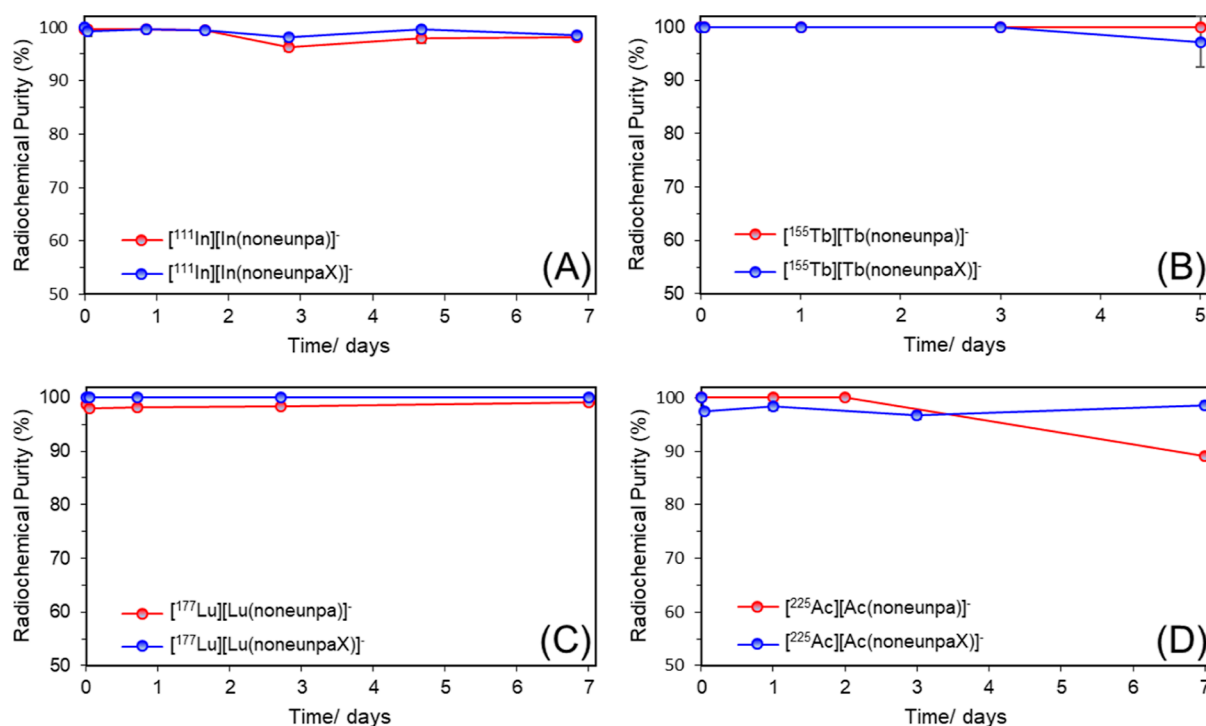


Figure 4. Human serum stability studies of $\text{H}_4\text{noneunpa}$ and $\text{H}_4\text{noneunpaX}$ with (A) $^{111}\text{In}^{3+}$ (54 GBq/ μmol), (B) $^{155}\text{Tb}^{3+}$ (1.0 GBq/ μmol), (C) $^{177}\text{Lu}^{3+}$ (2.0 GBq/ μmol), (D) $^{225}\text{Ac}^{3+}$ (134 MBq/ μmol). All experiments were performed at 37 °C and monitored via radio-TLC ($n = 3$).

below $\text{pH} \approx 0.5$ to give the neutral MHL species, which is deprotonated with increasing pH to give $[\text{ML}]^-$. This transformation occurs in a similar range to the Ln^{3+} complexes of $\text{H}_4\text{noneunpaX}$ ($\text{pK}_a = 2.28\text{--}3.22$) and may be attributed to the deprotonation of one of the carboxylate donors. In contrast, the In^{3+} complex shows different thermodynamic behavior in solution. The MHL species deprotonates with a higher pK_a to form the anionic $[\text{ML}]^-$ species [$\text{pK}_a = 6.17(3)$], which is assigned to the tertiary amine of the iminodiacetate moiety that remains protonated early in the complexation. This is consistent with the NMR characterization of $[\text{In}(\text{noneunpaX})]^-$ —a single species at pH 4.0 in which the two acetate donor groups remain unbound to the metal center. As with Sc^{3+} , the formation of a ternary $[\text{In}(\text{OH})\text{L}]^{2-}$ species is observed at higher pH, explained by the mismatch between the size of these small metal ions and the larger ligand binding cavity.

Radiolabeling Studies. Radiolabeling studies with ^{44}Sc - Sc^{3+} , ^{111}In - In^{3+} , ^{177}Lu - Lu^{3+} , ^{155}Tb - Tb^{3+} , ^{213}Bi - Bi^{3+} , and ^{225}Ac - Ac^{3+} ions have been performed to investigate the variation in metal ion affinity with changes in ionic radii across a broad size range and coordination number. ^{225}Ac ($t_{1/2} = 9.92$ days) is an interesting candidate for TAT owing its long half-life and the potency of particulate radiation emitted within its four-alpha decay scheme. Suitable ^{225}Ac companion radionuclides with comparable coordination characteristics and imageable decay properties to perform accurate staging of disease progression and assessment of patient suitability for treatments include ^{111}In ($t_{1/2} = 2.83$ days)³⁸ and ^{155}Tb ($t_{1/2} = 5.32$ days),³¹ both suitable for SPECT imaging owing to the emission of high abundance and low energy γ -rays (171 and 245 keV [^{111}In];³⁸ 44, 87, and 105 keV [^{155}Tb]³¹) in their decay schemes. Both are well-matched to the half-life of ^{225}Ac . ^{44}Sc is a promising candidate for PET imaging owing to its physical half-life ($t_{1/2} =$

3.97 h) and high positron branching ratio ($E_{\beta^+} = 632$ keV, 94.3%); the companion radioisotope ^{47}Sc ($t_{1/2} = 3.35$ days) may find utility for β^- -therapy ($E_{\beta^-} = 162$ keV, 100%).³⁹

Concentration-dependent radiolabeling studies showed $\text{H}_4\text{noneunpaX}$ to be a highly versatile chelator, exhibiting high affinity for all metal ions tested, with the exception of $^{213}\text{Bi}^{3+}$, Figure 3. Significantly, quantitative radiochemical yields (RCYs) were achieved within 10 min at ambient temperature, a notable advantage over DOTA. Optimal RCYs were obtained under mild conditions (pH 7.0, ambient temperature, 10 min), compatible with thermally sensitive biological targeting vectors such as monoclonal antibodies. $\text{H}_4\text{noneunpaX}$ showed comparable coordination characteristics to $\text{H}_4\text{noneunpa}$; each chelate was successfully radiolabeled at high molar activities with $^{111}\text{In}^{3+}$ (54 GBq/ μmol), $^{155}\text{Tb}^{3+}$ (1.0 GBq/ μmol), $^{177}\text{Lu}^{3+}$ (2.0 GBq/ μmol), and $^{225}\text{Ac}^{3+}$ (134 MBq/ μmol).

Concentration-dependent radiolabeling studies of $\text{H}_4\text{noneunpa}$ and $\text{H}_4\text{noneunpaX}$ with ^{44}Sc - Sc^{3+} showed poor radiometal ion compatibility, whereby low RCYs were achieved at low ligand concentrations. These results were anticipated based on the small ionic radius (0.870 Å, CN = 8) and chemical hardness of the Sc^{3+} ion, which prefers coordination numbers 6–8.²⁹ These results further suggest no significant difference in metal ion affinity between the conventional “anti”-constitutional arrangement and the inverted “syn”-regioisomer for ligands based on this framework.

The distinct contrast in radiolabeling efficiency exhibited by each chelate for $^{213}\text{Bi}^{3+}$ was somewhat surprising given the similarities in donor atoms and the observed trends with other trivalent metal ions. This deviation can be rationalized by consideration of the coordination characteristics of the Bi^{3+} ion. Bi^{3+} [1.150 Å (CN = 9)] has a similar ionic radius to Ac^{3+} (1.220 Å (CN = 9)),^{29,30} but it is of intermediate chemical

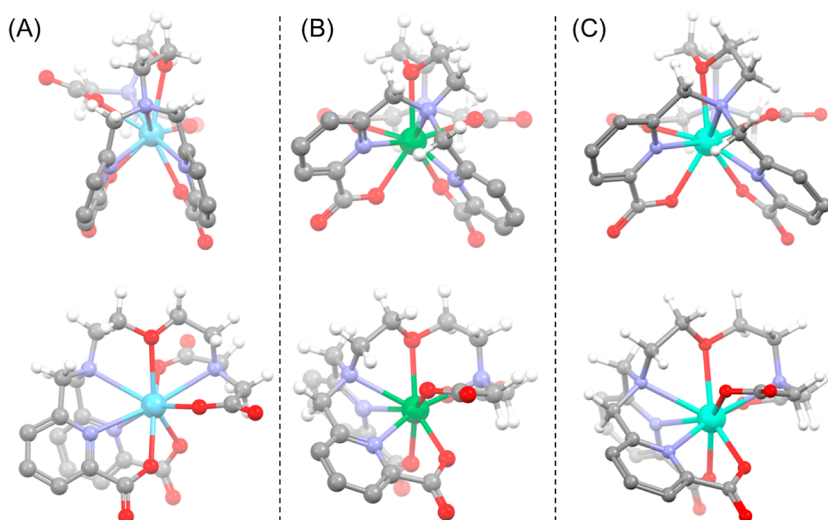


Figure 5. DFT-optimized structures of (A) $[\text{La}(\text{noneunpaX})]^-$, (B) $[\text{Lu}(\text{noneunpaX})]^-$, and (C) $[\text{Y}(\text{noneunpaX})]^-$. Selected hydrogens have been omitted for clarity.

hardness, exhibiting a stronger preference for intermediate hardness donor groups (e.g., nitrogen, pyridine) over hard ionic donors (oxygen, phenolates). Bi^{3+} may exhibit a stereochemically active $6s^2$ lone pair to induce significant impacts on the favored conformational geometries of the chelating ligand and its effective denticity.^{10,40}

In the case of $\text{H}_4\text{noneunpa}$ and $\text{H}_4\text{noneunpaX}$, the contrast in $[\text{Bi}^{3+}]$ chelation may be attributed to the large difference in steric accessibility of the nitrogen donor atoms in the backbone of each ligand. The steric crowding around N(1) imparted by the two picolinic acid donors in $\text{H}_4\text{noneunpaX}$ reduces the ability of the nitrogen atom to act as an effective donor to the large Bi^{3+} ion, leading to a longer overall bond length and weaker binding to the metal center. This characteristic has been further explored using DFT calculations of the metal complexes of both chelating ligands, *vide infra*.

Human Serum Stability Studies. A series of serum stability challenge assays were undertaken in order to determine the kinetic inertness of $\text{H}_4\text{noneunpaX}$ and $\text{H}_4\text{noneunpa}$ complexes with $[\text{In}^{3+}]$, $[\text{Tb}^{3+}]$, $[\text{Lu}^{3+}]$, and $[\text{Ac}^{3+}]$ in the presence of competing endogenous metal binding proteins. For $\text{H}_4\text{noneunpaX}$, incubation of the radiolabeled complexes at 37 °C in human serum showed no release of bound radiometal over 5–7 days, indicating high kinetic inertness and potential for *in vivo* application, Figure 4. The radiolabeled complexes of $\text{H}_4\text{noneunpa}$ exhibited similar kinetic inertness to $\text{H}_4\text{noneunpaX}$, maintaining >97% radiochemical purity over 5–7 days, with the exception of $[\text{Ac}^{3+}][\text{Ac}(\text{noneunpa})]^-$, which showed an initial drop in radiochemical integrity of ~10% over the course of the study.

Computational Studies. To explore the solution structures of the metal complexes of $\text{H}_4\text{noneunpaX}$, DFT calculations were carried out using Gaussian 16 (revision B.01) in the polarizability continuum model (PCM).^{41,42} Geometrical optimizations were performed with the hybrid Perdew–Burke–Ernzerhof (PBE(0)) exchange–correlation functional, using the relatively small core quasi-relativistic effective core potentials (ECP28/60MWB) and associated valence basis-sets for metal ions (La^{3+} , Lu^{3+} , Bi^{3+} , Y^{3+}), while light atoms (C, H, N, O) were modeled up to Def2TZVP levels of theory.^{43–45} Optimized structures for all complexes, with

Cartesian coordinates and calculated thermodynamic energy values, are provided in Figures S108–S112.

The distribution of donor arm substituents within the framework of $\text{H}_4\text{noneunpaX}$ generates two distinct conformational arrangements upon metal ion coordination (with a coordination number of 9), which differ by the relative orientation of the two mutual picolinate donors that adopt either a parallel or antiparallel relationship. These conformational isomers arise from the relative orientation of the 5-membered chelate rings formed between the ligand backbone and the metal center (λ vs δ). The solution structures for the regioisomer, $\text{H}_4\text{noneunpa}/\text{Oxyaapa}$, with La^{3+} , Lu^{3+} , and In^{3+} have been thoroughly investigated in previous studies.^{19,27} Geometric optimizations of $\text{H}_4\text{noneunpaX}$ with La^{3+} , Lu^{3+} , and Y^{3+} were undertaken to give an overview of the solution phase structures across the lanthanide series. In this case, Y^{3+} was used as a surrogate for modeling of Ln^{3+} ions with partially filled 4f-orbitals (i.e., Tb^{3+}) due to the high computational expense of performing DFT calculations with high spin angular momenta metal ions (e.g., Tb^{3+} , $S = 6$). This approach has been applied in previous studies and is a reasonable compromise given the similar ionic radii, electronegativity, and same valence of Y^{3+} and Tb^{3+} .^{46,47} The optimized structures for $[\text{M}(\text{noneunpaX})]^-$ show fully saturated metal coordination spheres, whereby all nine donor atoms from the ligand were bound to the metal centers. In the case of $[\text{La}(\text{noneunpaX})]^-$, the symmetric $\delta\delta$ configuration was favored being the lowest in energy by 5.30 kJ mol⁻¹, while the $[\text{Lu}(\text{noneunpaX})]^-$ complex favored a different asymmetric isomer with a twisted $\lambda\delta$ conformation (lowest in energy by 12.9 kJ mol⁻¹), Figure 5. Intriguingly, this is in contrast to the complexation reported for $\text{H}_4\text{noneunpa}$, which was found to form an asymmetric complex with La^{3+} and a symmetric complex with Lu^{3+} . The $[\text{Y}(\text{noneunpaX})]^-$ complex closely resembled the coordination geometry of the Lu^{3+} complex, attaining the same conformational isomer with each picolinate donor in a twisted, antiparallel relationship, Figure 5C.

The structure of $[\text{La}(\text{noneunpaX})]^-$ shows a high degree of symmetry, wherein the two picolinic acid donors adopt the same relative arrangement, with both pyridine rings eclipsed/parallel, while the two acetate donors also adopt the same

relative arrangement in an antiparallel orientation relative to the central plane of symmetry. This characterization is fully consistent with the experimental NMR results of the La^{3+} complex, which delineated a single, symmetric isomer in solution. Additionally, from the DFT calculated structure, the methylene protons adjacent to the acetate groups (H_a/H_b and H_a'/H_b') are shown in nearly identical chemical environments, thus giving rise to two pairs of diastereotopic doublets in the ^1H NMR spectrum with similar chemical shifts ($\delta_{ab} = 3.37$ ppm, $\delta_{a'b'} = 3.31$ ppm). By contrast, the solution phase structure of $[\text{Lu}(\text{noneunpaX})]^-$ shows a single asymmetric isomer, wherein a change in backbone geometry to the $\lambda\delta$ conformation causes a shift in the relative arrangement of the picolinic acid donors to an orthogonal configuration. This conformational shift is further supported by the ^1H NMR characterization of the Lu^{3+} complex, which exhibits sharply resolved, diastereotopic doublets for the four methylenic protons neighboring the picolinate donor arms. The large differences in chemical shift for mutually coupled protons H_g/H_g' ($\Delta\delta = 0.78$ ppm) and H_k/H_k' ($\Delta\delta = 0.74$ ppm) can be easily accounted for by the distinct local environments adopted in the rigid $[\text{Lu}(\text{noneunpaX})]^-$ complex, Figure 5B.

The solution phase characteristics of $[\text{Bi}(\text{noneunpaX})]^-$ and $[\text{Bi}(\text{noneunpaX})]^-$ were also investigated using DFT to provide insights into the structural origins of the drastic difference in complexation properties observed in radiolabeling studies with $^{213}\text{BiBi}^{3+}$. Clear differences in the interatomic bond distances between the backbone donor atoms and central Bi^{3+} ion are apparent in the structures of the two metal complexes, Figure 6. Specifically, the Bi–N(1) and Bi–O(5)

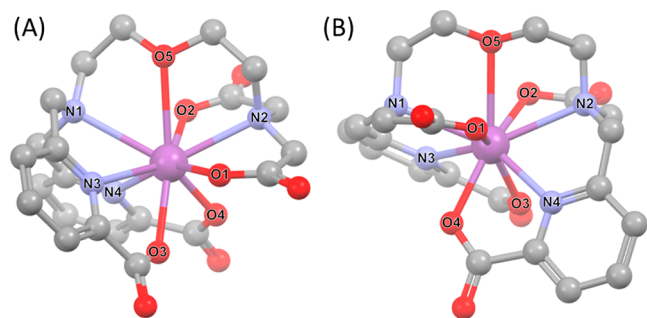


Figure 6. DFT-optimized structures of (A) $[\text{Bi}(\text{noneunpaX})]^-$ and (B) $[\text{Bi}(\text{noneunpaX})]^-$. Hydrogens have been omitted for clarity.

bond distances in $[\text{Bi}(\text{noneunpaX})]^-$ are elongated at 2.794 and 2.768 Å, respectively, compared to $[\text{Bi}(\text{noneunpaX})]^-$, wherein the equivalent donor distances are 2.661 and 2.698 Å. This deviation in bonding is a result of the increased steric constraints induced by anchoring two large picolinic acid donors to the same terminal nitrogen atom N(1), consequently disfavoring coordination of the large Bi^{3+} ion (ionic radius = 1.15 Å, CN = 9),⁴⁸ in addition to the hard anionic nature of the two acetate units placed on N(2), which are more poorly matched to the intermediate-hardness of the Bi^{3+} ion. In contrast, the combination of one acetate and one picolinic acid pendent donor group on the same nitrogen atom, as in the case of $[\text{Bi}(\text{noneunpa})]^-$, gives an overall hardness, which is well-matched to that of Bi^{3+} and reduces the steric constraints for effective backbone coordination. This observation was also observed for $[\text{Bi}(\text{neunpa-NH}_3)]$, which features the same configuration of donor arms on a more nitrogen-rich backbone

and has demonstrated highly favorable complexation with $^{213}\text{BiBi}^{3+}$ as well as good stability in vivo.

The structural differences between the $[\text{Bi}(\text{noneunpaX})]^-$ and $[\text{La}(\text{noneunpaX})]^-$ complexes (and moreover, the contrasting radiolabeling characteristics of the corresponding $^{213}\text{BiBi}^{3+}$ and $^{225}\text{AcAc}^{3+}$ complexes) are of significance between these trivalent metal ions of comparable ionic radii (1.150, 1.216, 1.220 Å, for Bi^{3+} , La^{3+} , and Ac^{3+} , respectively, CN = 9).^{29,30,48} We hypothesize that the differences observed with $\text{H}_4\text{noneunpaX}$ may be attributed to steric activation of the $6s^2$ lone pair on Bi^{3+} by the “syn” coordinating ligand. Natural bond orbital (NBO) analysis was performed on $[\text{Bi}(\text{noneunpaX})]^-$ to assess the extent of steric activation and implications on bonding.⁴⁹ From NBO analysis of the molecular orbital (MO) containing the $6s^2$ lone pair on Bi^{3+} , a percentage 6p-character of 1.90% was determined for $[\text{Bi}(\text{noneunpaX})]^-$, indicating significant stereochemical activation of the $6s^2$ lone pair. Although the extent of 6p mixing with the $6s^2$ lone pair is relatively small, this degree of 6p contribution has been shown previously to be sufficient to cause anisotropic distortions to the 6s-shell and thus the metal-complex geometry.^{10,40} By constant, NBO calculations for $[\text{Bi}(\text{noneunpa})]^-$ determined a 0.55% p-character for the $6s^2$ lone pair, implying a more symmetric distribution of electron density surrounding the Bi^{3+} ion.

Contour-plots of the electron-density for the MO comprising the $6s^2$ lone pair in both metal complexes are shown in Figure 7, wherein an asymmetric distribution for $[\text{Bi}(\text{noneunpaX})]^-$ in the direction of the N(1) and O(5) donor atoms is clearly visible, which further disfavors coordination to the metal center. Collectively, the combination of a sterically active lone pair with the high steric hindrance present at N(1) ultimately disfavors the Bi^{3+} ion in this case.

Bifunctional $\text{H}_4\text{noneunpaX}$. In pursuit of novel bifunctional chelating ligands, a critical factor for potential clinical translation is the synthetic accessibility of a given compound; chelators featuring superior complexation characteristics may not be feasible for industrial application if their fundamental design requires detailed, time-consuming, inefficient, low-overall yielding multistep syntheses. With this consideration in mind, $\text{H}_4\text{noneunpaX}$ was selected for bifunctionalization over $\text{H}_4\text{noneunpa}$, given the synthetic ease and scalability of preparations involving such a diametrically opposed (“syn”) constitutional arrangement. Furthermore, this decision was driven by the objective to develop a viable chelation system for $^{225}\text{AcAc}^{3+}$ and its application in TAT; therefore, the lower overall stability in human serum observed for $^{225}\text{Ac}[\text{Ac}(\text{noneunpa})]^-$ favored $\text{H}_4\text{noneunpaX}$ as the more suitable candidate.

The synthetic approach for bifunctional $\text{H}_4\text{noneunpaX-Ph-NCS}$ (13) was straightforward in which an emphasis on single modifications and functional group interconversions was selected in each step in order to simplify purification of synthetic intermediates, minimize potential byproduct formation, and allow reaction scalability, Scheme 2.

The synthesis of bifunctional $\text{H}_4\text{noneunpaX-Ph-NCS}$ (13) proceeds through a pathway analogous to $\text{H}_4\text{noneunpaX}$, utilizing the same synthetic intermediates (compounds 1–4) to provide primary amine 4, which was protected using 2-nitrobenzenesulfonyl chloride to give the corresponding nosyl-protected sulfonamide 7 in high yield. N-alkylation of sulfonamide 7 with methyl (6-bromomethyl)picolinate under basic conditions was achieved through mild heating of the reaction mixture overnight, to generate the singularly alkylated

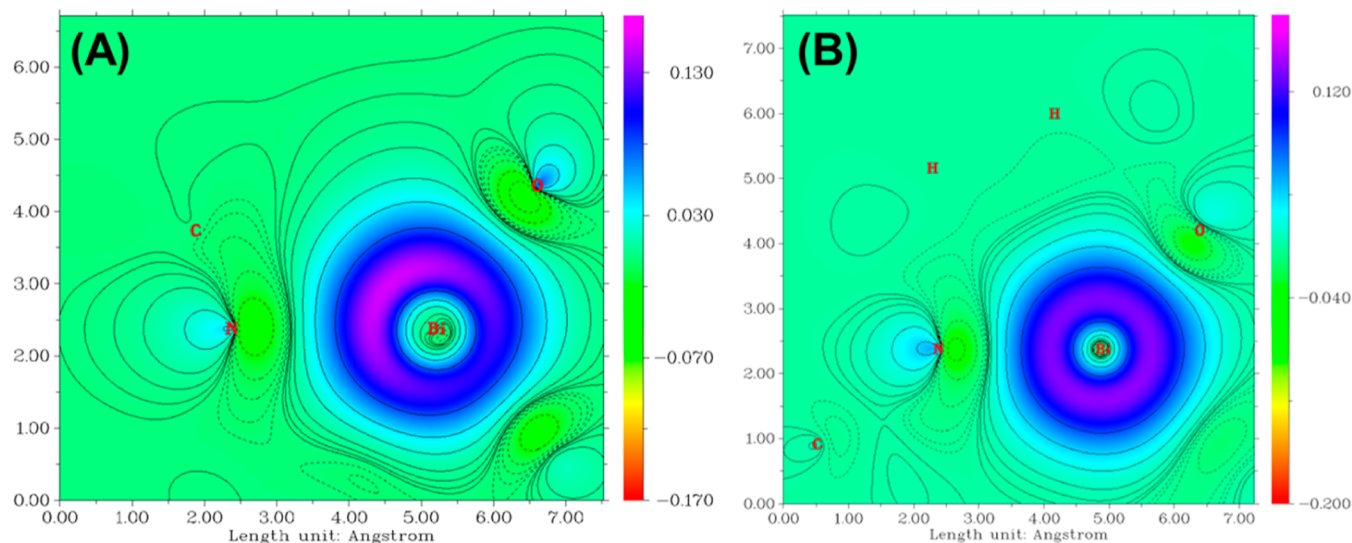
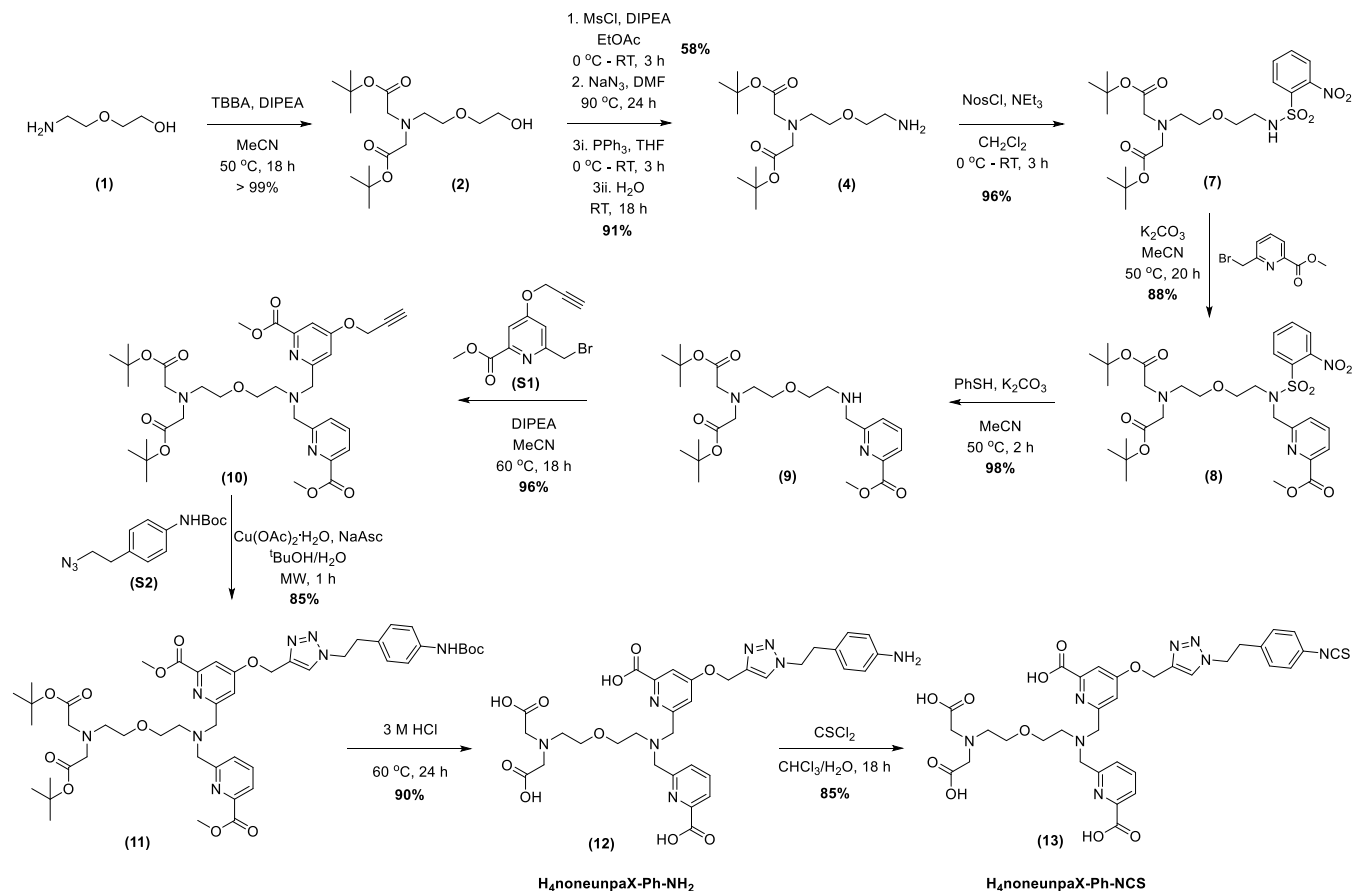


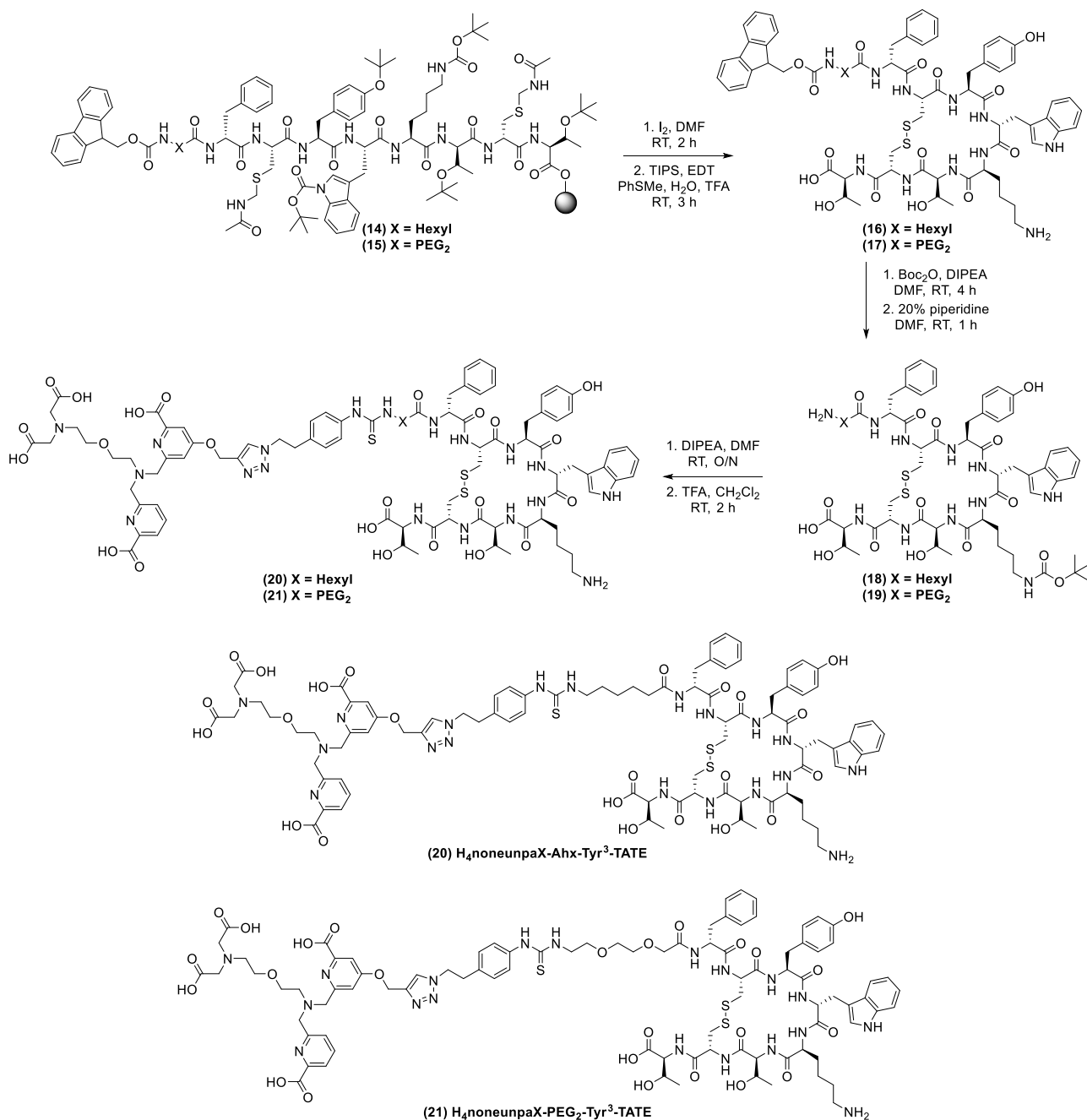
Figure 7. Contour plots of the electron wave function of the MO containing the $6s^2$ lone pair of Bi^{3+} in (A) $[\text{Bi}(\text{noneunpaX})]^-$ and (B) $[\text{Bi}(\text{noneunpa})]^-$.

Scheme 2. Synthesis of Bifunctional $\text{H}_4\text{noneunpaX-Ph-NCS}$ over 9 Steps with a Cumulative Yield of 28%



product cleanly in high yields. Removal of the nosyl-protecting group from compound **8** was achieved using thiophenol to give the corresponding secondary amine **9**. An excess of thiophenol (3 equiv) was necessary to achieve complete deprotection of compound **8** and avoid tedious purification of the desired product. Subsequent *N*-alkylation of secondary amine **9** using a functionalized derivative of the protected picolinic acid electrophile **S1** was achieved by mild heating overnight to

give the protected bifunctional ligand **10** with alkyne functionality, suitable for click-based bioconjugation. The alkyne-derivatized picolinate electrophile **S1** was prepared separately starting from chelidamic acid, the synthetic methodology for which is outlined in our previous studies^{50,51} and in the [Supporting Information](#). Alkyne **10** was subsequently reacted with the bifunctional azide linker **S2** using Huisgen's 1,3-dipolar cycloaddition to click using $\text{Cu}(\text{OAc})_2 \cdot \text{H}_2\text{O}$ for

Scheme 3. Syntheses of H₄noneunpaX-Ahx-Tyr³-TATE and H₄noneunpaX-PEG₂-Tyr³-TATE

generation of an in situ source of Cu(I) catalyst and sodium ascorbate as a reductant. Syntheses for the bifunctional azide linker **S2** are also outlined in the [Supporting Information](#). Compound **11** was treated with an excess of sodium sulfide to precipitate any traces of Cu(I/II) chelated by the protected ligand prior to removal of the methyl, *tert*-butyl, and Boc-protected groups using 3 M HCl. Purification of H₄noneunpaX-Ph-NH₂ **12** was achieved via RP-HPLC and the product isolated as the corresponding HCl salt by coevaporation with 3 M HCl. Conversion of the aniline **12** to the isothiocyanate **13** was carried out using standardized literature approaches involving thiophosgene⁵² and the product isolated via RP-HPLC.

Radiolabeling Studies of H₄noneunpaX-Ph-NH₂. To assess the potential impacts of bifunctionalization through one

picolinic acid donor arm on the radiometal chelating properties, concentration-dependent radiolabeling studies of H₄noneunpaX-Ph-NH₂ with [⁴⁴Sc]Sc³⁺, [¹¹¹In]In³⁺, [¹⁷⁷Lu]-Lu³⁺, [¹⁵⁵Tb]Tb³⁺, [^{133/135}La]La³⁺, and [²²⁵Ac]Ac³⁺ were undertaken and compared to the original unmodified chelate, [Figure S119](#). Radiolabeling of H₄noneunpaX-Ph-NH₂ with [⁴⁴Sc]Sc³⁺, [¹¹¹In]In³⁺, [¹⁷⁷Lu]Lu³⁺, [¹⁵⁵Tb]Tb³⁺, and [²²⁵Ac]-Ac³⁺ demonstrated results similar to those of the original chelating ligand, achieving quantitative RCYs within 10 min at ambient temperature, implying that no significant changes to the coordination environment were incurred through functionalization. Moderate improvements in RCYs with [⁴⁴Sc]Sc³⁺ and [¹⁵⁵Tb]Tb³⁺ were achieved compared to the nonbifunctional chelator at low ligand concentration (10⁻⁵ to 10⁻⁶ M), which may be attributed to the bifunctional appendage imposing a

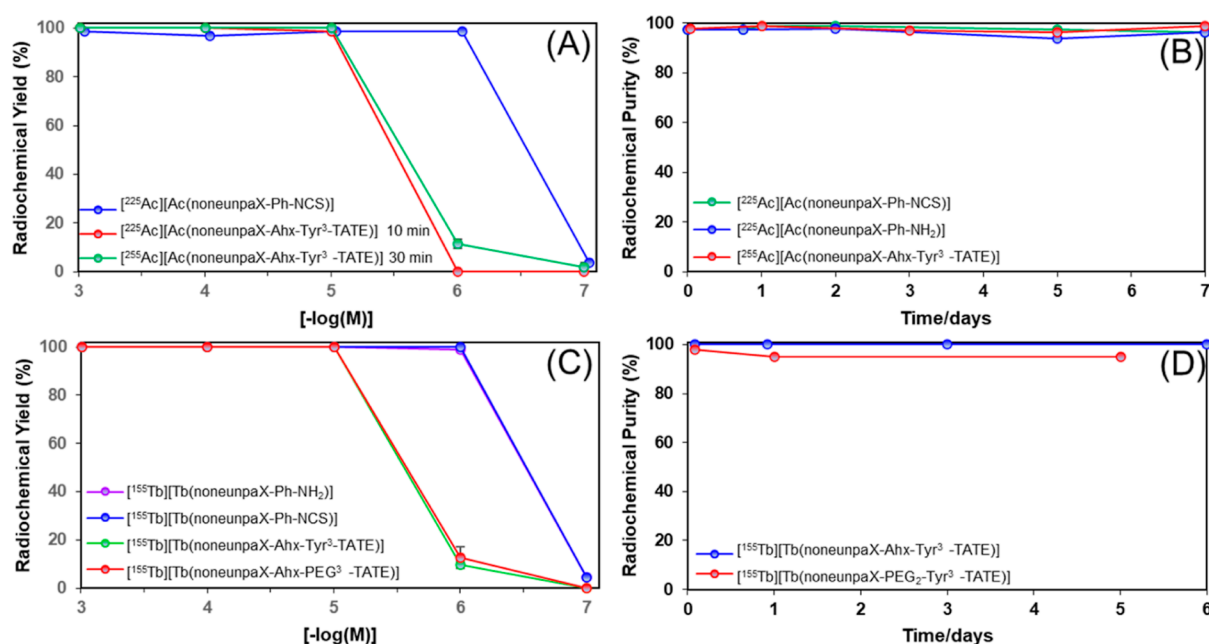


Figure 8. Radiolabeling studies of bifunctional H₄noneunpaX and corresponding peptide conjugates: (A) concentration-dependent radiolabeling with [²²⁵Ac]Ac³⁺ (40 kBq) in NH₄OAc buffer (0.5 M, pH 7) (RT, 10 min). (B) Human serum stability challenge of [²²⁵Ac]Ac³⁺-labeled compounds. (C) Concentration-dependent radiolabeling with [¹⁵⁵Tb]Tb³⁺ (120 kBq) in NH₄OAc buffer (0.5 M, pH 6) (RT, 10 min). (D) Human serum stability challenge of [¹⁵⁵Tb]Tb³⁺-labeled bioconjugates.

degree of preorganization in the binding cavity, thereby favoring metal complexation under these conditions.

Additional studies of H₄noneunpaX-Ph-NH₂ with [¹⁷⁷Lu]-Lu³⁺ showed highly favorable results, achieving quantitative RCYs over a wide concentration range (10⁻³ to 10⁻⁶ M) at RT within 10 min. Notably, the maximal molar activity of [¹⁷⁷Lu][Lu(noneunpaX-Ph-NH₂)]⁻ was determined at 250 MBq/μmol, corresponding to a ligand-to-metal ratio of 174:1, and further human serum stability studies showed no change in radiochemical purity (RCP) over 7 days, Figure S120.

Bioconjugate Studies. As a proof of concept to assess the suitability of H₄noneunpaX for *in vivo* applications, two bioconjugates of H₄noneunpaX-Ph-NCS with different covalent linkers were prepared incorporating the SSTR2-targeting peptide Tyr³-TATE for evaluation in mice bearing AR42J exocrine/pancreatic tumor xenografts. Tyr³-TATE was selected as an appropriate model targeting vector for NETs and to allow direct comparison to the clinically applied radiotherapeutic [¹⁷⁷Lu]Lu-DOTA-TATE.²⁴

Synthesis of H₄noneunpaX-Ahx/PEG₂-Tyr³-TATE. Synthesis of the linear resin-bound Tyr³-TATE peptides was carried out using standardized Fmoc-based semiautomated solid-phase peptide synthesis (SPPS) on preloaded Wang resin, using an analogous approach to that reported by Noor et al.³³ Deprotection of N^α-Fmoc protecting groups was achieved by treatment with 20% piperidine in DMF (2 × 15 mL). N^α-Fmoc-protected amino acids were coupled to the N-terminus of the linear peptide after preactivation with 1-hydroxybenzotriazole (HOBt) and 2-(1*H*-benzotriazol-1-yl)-1,1,3,3-tetramethyluronium hexafluorophosphate (HBTU), using diisopropylethylamine (DIPEA) as the base. The resin-bound linear peptide was prepared according to the sequence: [D¹Phe-Cys(ACM)-Tyr(tBu)-D¹Trp(tBu)-Lys(Boc)-Thr(tBu)-Cys(ACM)-Thr(tBu)-OH], Scheme 3. After preparation of the resin-bound octapeptide sequence, N^α-Fmoc-Ahx-CO₂H or N^α-Fmoc-PEG-CO₂H were incorporated as covalent linkers to give the

Fmoc-protected linear peptides **14** and **15**, respectively. Cyclization of the linear peptides was achieved by treatment with iodine in DMF, which sequentially removes the acetamido methyl (ACM) protecting groups and mediates the formation of the disulfide bridge between Cys² and Cys⁷. Global deprotection and cleavage from the resin was carried out using a standardized TFA cleavage cocktail to give the cyclized Fmoc-protected peptides **16** and **17**, which were isolated by RP-HPLC. To allow selective functionalization of the N-terminus of each peptide, the side chain primary amine group on Lys⁵ was first protected using Boc₂O prior to N^α-Fmoc cleavage with 20% piperidine in DMF to give compounds **18** and **19**. This approach maximized the purity of the Tyr³-TATE peptides prior to incorporating the bifunctional chelator. Conjugation of H₄noneunpaX-Ph-NCS to the free N-termini on each of **18** and **19** was achieved under mild, basic conditions in solution, and final cleavage of the N(Boc)-Lys⁵ protecting group gave the corresponding chelate-peptide bioconjugates **20** and **21**. H₄noneunpaX-Ahx-Tyr³-TATE (**20**) and H₄noneunpaX-PEG₂-Tyr³-TATE (**21**) were purified via RP-HPLC and mass spectrometric analyses (ESI/MALDI) to confirm isolation of the intended products.

Radiolabeling Studies of Chelate Bioconjugates. Concentration-dependent radiolabeling of H₄noneunpaX-Ahx-Tyr³-TATE and H₄noneunpaX-PEG₂-Tyr³-TATE was evaluated with [¹⁵⁵Tb]Tb³⁺ and [²²⁵Ac]Ac³⁺, Figure 8. Each of the chelate bioconjugates attained quantitative RCYs at a concentration of 10⁻⁵ M within 10 min at ambient temperature. Assessment of the serum stability for each of the radiolabeled bioconjugates showed excellent stability over the course of the study, with no significant changes in radiochemical purity from the initial time-points.

Log D_{7.4} Measurements. Prior to assessing radiotracer performance *in vivo*, the lipophilicity of the radiolabeled chelate bioconjugates was determined through measurement of the distribution coefficients between *n*-octanol and PBS (0.01 M,

pH 7.4), Table 4. All four radiolabeled tracers are moderately hydrophilic with log $D_{7.4}$ values ranging from -1.93 to -2.59 ,

Table 4. Distribution Coefficients (Log $D_{7.4}$) for H_4 noneunpaX-Ahx-Tyr³-TATE and H_4 noneunpaX-PEG₂-Tyr³-TATE Labeled with [²²⁵Ac]Ac³⁺ and [¹⁵⁵Tb]Tb³⁺, Measured between PBS and *n*-octanol ($n = 5-6$)

compound	log $D_{7.4}$
[²²⁵ Ac]Ac-noneunpaX-Ahx-Tyr ³ -TATE	-1.93 ± 0.08
[²²⁵ Ac]Ac-noneunpaX-PEG ₂ -Tyr ³ -TATE	-2.51 ± 0.09
[¹⁵⁵ Tb]Tb-noneunpaX-Ahx-Tyr ³ -TATE	-2.01 ± 0.06
[¹⁵⁵ Tb]Tb-noneunpaX-PEG ₂ -Tyr ³ -TATE	-2.59 ± 0.04

comparable to reports for [¹⁶¹Tb]Tb-DOTA-LM3 (log $D_{7.4} = -2.5 \pm 0.1$), an SSTR2 antagonist analogue of DOTA-TATE.⁵⁴ As anticipated, the higher lipophilicity of the aliphatic hexyl covalent linker is reflected in the log $D_{7.4}$ measurements, with both Ahx-Tyr³-TATE tracers being more lipophilic than the PEG₂-Tyr³-TATE derivatives. Notably, interchange between [¹⁵⁵Tb]Tb³⁺ and [²²⁵Ac]Ac³⁺ did not have a significant impact on the log $D_{7.4}$ values for either bioconjugate, which may indicate a comparable biodistribution profile in vivo using this theranostic pair.

Preclinical In Vivo Studies. To assess the suitability of ¹⁵⁵Tb as an imaging companion for ²²⁵Ac, in vivo SPECT/CT studies of the two ¹⁵⁵Tb-labeled conjugates were performed in male NRG mice bearing AR42J tumor xenografts. Both radiotracers were prepared at high molar activity (~ 23.6 MBq/nmol) with a high radiochemical purity ($>98\%$) as confirmed by iTLC and radio-HPLC. For in vivo SPECT/CT studies, mice were administered with 13.5 MBq (0.572 nmol/animal) of each radiotracer, while biodistribution studies were performed using 0.80 MBq (0.033 nmol/animal).

SPECT/CT scans of mice bearing AR42J tumor xenografts were acquired over the first 1.5 h post administration to assess the pharmacokinetic profile of both ¹⁵⁵Tb-labeled radiotracers, Figure 9. Further static SPECT/CT images were recorded at 3, 5, and 24 h post administration, Figure 10, and mean standardized uptake values (SUV_{mean}) for regions of interest (ROIs) were extracted from the quantitative images to generate time-activity curves for each radiotracer, Figure 11. The quantitative imaging studies enabled direct measurement of the activity concentrations (% ID/g) in ROIs in the SPECT/CT scans and are directly comparable to the ex vivo biodistribution results determined after sacrificing the mice following acquisition of the final SPECT/CT scans (24 h p.i.).

In both cases, the ¹⁵⁵Tb-labeled radiotracers exhibit fast clearance from blood circulation over the first hour after

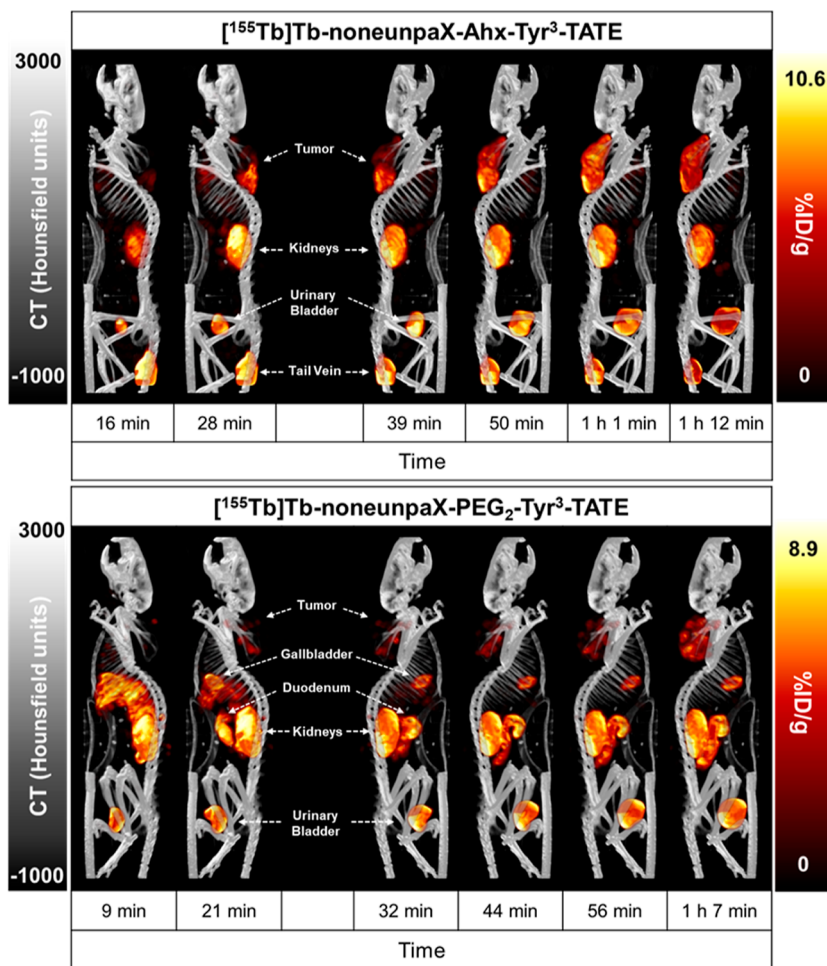


Figure 9. Transverse viewpoints of maximum intensity projections (MIPs) from quantitative SPECT/CT scans at 0–1.5 h post administration of [¹⁵⁵Tb]Tb-noneunpaX-Ahx-Tyr³-TATE (top) and [¹⁵⁵Tb]Tb-noneunpaX-PEG₂-Tyr³-TATE (bottom) in male NRG mice bearing AR42J exocrine tumor xenografts (left shoulder).

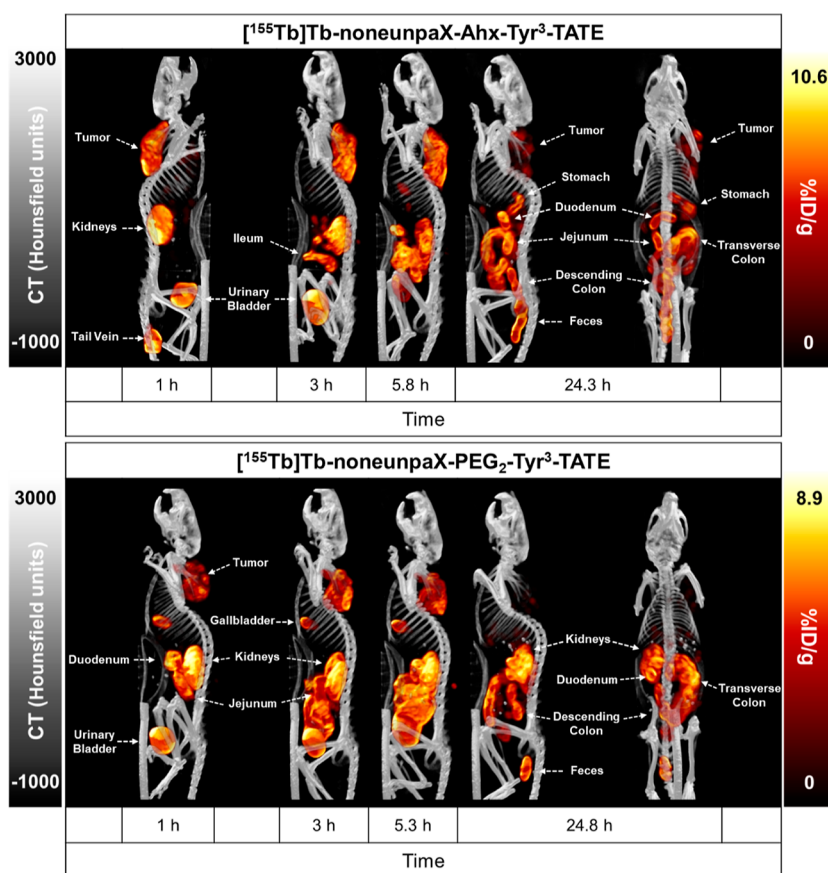


Figure 10. Transverse views of MIPs from SPECT/CT scans at 1, 3, 5, and 24 h post administration of $[^{155}\text{Tb}]\text{Tb-noneunpaX-Ahx-Tyr}^3\text{-TATE}$ (top) and $[^{155}\text{Tb}]\text{Tb-noneunpaX-PEG}_2\text{-Tyr}^3\text{-TATE}$ (bottom) in male NRG mice bearing AR42J pancreatic exocrine tumor xenografts (left shoulder).

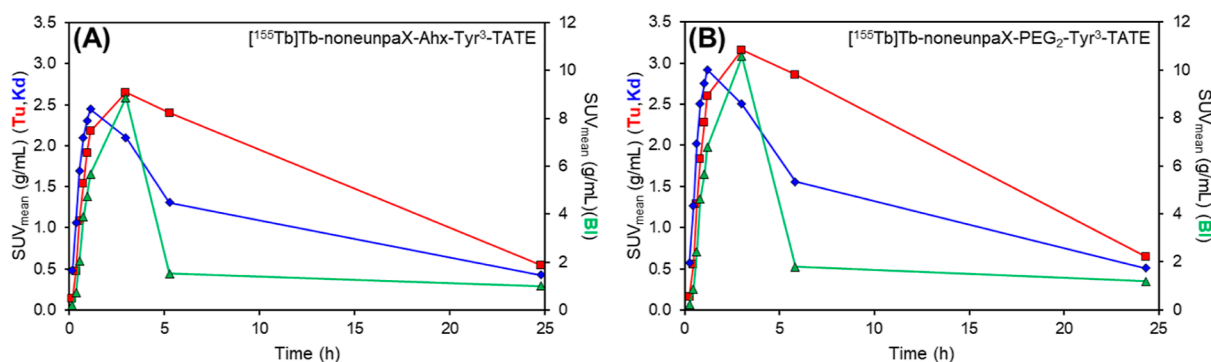


Figure 11. Representative time-activity plots of (A) $[^{155}\text{Tb}]\text{Tb-noneunpaX-Ahx-Tyr}^3\text{-TATE}$ and (B) $[^{155}\text{Tb}]\text{Tb-noneunpaX-PEG}_2\text{-Tyr}^3\text{-TATE}$ in male NRG mice bearing AR42J exocrine/pancreatic tumor xenografts. SUVs were extracted for ROIs in the tumor (Tu), kidneys (Kd), and bladder (Bl) from the calibrated SPECT/CT images.

administration, with uptake in the tumor beginning within 10–15 min p.i. Comparatively, the two tracers exhibited similar distribution profiles, with tumor uptake peaking at 3 h p.i. for both $[^{155}\text{Tb}]\text{Tb-noneunpaX-Ahx-Tyr}^3\text{-TATE}$ ($\text{SUV}_{\text{mean}} = 3.16 \text{ g/mL}$, $\equiv 10.8\% \text{ ID/g}$) and $[^{155}\text{Tb}]\text{Tb-noneunpaX-PEG}_2\text{-Tyr}^3\text{-TATE}$ ($\text{SUV}_{\text{mean}} = 2.65 \text{ g/mL}$, $\equiv 9.0\% \text{ ID/g}$), which is sustained up to 6 h p.i. Both tracers followed the pharmacokinetic profile observed for hydrophilic octreotate-based bioconjugates, where fast clearance and accumulation in the kidneys and bladder is seen.^{55,56}

Clearance of both radiotracers occurs predominantly through the renal pathway, as observed by high uptake in the kidneys

and bladder and low uptake in the liver. The SPECT/CT images show additional clearance via the biliary tract, whereby an increase in activity is seen in the gallbladder beginning at 3 h p.i., with subsequent uptake in the small intestines (duodenum, jejunum) at later time-points. This additional elimination pathway may account for the sustained tumor uptake over 1–3 h, in contrast to $[^{177}\text{Lu}]\text{Lu-DOTA-TATE}$,⁵⁵ due to reabsorption of the radiotracers in the gastrointestinal tract (enterohepatic circulation), which is seen in drugs exhibiting clearance in the bile.⁵⁷ At later time points (24 h p.i.), both ^{155}Tb -labeled tracers are cleared through the gastrointestinal tract, as visualized by activity in the jejunum, colon, and feces.

From the time-activity curves, it is clearly seen that each tracer exhibits a comparable pharmacokinetic profile, with [^{155}Tb]Tb-noneunpaX-PEG₂-Tyr³-TATE showing moderately higher renal excretion compared to [^{155}Tb]Tb-noneunpaX-Ahx-Tyr³-TATE, which may be explained by the difference in hydrophilicity of each radiotracer.

SSTR2 is expressed at low levels in several normal healthy tissues, including the pancreas, lungs, stomach, intestines, adrenal glands, and kidneys, which are clearly visualized in the SPECT/CT images and biodistribution data determined for each tracer, Figure 12. Significantly, lower accumulations were

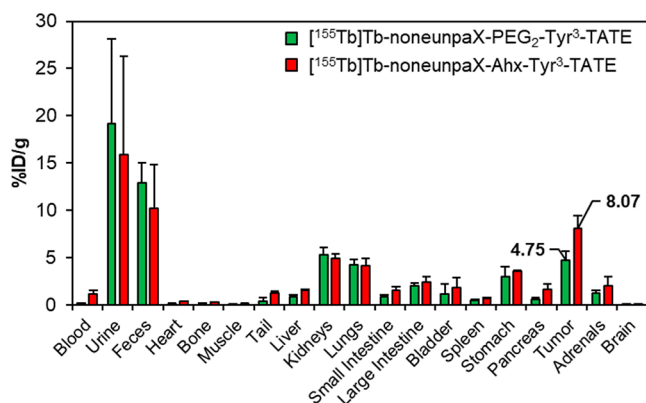


Figure 12. Decay-corrected biodistribution studies of [^{155}Tb]Tb-noneunpaX-Ahx-Tyr³-TATE and [^{155}Tb]Tb-noneunpaX-PEG₂-Tyr³-TATE at 5 h post injection in male NRG mice ($n = 4$) bearing AR42J exocrine/pancreatic tumor xenografts.

observed in the pancreas (1.63 ± 0.46 and $0.60 \pm 0.11\%$ ID/g), lungs (4.14 ± 0.68 and $4.27 \pm 0.45\%$ ID/g), and adrenal glands (2.03 ± 0.77 and $1.23 \pm 0.24\%$ ID/g) at 5 h post injection for [^{155}Tb]Tb-noneunpaX-Ahx-Tyr³-TATE and [^{155}Tb]Tb-noneunpaX-PEG₂-Tyr³-TATE, respectively, compared to [^{177}Lu]Lu-DOTA-TATE [pancreas (10.9% ID/g), lungs (17.4% ID/g), and adrenal glands (8.95% ID/g)].⁵⁵ However, similar uptake in the kidneys (4.93 ± 0.40 and $5.29 \pm 0.66\%$ ID/g) was seen compared to [^{177}Lu]Lu-DOTA-TATE (6.31% ID/g).⁵⁵ [^{155}Tb]Tb-noneunpaX-Ahx-Tyr³-TATE showed higher, statistically significant tumor uptake at 5 h p.i. than [^{155}Tb]Tb-noneunpaX-PEG₂-Tyr³-TATE (8.07 ± 1.39 vs $4.75 \pm 0.99\%$ ID/g, respectively; t -test, $p = 0.014$).

The primary objectives of these studies were to evaluate the in vivo suitability of H₄noneunpaX as a new bifunctional chelating ligand and learn about the implications of a “syn”- vs “anti”- constitutional arrangement of the chelating arms. Overall, the imaging and biodistribution studies show excellent initial results for this chelator, with no evidence of degradation in vivo or release of bound activity, which would be seen as uptake in the bone marrow overtime. In addition, both Tyr³-TATE analogues show improved pharmacokinetics with lower nontarget tissue accumulation compared to [^{177}Lu]Lu-DOTA-TATE.⁵⁵

CONCLUSIONS

A new nonadentate chelating ligand, H₄noneunpaX, was synthesized to investigate the influence of an unusual, inverted donor group arrangement on metal binding characteristics within the “NON backbone”. Characterization of the metal complexation of H₄noneunpaX through NMR spectroscopy, mass spectrometry, radiolabeling, solution thermodynamic

stability studies, and DFT calculations showed excellent compatibility with a wide range of large trivalent metal cations, with a particular preference for hard lanthanide and actinide ions. The radiolabeling properties of H₄noneunpaX were assessed with [^{44}Sc]Sc³⁺, [^{111}In]In³⁺, [^{155}Tb]Tb³⁺, [^{177}Lu]Lu³⁺, [^{213}Bi]Bi³⁺, and [^{225}Ac]Ac³⁺, demonstrating quantitative RCYs within 10 min at ambient temperature and achieving notably high molar activities with [^{111}In]In³⁺ ($54\text{ GBq}/\mu\text{mol}$), [^{155}Tb]Tb³⁺ ($1.0\text{ GBq}/\mu\text{mol}$), [^{177}Lu]Lu³⁺ ($2.0\text{ GBq}/\mu\text{mol}$), and [^{225}Ac]Ac³⁺ ($134\text{ MBq}/\mu\text{mol}$). The reactivity trends were found to be highly comparable to the structural related “anti”-constitutional isomer, H₄noneunpa, achieving similar RCYs and molar activities. The kinetic inertness of each metal complex was determined via serum challenge studies, which showed excellent in vitro stability ($>95\%$ RCP over 5–7 days), with the exception of [^{225}Ac]Ac(noneunpa)[−], which showed a reduction in integrity over time ($\sim 10\%$ degradation), while [^{225}Ac]Ac(noneunpaX)[−] maintained high radiochemical integrity ($>99\%$ RCP over 7 days), thereby showing a small influence between chelate structural arrangements on complex stability. Solution thermodynamic stability studies showed the formation of highly stable metal complexes with H₄noneunpaX, whereby a single dominant species (ML[−]) was observed over a broad pH range (pH = 3.5–11.5) on complexation with the lanthanide series. High stability constants were determined for each of the metal complexes, indicating highly effective metal scavenging ability.

A bifunctional analogue of H₄noneunpaX was prepared using a simple, versatile, and scalable synthetic approach and the complexation properties reassessed, showing comparable characteristics to the unmodified chelator. Dose escalation studies of bifunctional H₄noneunpaX-Ph-NH₂ with [^{177}Lu]Lu³⁺ demonstrated highly competitive radiolabeling with notably high molar activities ($250\text{ GBq}/\mu\text{mol}$). A pilot study involving two Tyr³-TATE peptides conjugated to H₄noneunpaX demonstrated the effectiveness of the new chelate for radiopharmaceuticals targeting SSTR2 positive tumors. Radiolabeling studies of the two bioconjugates showed a small decrease in efficiency compared to the free chelate, which is typical for chelate-peptide conjugates, but nevertheless they still achieved high RCYs at low concentration with high molar activities. Preliminary longitudinal SPECT/CT imaging, pharmacokinetics, and biodistribution studies were undertaken with [^{155}Tb]Tb-radiolabeled H₄noneunpaX-Ahx-Tyr³-TATE and H₄noneunpaX-PEG₂-Tyr³-TATE in male NRG mice bearing AR42J tumor xenografts. Both radiolabeled bioconjugates showed good in vivo performance, with no evident degradation over the course of the study and good tumor uptake ([^{155}Tb]Tb-noneunpaX-Ahx-Tyr³-TATE (SUV_{mean} = 3.16 g/mL , $\equiv 10.8\%$ ID/g) and [^{155}Tb]Tb-noneunpaX-PEG₂-Tyr³-TATE (SUV_{mean} = 2.65 g/mL , $\equiv 9.0\%$ ID/g) at 3 h). The biodistribution profile of each radiotracer showed the typical expected clearance profile of SSTR2 targeting tracers (i.e., [^{177}Lu]Lu-DOTA-TATE), with elimination primarily through the renal pathway, with uptake in the kidneys and bladder, followed by elimination in the urine.

Ultimately, these studies highlight H₄noneunpaX as an important advance in chelating ligands, with beneficial characteristics for radiometal-based pharmaceuticals and an important adjunct to its “anti” constitutional isomer H₄noneunpa. The mild radiolabeling conditions and high kinetic inertness exhibited by H₄noneunpaX with several high value radiometal ions (^{225}Ac , ^{177}Lu , ^{155}Tb , ^{111}In) is a major

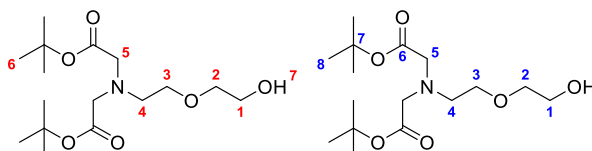
advantage over conventional chelators (DOTA). Currently, in the field of nuclear medicine, a major challenge is the lack of effective chelators, which can be radiolabeled interchangeably with ^{225}Ac and suitable diagnostic radionuclides for dosimetry evaluations, with the most promising ligands for ^{225}Ac (e.g., macropa) being incompatible with conventional imaging radiometals. $\text{H}_4\text{noneunpaX}$ has high potential to address this challenge and enable the routine application of targeted alpha therapy (^{225}Ac) with simultaneous diagnostic imaging (^{155}Tb) and will be particularly beneficial for radiopharmaceuticals incorporating thermally sensitive biological targeting vectors, such as antibodies. The synthetic strategy developed for bifunctional $\text{H}_4\text{noneunpaX}$ utilizes a convenient and adaptable approach, which can enable simple interchange of bifunctional handles and covalent linkers, a highly advantageous characteristic for radiopharmaceutical optimization and tuning of pharmacokinetic properties. While the SSTR2 targeting bioconjugates reported did not show a significant improvement over conventional radiopharmaceuticals (DOTATATE, DOTATOC), the in vivo viability of this new chelator was established and will be further investigated using different conjugation methods and new targeting vectors in future studies.

EXPERIMENTAL SECTION

Materials and Methods. All solvents and reagents were purchased from commercial suppliers (Sigma-Aldrich, AK Scientific, Alfa Aesar) and were used directly without further purification. Analytical thin-layer chromatography (TLC) sheets were purchased from Merck (TLC Silica gel 60 F254, aluminum sheet). Deionized H_2O (18.2 $\text{M}\Omega/\text{cm}$ at 25 $^\circ\text{C}$) was obtained from a PURELAB Ultra water purification system, ELGA LabWater. Flash column chromatography was performed using Siliaflash F60 silica gel (60 \AA , 40–63 μm particle size, 230–400 mesh) from Silicycle Inc. Automated column chromatography was performed using a Teledyne Isco (Lincoln, NE) CombiFlash Rf automated purification system equipped with RediSep Rf Gold HP prepacked reusable silica and neutral alumina column cartridges. Low-resolution mass spectrometry was performed using a Waters 2965 ZQ spectrometer with an electrospray/chemical ionization (ESI/CI) source. High-resolution mass spectrometry (HR-MS) was performed using a Waters Micromass LCT TOF instrument. Elemental analyses (CHN) were carried out using a ThermoFlash 2000 elemental analyzer. ^1H and $^{13}\text{C}\{^1\text{H}\}$ NMR spectra were recorded using Bruker AV300 and AV400 spectrometers; all spectra are reported on the delta scale referenced to residual solvent peaks. Analytical high-performance liquid chromatography (HPLC) and semipreparative HPLC were carried out using a Waters 600 system equipped with a Waters 2487 dual wavelength absorbance detector monitoring at 254 and 210 nm and a Phenomenex Synergi 250 $\text{mm} \times 21.2 \text{ mm} \times 4 \mu\text{m}$ hydro-RP80 \AA column (10 mL/min). All HPLC methods employed a $\text{H}_2\text{O}/\text{MeCN}$ biphasic solvent system buffered with 0.1% TFA. HPLC solvent system 1 (A: H_2O (0.1% TFA), B: MeCN (0.1% TFA), HPLC solvent system 2: (A: H_2O (0.01% TFA), B: MeCN). [^{44}Sc] Sc^{3+} ($t_{1/2} = 3.97 \text{ h}$) was produced at TRIUMF via proton irradiation of ^{nat}Ca targets with 12.8 MeV protons.³⁹ [^{111}In] In^{3+} ($t_{1/2} = 2.83 \text{ days}$) (purchased from BWX Technologies) was produced by proton irradiation (Advanced Cyclotron Systems, model TR30) via the $^{111}\text{Cd}(\text{p,n})^{111}\text{In}$ reaction and provided as a 0.05 M HCl solution. [^{155}Tb] Tb^{3+} ($t_{1/2} = 5.32 \text{ days}$) was produced at TRIUMF via irradiation of tantalum targets with 500 MeV protons, followed by directed isotope separation online and implantation into NH_4Cl layered aluminum disks.⁵⁸ [$^{132/135}\text{La}$] La^{3+} ($t_{1/2} = 19.5 \text{ h}$) was produced at TRIUMF via irradiation of ^{nat}Ba targets with 12.8 MeV protons using a similar approach to the methods reported by Aluicio-Sarduy et al.⁵⁹ [^{177}Lu] Lu^{3+} ($t_{1/2} = 6.67 \text{ days}$) was obtained from ITM Medical Isotopes GmbH Germany as a 0.05 M HCl solution. [^{213}Bi] Bi^{3+} was obtained from an in-house $^{225}\text{Ac}/^{213}\text{Bi}$ generator constructed using the

AG-MP-50 cation exchange resin, based on published methodologies.⁶⁰ [^{225}Ac] Ac^{3+} ($t_{1/2} = 10.0 \text{ days}$) was produced at TRIUMF via the spallation of ^{232}Th targets with 500 MeV protons and purified as previously reported.⁶¹ Radiolabeling of compounds was assessed via instant thin-layer chromatography (iTLC) using silicic acid (SA)-impregnated paper TLC plates sourced from Agilent technologies. TLC imaging was performed using an AR-2000 imaging scanner equipped with P-10 gas, and subsequent analysis of radiochemical conversion was carried out using WinScan V3.14 software. Radio-HPLC was carried out using an Agilent 1200 instrument equipped with a Phenomenex Synergi 4 μm 250 $\text{mm} \times 4.6 \text{ mm}$ hydro-RP 80 \AA column. Radioactivity was quantified using a calibrated high-purity germanium (HPGe) detector (Mirion Technologies (Canberra) Inc.) with Genie 2000 software. All work with radionuclides at TRIUMF was undertaken in shielded fume hoods to minimize dose to experimenters (and special precautions were used to prevent contamination) under nuclear energy worker status earned by attending TRIUMF's Advanced Radiation Protection course and passing the final exam. Peptides were prepared using an AAPPTec Focus Xi semiautomated solid phase peptide synthesizer. SPECT/CT studies were performed using a multimodal VECTOR/CT system (MILabs, The Netherlands) in combination with an extra ultrahigh sensitivity (XUHS) 2 mm pinhole collimator. Image analysis was performed using AMIDE (v. 1.0.4) software.⁶²

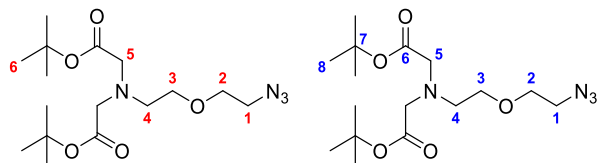
$\text{H}_4\text{noneunpaX}$. Di-*tert*-Butyl 2,2'-((2-(2-Hydroxyethoxy)ethyl)azanediyl)diacetate (2). *tert*-Butyl bromoacetate (4.30 mL, 5.57 g, 28.6 mmol) was added slowly to a solution of 2-(2-aminoethoxy)ethanol-1-ol (1) (1.53 g, 14.3 mmol) and diisopropylethylamine (5.00 mL, 3.69 g, 28.6 mmol) dissolved in dry MeCN (150 mL). The reaction mixture was heated to 50 $^\circ\text{C}$ and stirred overnight. The volatiles were then removed in vacuo and the resulting residue redissolved in EtOAc (150 mL). After standing for 10 min at RT, the resulting white precipitate was removed via vacuum filtration, washed with cool EtOAc (50 mL), and discarded. The filtrate was washed with deionized water ($3 \times 150 \text{ mL}$), and the combined aqueous phase back-extracted with EtOAc ($2 \times 150 \text{ mL}$). The combined organics were evaporated in vacuo to yield the title compound as a pale-yellow oil (4.69 g, 99%). $R_f = 0.50$ ($\text{CH}_2\text{Cl}_2/\text{MeOH}$, 95:5 Si-Al TLC). ^1H NMR (300 MHz, CDCl_3 , 298 K) 3.66 (2H, t, $J = 4.6 \text{ Hz}$, 1- CH_2), 3.60 (2H, t, $J = 5.2 \text{ Hz}$, 3- CH_2), 3.52 (2H, t, $J = 4.6 \text{ Hz}$, 2- CH_2), 3.47 (4H, s, 5- CH_2), 2.96 (1H, br s, 7-OH), 2.92 (2H, t, $J = 5.2 \text{ Hz}$, 4- CH_2), 1.42 (18H, s, 6- $\text{C}(\text{CH}_3)_3$). $^{13}\text{C}\{^1\text{H}\}$ NMR (75 MHz, CDCl_3 , 298 K) 171.0 (6-C), 81.2 (7-C), 72.4 (2-C), 70.2 (3-C), 61.9 (1-C), 56.8 (5-C), 53.4 (4-C), 28.3 (8-C). ESI-MS (MeOH) 334.26 [$\text{C}_{16}\text{H}_{31}\text{NO}_6 + \text{H}$] $^+$.



Compound (2) with ^1H and ^{13}C NMR assignments, red and blue, respectively.

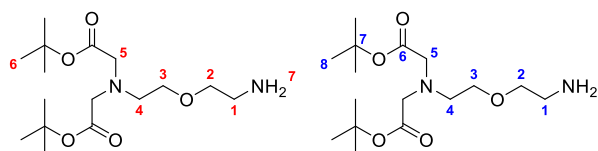
Di-*tert*-Butyl 2,2'-((2-(2-Azidoethoxy)ethyl)azanediyl)diacetate (3). Methanesulfonyl chloride (1.34 mL, 1.98 g, 17.3 mmol) was added slowly to a solution of di-*tert*-butyl 2,2'-((2-(2-hydroxyethoxy)ethyl)azanediyl)diacetate (2) (5.26 g, 15.7 mmol) and diisopropylethylamine (3.01 mL, 2.24 g, 17.3 mmol) in EtOAc (15 mL) at 0 $^\circ\text{C}$. After 10 min, the suspension was warmed to RT and stirred for a further 3 h. Upon completion, the suspension was cooled to 0 $^\circ\text{C}$ and the white solid separated by vacuum filtration. The filtrate was diluted with EtOAc (50 mL) and washed with deionized H_2O ($3 \times 50 \text{ mL}$). The organic phase was dried over Na_2SO_4 and evaporated in vacuo to yield the corresponding mesylate as a pale-yellow oil [$R_f = 0.65$ ($\text{CH}_2\text{Cl}_2/\text{MeOH}$, 95:5, Si-Al TLC)], which was used without further purification. NaN_3 (3.08 mg, 47.2 mmol) was added to a solution of crude mesylate dissolved in dry DMF (20 mL) and the suspension heated at 80 $^\circ\text{C}$ O/N. Upon completion, the solution was cooled to RT and diluted with deionized H_2O (50 mL). The aqueous phase was extracted with CH_2Cl_2 ($3 \times 50 \text{ mL}$) and the combined organics washed with 5% LiCl aq sol (50 mL). The volatiles were removed in

vacuo and the resulting residue purified via silica gel chromatography (CombiFlash R_f automated purification system; 40 g HP silica RediSep Gold cartridge; A: CH_2Cl_2 , B: MeOH; 100% A to 5% B; product elution: 2.5% MeOH). The title compound was attained as a pale-yellow oil (3.25 g, 58%). R_f = 0.90 (CH_2Cl_2 /MeOH, 95:5, Si-Al TLC; KMnO_4 strain: yellow spot). ^1H NMR (300 MHz, CDCl_3 , 298 K) 3.62–3.57 (4H, m, 2- and 3- CH_2), 3.46 (4H, s, 5- CH_2), 3.33 (2H, t, J = 5.0 Hz, 1- CH_2), 2.92 (2H, t, J = 5.6 Hz, 4- CH_2), 1.42 (18H, s, 6- $(\text{C}(\text{CH}_3)_3)$). ^{13}C $\{^1\text{H}\}$ NMR (75 MHz, CDCl_3 , 298 K) 170.9 (6-C), 81.0 (7-C), 70.9 (2-C), 69.8 (3-C), 56.9 (5-C), 53.6 (4-C), 50.8 (1-C), 28.3 (8-C). ESI-MS (MeOH) 359.21 [$\text{C}_{16}\text{H}_{30}\text{N}_4\text{O}_5 + \text{H}$] $^+$.



Compound (3) with ^1H and ^{13}C NMR assignments, red and blue, respectively.

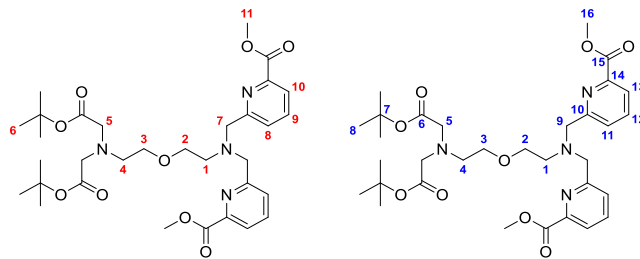
Di-tert-Butyl 2,2'-((2-(2-Aminoethoxy)ethyl)azanediyl)diacetate (4). Di-tert-butyl 2,2'-((2-(2-aminoethoxy)ethyl)azanediyl)diacetate (3) (2.81 g, 7.85 mmol) was dissolved in dry THF (30 mL) and cooled to 0 $^\circ\text{C}$. PPh_3 (2.47 g, 9.42 mmol) was added slowly to the reaction mixture under Ar and the resulting solution allowed to warm to RT and stirred for 5 h. The resulting solution was then added dropwise into deionized H_2O (350 mL) and the suspension stirred overnight. The THF was removed in vacuo and the off-white suspension left to precipitate at RT for 1 h. The white precipitate was removed via vacuum filtration and the aqueous phase concentrated to ~100 mL in vacuo. The aqueous phase was extracted with CH_2Cl_2 (4 \times 75 mL) and the combined organic phase evaporated in vacuo to give the title compound as a pale-yellow oil (2.38 g, 91%). R_f = 0.0 (CH_2Cl_2 /MeOH, 95:5, Si-Al TLC; Ninhydrin strain: purple spot). ^1H NMR (300 MHz, CDCl_3 , 298 K) 6.72 (3H, br s, 7- NH_2), 3.71 (2H, t, J = 4.5 Hz, 2- CH_2), 3.58 (2H, t, J = 5.1 Hz, 3- CH_2), 3.45 (4H, s, 5- CH_2), 3.10 (2H, t, J = 4.5 Hz, 1- CH_2), 2.91 (2H, t, J = 5.1 Hz, 4- CH_2), 1.42 (18H, s, 6- $(\text{C}(\text{CH}_3)_3)$). ^{13}C $\{^1\text{H}\}$ NMR (75 MHz, CDCl_3 , 298 K) 171.0 (6-C), 81.6 (7-C), 68.8 (2-C), 67.9 (3-C), 56.2 (5-C), 53.3 (4-C), 40.5 (1-C), 28.3 (8-C). ESI-MS (MeOH) 333.19 [$\text{C}_{16}\text{H}_{32}\text{N}_2\text{O}_5 + \text{H}$] $^+$.



Compound (4) with ^1H and ^{13}C NMR assignments, red and blue, respectively.

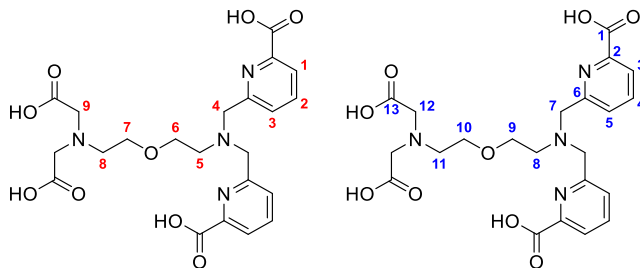
($t\text{Bu}$) $_2(\text{Me})_2\text{noneunpaX}$ (5). Methyl (6-bromomethyl) picolinate (515 mg, 2.82 mmol) was added to a solution of di-tert-butyl 2,2'-((2-(2-aminoethoxy)ethyl)azanediyl) diacetate (4) (372 mg, 1.12 mmol) in dry MeCN (15 mL) under argon. Diisopropylethylamine (585 μL , 434 mg, 3.36 mmol) was added and the resulting pale-yellow solution stirred for 1 h at ambient temperature. The reaction mixture was subsequently heated to 50 $^\circ\text{C}$ and stirred overnight. The volatiles were then removed in vacuo, and the resulting residue was redissolved in CH_2Cl_2 (25 mL). The organic phase was washed with deionized H_2O (3 \times 25 mL) and brine (25 mL), dried over Na_2SO_4 , and evaporated in vacuo. The crude residue was purified via flash column chromatography on neutral alumina (CombiFlash R_f automated purification system; 24 g RediSep R_f alumina neutral cartridge; A: CH_2Cl_2 , B: MeOH; 100% A to 10% B; product elution: 5–8% MeOH). The product was attained as a pale-yellow oil (459 mg, 65%). R_f = 0.25 (CH_2Cl_2 /MeOH, 95:5, Alumina (N) TLC). ^1H NMR (300 MHz, CDCl_3 , 298 K) 7.90 (2H, dd, 3J = 7.3 Hz, 4J = 1.1 Hz, 10-CH), 7.80 (2H, dd, 3J = 8.1 Hz, 4J = 1.4 Hz, 8-CH), 7.75 (2H, t, 3J = 7.5 Hz, 9-CH), 3.94 (4H, s, 7- CH_2), 3.90 (6H, s, 11- CH_3), 3.49 (2H, t, 3J = 5.6 Hz, 2- CH_2), 3.44 (2H, t, 3J = 5.8 Hz, 3- CH_2), 3.40 (4H, s, 5- CH_2), 2.84 (2H, t, 3J = 5.8 Hz, 4- CH_2), 2.74 (2H, t, 3J = 5.6 Hz, 1- CH_2), 1.35

(18H, s, 6- $(\text{C}(\text{CH}_3)_3)$). ^{13}C $\{^1\text{H}\}$ NMR (75 MHz, CDCl_3 , 298 K) 170.8 (6-C), 165.9 (15-C), 160.8 (10-C), 147.3 (14-C), 137.5 (12-C), 126.1 (11-C), 123.6 (13-C), 80.9 (7-C), 70.5 (3-C), 69.4 (2-C), 60.9 (9-C), 56.7 (5-C), 54.1 (1-C), 53.6 (4-C), 52.9 (16-C), 28.2 (8-C). ESI-MS (MeOH) 653.3 [$\text{C}_{32}\text{H}_{46}\text{N}_4\text{O}_9 + \text{Na}$] $^+$.



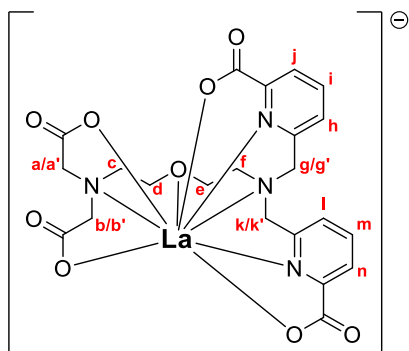
Compound (5) with ^1H and ^{13}C NMR assignments, red and blue, respectively.

$\text{H}_4\text{noneunpaX} \cdot 4\text{HCl} \cdot 5\text{H}_2\text{O}$ (6). ($t\text{Bu}$) $_2(\text{Me})_2\text{noneunpaX}$ (5) (168 mg, 0.257 mmol) was dissolved in 4 M HCl (5 mL) and heated at 60 $^\circ\text{C}$ overnight. The volatiles were removed in vacuo and the resulting off-white solid purified via RP-HPLC (A: H_2O (0.1% TFA), B: MeCN; 100% A to 20% B, 30 min, t_R ~ 21.5 min). Pure $\text{H}_4\text{noneunpaX}$ was attained as a white HCl salt (146 mg, 87%) by coevaporation with 3 M HCl. ^1H NMR (400 MHz, D_2O , 298 K) 7.95 (2H, d, 3J = 7.7 Hz, 1-CH), 7.89 (2H, t, 3J = 7.7 Hz, 2-CH), 7.57 (2H, d, 3J = 7.7 Hz, 3-CH), 4.76 (4H, s, 4- CH_2), 4.21 (4H, s, 9- CH_2), 3.94 (2H, t, 3J = 4.4 Hz, 6- CH_2), 3.84 (2H, t, 3J = 4.4 Hz, 7- CH_2), 3.75 (2H, t, 3J = 4.4 Hz, 5- CH_2), 3.63 (2H, t, 3J = 4.4 Hz, 8- CH_2). ^{13}C $\{^1\text{H}\}$ NMR (75 MHz, CDCl_3 , 298 K) 167.9 (13-C), 166.7 (1-C), 149.7 (2-C), 146.3 (6-C), 140.1 (3-C), 128.5 (5-C), 125.4 (4-C), 65.3 (10-C), 64.6 (9-C), 58.6 (7-C), 56.2 (11-C), 56.0 (8-C), 55.5 (12-C). ESI-MS (H_2O) 491.1 [$\text{C}_{22}\text{H}_{26}\text{N}_4\text{O}_9 + \text{H}$] $^+$. HR-ESI-MS (H_2O) calcd for [$\text{C}_{22}\text{H}_{26}\text{N}_4\text{O}_9 + \text{H}$] $^+$, 491.1700; found [$\text{M} + \text{H}$] $^+$, 491.1779. Elemental analysis: Calcd % for $\text{H}_4\text{noneunpaX} \cdot 4\text{HCl} \cdot 5\text{H}_2\text{O}$ ($\text{C}_{22}\text{H}_{26}\text{N}_4\text{O}_9 \cdot 4\text{HCl} \cdot 5\text{H}_2\text{O}$ = 726.178 g mol^{-1}): C, 37.59; H, 5.36; N, 7.97. Found: C, 37.65; H, 5.43; N, 7.97.



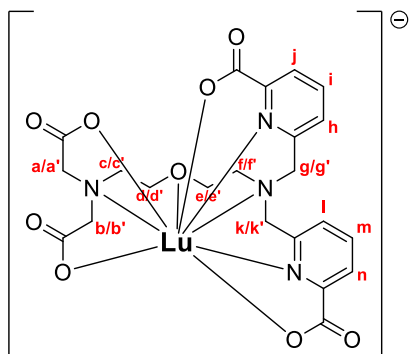
Compound (6) with ^1H and ^{13}C NMR assignments, red and blue, respectively.

Metal Complexation. $\text{Na}[\text{La}(\text{noneunpaX})]$. $\text{La}(\text{NO}_3)_3 \cdot 6\text{H}_2\text{O}$ (2.9 mg, 6.75 μmol , 1.0 equiv) was added directly to a solution of $\text{H}_4\text{noneunpaX} \cdot 4\text{HCl} \cdot 5\text{H}_2\text{O}$ (4.9 mg, 6.75 μmol , 1.0 equiv) in D_2O (300 μL). The solution was mixed thoroughly at 1000 rpm using a vortex mixer and the pH adjusted to ~7.0 using dilute NaOD solution to give the corresponding [$\text{La}(\text{noneunpaX})$] $^-$ complex as a sodium salt. The white precipitate was filtered and the filtrate characterized directly. ^1H NMR (400 MHz, D_2O , 298 K, pH 7.0) 7.87 (2H, t, 3J = 7.7 Hz, i- and m-CH), 7.77 (2H, d, 3J = 7.5 Hz, j- and n-CH), 7.42 (2H, d, 3J = 7.7 Hz, h- and l-CH), 4.19 (2H, d, 2J = 16.4 Hz, g'- and k'-CH), 3.93 (2H, d, 2J = 16.4 Hz, g- and k-CH), 3.53 (2H, t, 3J = 5.0 Hz, d- CH_2), 3.48 (2H, d, 3J = 4.9 Hz, e- CH_2), 3.37 (2H, d, 2J = 16.3 Hz, a'- and b'-CH), 3.31 (2H, d, 2J = 16.3 Hz, a- and b-CH), 3.04 (2H, br t, f- CH_2), 2.71 (2H, t, 3J = 5.0 Hz, c- CH_2). LR-ESI-MS (H_2O) 627.0 [$\text{C}_{22}\text{H}_{22}\text{LaN}_4\text{O}_9 + 2\text{H}$] $^+$, 624.8 [M] $^-$. HR-ESI-MS (H_2O) calcd for [$\text{C}_{22}\text{H}_{22}\text{LaN}_4\text{O}_9 + 2\text{H}$] $^+$, 627.0536; found [$\text{M} + 2\text{H}$] $^+$, 627.0600.



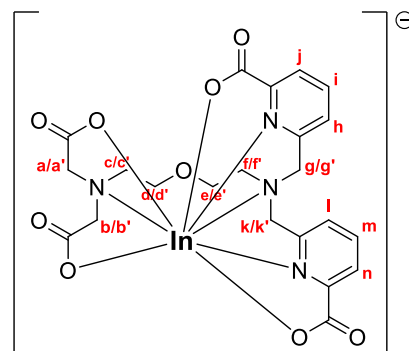
Chemical structure of $[\text{La}(\text{noneunpaX})]^-$ with ^1H NMR assignments indicated.

Na[Lu(noneunpaX)]. $\text{Lu}(\text{NO}_3)_3 \cdot \text{H}_2\text{O}$ (2.4 mg, 6.75 μmol , 1.0 equiv) was added directly to a solution of $\text{H}_4\text{noneunpaX} \cdot 4\text{HCl} \cdot 5\text{H}_2\text{O}$ (4.9 mg, 6.75 μmol , 1.0 equiv) in D_2O (300 μL). The solution was mixed thoroughly at 1000 rpm using a vortex mixer and the pD adjusted to ~ 6.5 using dilute NaOD solution to give $\text{Na}[\text{Lu}(\text{noneunpaX})]$. The solution was filtered and analyzed without additional purification. ^1H NMR (400 MHz, D_2O , 298 K, pD 6.5) 8.03 (1H, t, $^3J = 7.8$ Hz, i-CH), 7.96 (1H, t, $^3J = 7.7$ Hz, m-CH), 7.90 (1H, d, $^3J = 7.7$ Hz, n-CH), 7.83 (1H, d, $^3J = 7.8$ Hz, j-CH), 7.61 (1H, d, $^3J = 7.8$ Hz, h-CH), 7.43 (1H, d, $^3J = 7.7$ Hz, l-CH), 4.95 (1H, d, $^2J = 15.8$ Hz, g'-CH), 4.17 (1H, d, $^2J = 15.8$ Hz, g-CH), 4.01 (1H, d, $^2J = 15.6$ Hz, b'-CH), 3.97 (1H, d, $^2J = 17.4$ Hz, k'-CH), 3.90 (1H, d, $^2J = 17.4$ Hz, k-CH), 3.77 (1H, ddd, c-CH), 3.66 (1H, dd, d-CH), 3.45 (1H, d, $^2J = 18.4$ Hz, a'-CH), 3.43–3.40 (1H, m, e-CH), 3.36–3.24 (2H, m, e'- and d'-CH), 3.27 (1H, d, $^2J = 15.6$ Hz, b-CH), 3.19 (1H, d, $^2J = 18.4$ Hz, a-CH), 3.10 (1H, ddd, f-CH), 2.80 (1H, d, $^2J = 12.9$ Hz, f'-CH), 2.65 (1H, dd, c'-CH). LR-ESI-MS (H_2O) 663.1 $[\text{C}_{22}\text{H}_{22}\text{LuN}_4\text{O}_9 + 2\text{H}]^+$, 661.1 $[\text{M}]^-$. HR-ESI-MS (H_2O) calcd for $[\text{C}_{22}\text{H}_{22}\text{LuN}_4\text{O}_9 + 2\text{H}]^+$, 663.0873; found $[\text{M} + 2\text{H}]^+$, 663.0946.



Chemical structure of $[\text{Lu}(\text{noneunpaX})]^-$ with ^1H NMR assignments indicated.

Na[In(noneunpaX)]. $\text{In}(\text{NO}_3)_3 \cdot \text{H}_2\text{O}$ (2.1 mg, 6.75 μmol , 1.0 equiv) was added directly to a solution of $\text{H}_4\text{noneunpaX} \cdot 4\text{HCl} \cdot 5\text{H}_2\text{O}$ (4.9 mg, 6.75 μmol , 1.0 equiv) in D_2O (300 μL). The solution was mixed thoroughly at 1000 rpm using a vortex mixer and the pD adjusted to ~ 4.5 using dilute NaOD solution to give $\text{Na}[\text{In}(\text{noneunpaX})]$. The solution was filtered and analyzed without additional purification. ^1H NMR (400 MHz, D_2O , 298 K, pD 5.5) 8.32 (2H, t, $^3J = 5.2$ Hz, i- and m-CH), 8.28 (2H, d, $^3J = 5.0$ Hz, j- and n-CH), 7.88 (2H, d, $^3J = 5.0$ Hz, h- and l-CH), 4.82 (2H, d, $^2J = 10.7$ Hz, g and k-CH₂), 4.28 (2H, d, $^2J = 10.7$ Hz, g'- and k'-CH₂), 3.74 (4H, s, a/a'- and b/b'-CH₂), 3.56 (4H, br s, d/d'- and e/e'-CH₂), 3.38 (2H, br s, f/f'-CH₂), 2.80 (2H, br s, c/c'-CH₂). LR-ESI-MS (H_2O) 603.0 $[\text{C}_{22}\text{H}_{22}\text{InN}_4\text{O}_9 + 2\text{H}]^+$, 625.0 $[\text{C}_{22}\text{H}_{22}\text{InN}_4\text{O}_9 + \text{H} + \text{Na}]^+$. HR-ESI-MS (H_2O) calcd for $[\text{C}_{22}\text{H}_{22}\text{InN}_4\text{O}_9 + 2\text{H}]^+$, 603.0506; found $[\text{M} + 2\text{H}]^+$, 603.0572.



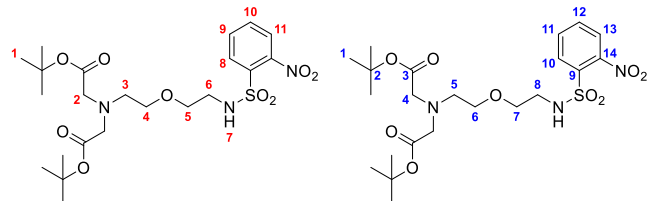
Chemical structure of $[\text{In}(\text{noneunpaX})]^-$ with ^1H NMR assignments indicated.

Solution Thermodynamic Stability Studies. All potentiometric titrations were carried out with a Metrohm Titrando 809 and a Metrohm Dosino 800 with a Ross combined electrode. A temperature-controlled (298 K) 20 mL glass cell with an inlet–outlet adapter for nitrogen gas purging (purified via a 10% NaOH solution to exclude CO_2 prior to and during each titration) was used as a titration cell. The electrode was calibrated daily in hydrogen ion concentration by direct titration of HCl with freshly prepared NaOH solution, and the results were analyzed with the Gran procedure⁶³ to determine the standard potential (E°) and the ionic product of water ($\text{p}K_w$), at 298 K, with 0.16 M NaCl as a supporting electrolyte. Solutions under study were titrated with carbonate-free NaOH solution (~ 0.16 M), which was standardized against freshly recrystallized potassium hydrogen phthalate. The experimental procedures for determination of the ligand protonation constants, complex formation, and pM values are found in the [Supporting Information](#).

Computational Studies. DFT calculations were performed using Gaussian 16 (revision B.01).⁴¹ Geometrical optimizations were performed with the hybrid PBE(0) exchange–correlation functional, which has shown excellent performance for modeling lanthanide coordination complexes in solution and was used previously to yield optimized geometries with comparable bond distances to experimentally obtained structures.^{64,65} Relatively small core quasi-relativistic effective core potentials (ECP28/60MWB) and their associated valence basis-sets were used for modeling metal ions (La^{3+} , Lu^{3+} , Bi^{3+}), while light atoms (C, H, N, O) were modeled up to Def2TZVP levels of theory.^{43–45} Initial geometries were generated using Avogadro (version 1.2.0) to provide input coordinates for calculations.⁶⁶ Solvation effects were modeled using the integrated equation formalism PCM for all metal complexes.⁴² Vibrational frequency analysis was carried out on the final optimized geometries to confirm that the obtained structures were true energy minima of the potential energy surface. NBO analysis was performed using NBO (version 3.1) within Gaussian 16.⁴⁹ Contour plots of the electron-density encompassing the 6s2 lone pair in $[\text{Bi}(\text{noneunpaX})]^-$ were generated using Multiwfn software.⁶⁷

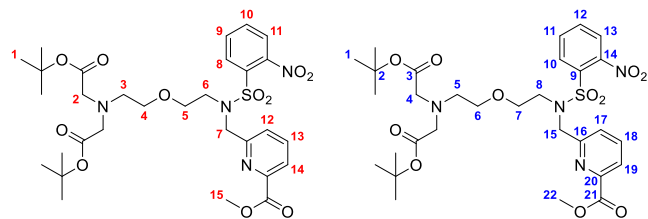
Bifunctional $\text{H}_4\text{noneunpaX}$ -Ph-NCS. Di-*tert*-Butyl 2,2'-((2-(2-(2-Nitrophenyl)sulfonamido)ethoxy)ethyl)azanediyl)diacetate (7). Di-*tert*-butyl 2,2'-((2-(2-Aminoethoxy)ethyl)azanediyl)diacetate (4) (2.35 g, 7.16 mmol) was dissolved in dry CH_2Cl_2 (40 mL) and cooled to 0 $^\circ\text{C}$. Triethylamine (2.00 mL, 1.45 g, 14.3 mmol, 2 equiv) was added to the reaction mixture, followed by slow addition of 2-nitrobenzenesulfonyl chloride (1.59 g, 7.16 mmol). The resulting pale-yellow solution was stirred at 0 $^\circ\text{C}$ for 1 h and then allowed to warm to RT and stirred for a further 5 h. The reaction mixture was then diluted with CH_2Cl_2 (40 mL) and extracted with deionized H_2O (2×50 mL) and brine (50 mL). The organic phase was evaporated in vacuo and the resulting residue purified via silica gel chromatography (CombiFlash Rf automated purification system; 80 g HP silica RediSep Gold cartridge; A: hexanes, B: EtOAc, 100% A to 40% B; product elution: 25% EtOAc). The title compound was attained as a pale-yellow oil (3.51 g, 96%). $R_f = 0.50$ (hexanes/EtOAc, 2:1, Si–Al TLC). ^1H NMR (400 MHz, CDCl_3 , 298 K) 8.14–8.12 (1H, m, 11-CH), 7.85–7.82 (1H, m, 9-CH), 7.75–7.70 (2H, m, 8- and 11-CH), 6.13 (1H, t, $^3J = 5.6$ Hz, 7-NH), 3.54–3.49 (4H, m, 4- and 5-CH₂),

3.45 (4H, s, 2-CH₂), 3.28 (2H, q, ³J = 5.5 Hz, 6-CH₂), 2.87 (2H, t, ³J = 5.6 Hz, 3-CH₂), 1.45 (18H, s, 1-C(CH₃)₃). ¹³C{¹H} NMR (100 MHz, CDCl₃, 298 K) 170.7 (3-C), 148.1 (14-C), 134.0 (9-C), 133.4 (11-C), 132.6 (12-C), 130.9 (13-C), 125.2 (10-C), 81.1 (2-C), 70.1 (7-C), 68.9 (6-C), 56.7 (4-C), 53.2 (5-C), 43.7 (8-C), 28.2 (1-C). ESI-MS (MeOH) 518.7 [C₂₂H₃₅N₃O₉S + H]⁺.



Compound (7) with ¹H and ¹³C NMR assignments, red and blue, respectively.

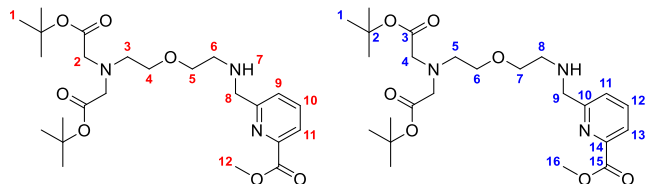
Di-tert-Butyl 2,2'-((2-((2-((6-methoxycarbonyl)pyridin-2-yl)methyl)-2-nitrophenyl)sulfonamido)ethoxy)ethyl)azanediyl diacetate (8). Methyl (6-bromomethyl) picolinate (884 mg, 3.84 mmol) was added to a solution of di-tert-butyl 2,2'-((2-((2-nitrophenyl)sulfonamido)ethoxy)ethyl)azanediyl diacetate (7) (1.98 g, 3.84 mmol) in dry MeCN (60 mL). The solution was stirred for 15 min at RT; K₂CO₃ (1.06 g, 7.68 mmol, 2.0 equiv) was then added and the resulting suspension heated at 50 °C overnight. The inorganic salts were then separated via centrifuge, washed with CH₂Cl₂ (3 × 10 mL), and the combined organic phase was evaporated in vacuo. The resulting residue was redissolved in CH₂Cl₂ (75 mL), washed with deionized H₂O (3 × 75 mL) and brine (75 mL), and dried over Na₂SO₄. The organic phase was evaporated in vacuo and the resulting residue purified via silica gel chromatography (CombiFlash R_f automated purification system; 40 g HP silica RediSep Gold cartridge; A: CH₂Cl₂, B: MeOH; 100% A to 5% B; product elution: 2% MeOH). The title product was attained as a pale-yellow oil (2.26 g, 88%). R_f = 0.30 (CH₂Cl₂/MeOH, 99:1, Si-Al TLC). ¹H NMR (400 MHz, CDCl₃, 298 K) 8.13–8.1 (1H, m, 11-CH), 7.98 (1H, d, ³J = 7.1 Hz, 14-CH), 7.81 (1H, t, ³J = 7.1 Hz, 13-CH), 7.68 (1H, d, ³J = 7.1 Hz, 12-CH), 7.66–7.62 (3H, m, 8-, 9- and 10-CH), 4.83 (2H, s, 7-CH₂), 3.95 (3H, s, 15-CH₃), 3.54 (2H, t, ³J = 5.3 Hz, 6-CH₂), 3.47 (2H, t, ³J = 5.3 Hz, 5-CH₂), 3.37 (4H, s, 2-CH₂), 3.35 (2H, t, ³J = 6.0 Hz, 4-CH₂), 2.71 (2H, ³J = 6.0 Hz, 3-CH₂), 1.41 (18H, s, 1-C(CH₃)₃). ¹³C{¹H} NMR (100 MHz, CDCl₃, 298 K) 170.6 (3-C), 165.4 (21-C), 157.4 (16-C), 148.1 (20-C), 147.4 (14-C), 137.9 (18-C), 133.5 (11-C), 133.4 (9-C), 131.8 (12-C), 131.0 (13-C), 125.4 (17-C), 124.3 (10-C), 124.0 (19-C), 80.9 (2-C), 70.0 (6-C), 68.6 (7-C), 56.5 (4-C), 53.9 (15-C), 53.3 (5-C), 52.8 (22-C), 48.1 (8-C), 28.1 (1-C). ESI-MS (MeOH) 667.3 [C₃₀H₄₂N₄O₁₁S + H]⁺.



Compound (8) with ¹H and ¹³C NMR assignments, red and blue, respectively.

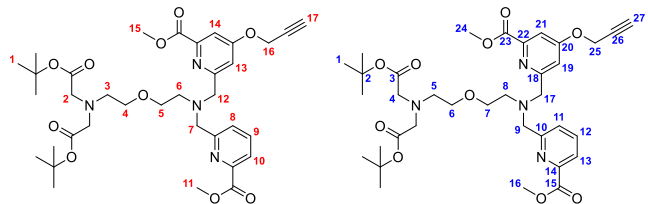
Di-tert-Butyl 2,2'-((2-((2-((6-methoxycarbonyl)pyridin-2-yl)methyl)amino)ethoxy)ethyl)azane-diyl diacetate (9). Thiophenol (1.05 mL, 10.2 mmol, 3.0 equiv) was added to a suspension of di-tert-butyl 2,2'-((2-((2-((6-methoxycarbonyl)pyridin-2-yl)methyl)-2-nitrophenyl)sulfonamido)ethoxy)-ethyl)azanediyl diacetate (8) (2.26 g, 3.39 mmol) and K₂CO₃ (937 mg, 6.78 mmol, 2.0 equiv) in dry MeCN (60 mL). The reaction mixture was heated to 50 °C and stirred for 2 h. The inorganic salts were then separated via centrifuge, washed with CH₂Cl₂ (3 × 10 mL), and the combined organic phase-evaporated in vacuo. The resulting residue was redissolved in CH₂Cl₂ (50 mL) and washed with deionized H₂O (2 × 50 mL) and brine (50 mL). The organic phase was evaporated in vacuo and the resulting oil purified via silica gel chromatography

(CombiFlash R_f automated purification system; 40 g HP silica RediSep Gold cartridge; A: CH₂Cl₂, B: MeOH; 100% A to 10% B; product elution: 5–8% MeOH) to give the title product as a pale-yellow oil (1.61 g, 98%). R_f = 0.20 (CH₂Cl₂/MeOH; 9:1). ¹H NMR (400 MHz, CDCl₃, 298 K) 8.00 (1H, d, ³J = 7.4 Hz, 11-CH), 7.81 (1H, t, ³J = 7.4 Hz, 10-CH), 7.66 (1H, d, ³J = 7.4 Hz, 9-CH), 4.05 (2H, s, 8-CH₂), 3.99 (3H, s, 12-CH₃), 3.61–3.56 (4H, m, 4- and 5-CH₂), 3.49 (4H, s, 2-CH₂), 2.94 (2H, t, ³J = 5.8 Hz, 6-CH₂), 2.83 (2H, t, ³J = 5.2 Hz, 3-CH₂), 2.26 (1H, br s, 7-NH), 1.44 (18H, s, 1-C(CH₃)₃). ¹³C{¹H} NMR (100 MHz, CDCl₃, 298 K) 170.6 (3-C), 165.4 (21-C), 157.4 (16-C), 148.1 (20-C), 147.4 (14-C), 137.9 (18-C), 133.5 (9-C), 133.4 (11-C), 131.8 (12-C), 131.0 (13-C), 125.4 (17-C), 124.3 (10-C), 124.0 (19-C), 80.9 (2-C), 70.0 (6-C), 68.6 (7-C), 56.5 (4-C), 53.9 (15-C), 53.3 (5-C), 52.8 (22-C), 48.1 (8-C), 28.1 (1-C). ESI-MS (MeOH) 482.2 [C₂₄H₃₉N₃O₇ + H]⁺.



Compound (9) with ¹H and ¹³C NMR assignments, red and blue, respectively.

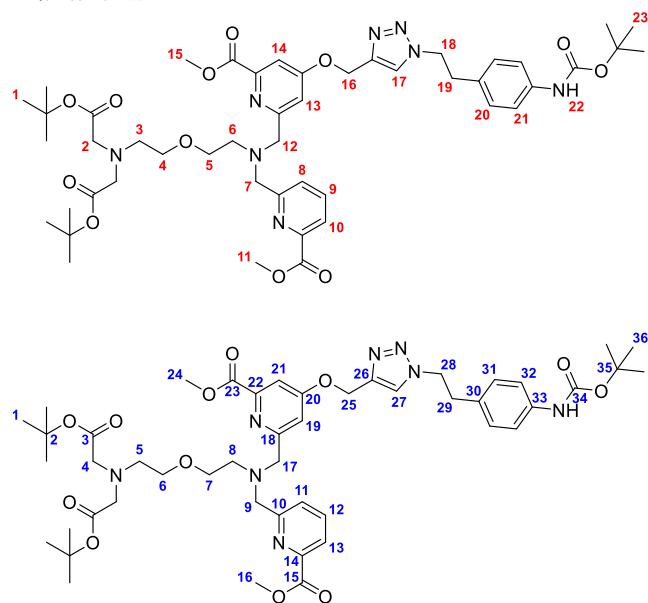
(^tBu)₂(Me)₂noneunpaX(OCH₂CCH) (10). Methyl 6-(bromomethyl)-4-(prop-2-yn-1-yloxy)picolinate (S3) (864 mg, 3.04 mmol) was added to a suspension of di-tert-butyl 2,2'-((2-((2-((6-methoxycarbonyl)pyridin-2-yl)methyl)amino)ethoxy)ethyl)azanediyl diacetate (1.46 g, 3.04 mmol) and DIPEA (1.06 mL, 784 mg, 6.06 mmol) in dry MeCN (30 mL). The reaction mixture was heated to 60 °C, stirred overnight, cooled to room temperature, and the volatiles removed in vacuo. The resulting residue was redissolved in CH₂Cl₂ (50 mL) and washed with deionized H₂O (2 × 50 mL) and brine (30 mL). The volatiles were removed in vacuo and the crude product purified via silica gel chromatography (CombiFlash R_f automated purification system; 24 g HP silica RediSep Gold cartridge; A: CH₂Cl₂, B: MeOH; 100% A to 10% B; product elution: 4% MeOH). The title product was attained as a pale-yellow oil (1.99 g, 95%). R_f = 0.60 (CH₂Cl₂/MeOH; 95:5). ¹H NMR (400 MHz, CDCl₃, 298 K) 7.98 (1H, dd, ³J = 7.5 Hz, ⁴J = 0.9 Hz, 10-CH), 7.88 (1H, d, ³J = 7.5 Hz, 8-CH), 7.78 (1H, t, ³J = 7.5 Hz, 9-CH), 7.59 (1H, d, ⁴J = 2.5 Hz, 14-CH), 7.52 (1H, br d, ⁴J = 2.5 Hz, 13-CH), 4.81 (2H, d, ⁴J = 2.4 Hz, 16-CH₂), 4.01 (2H, br s, 7-CH₂), 3.98 (3H, s, 11-CH₃), 3.97 (5H, br m, 12-CH₂ and 15-CH₃), 3.57 (2H, t, ³J = 5.5 Hz, 4-CH₂), 3.52 (2H, t, ³J = 5.9 Hz, 5-CH₂), 3.45 (4H, s, 2-CH₂), 2.91 (2H, t, ³J = 5.9 Hz, 6-CH₂), 2.81 (2H, t, ³J = 5.5 Hz, 3-CH₂), 2.60 (1H, t, ⁴J = 2.4 Hz, 17-CH), 1.42 (18H, s, 1-C(CH₃)₃). ¹³C{¹H} NMR (100 MHz, CDCl₃, 298 K) 170.7 (3-C), 165.8 (15-C), 165.7 (23-C), 165.1 (20-C), 162.6 (10-C), 160.6 (18-C), 148.9 (22-C), 147.3 (14-C), 137.4 (12-C), 126.1 (11-C), 123.6 (13-C), 111.8 (19-C), 111.0 (21-C), 80.8 (2-C), 77.1 (26-C), 76.9 (27-C), 70.4 (6-C), 69.3 (14-C), 60.8 (9-C), 60.6 (17-C), 56.6 (4-C), 55.9 (25-C), 54.0 (8-C), 53.5 (5-C), 53.0 (16-C), 52.9 (24-C), 28.1 (1-C). ESI-MS (MeOH) 685.3 [C₃₅H₄₈N₄O₁₀ + H]⁺.



Compound (10) with ¹H and ¹³C NMR assignments, red and blue, respectively.

(^tBu)₂(Me)₂noneunpaX(Ph-NHBoc) (11). A solution of Cu(OAc)₂·H₂O (66 mg, 0.329 mmol, 1.0 equiv) in deionized H₂O (1 mL) was added to a mixture containing (^tBu)₂(Me)₂noneunpaX(OCH₂CCH) (225 mg, 0.329 mmol) and *tert*-butyl (4-(2-azidoethyl)phenyl)-carbamate (86 mg, 0.329 mmol) in ^tBuOH (1 mL). Sodium ascorbate (65 mg, 0.329 mmol, 1.0 equiv) was added to the reaction mixture,

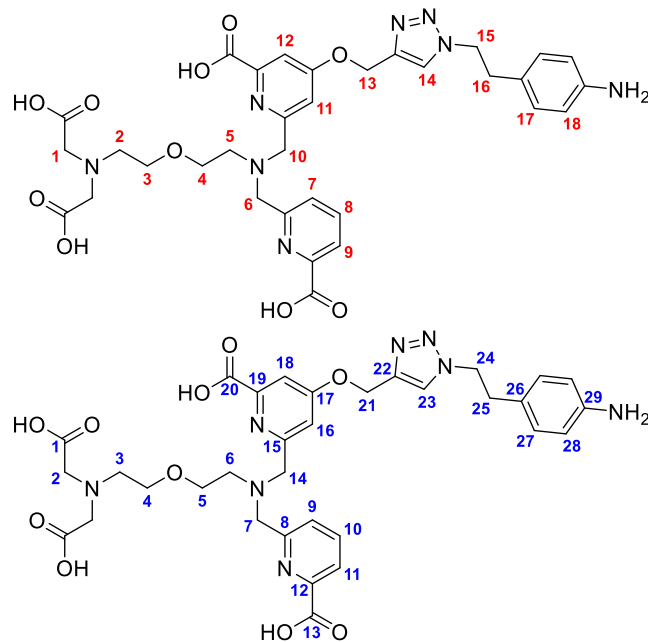
which darkened progressively over 10 min to give a red-brown solution. The solution was warmed to 40 °C and stirred for 48 h. The dark brown mixture was treated with a solution of Na₂S·9H₂O (790 mg, 3.29 mmol, 10 equiv) dissolved in deionized H₂O (4 mL). Black CuS precipitated immediately on addition, and the suspension was stirred for a further 1 h at RT. The precipitate was separated by centrifuge and the supernatant collected and evaporated under reduced pressure to remove excess ^tBuOH. The resulting aqueous phase was diluted with deionized H₂O (10 mL) and extracted with CH₂Cl₂ (3 × 15 mL). The combined organic phase was washed with deionized H₂O (10 mL) and brine (10 mL). The volatiles were removed in vacuo and the crude material purified via silica gel chromatography (CombiFlash R_f automated purification system; 12 g HP silica RediSep Gold cartridge; A: CH₂Cl₂, B: MeOH; 100% A to 15% B; product elution: 6.5% MeOH) to attain the title compound as a white fluffy solid (211 mg, 76%). R_f = 0.50 (CH₂Cl₂/MeOH; 9:1). ¹H NMR (400 MHz, CDCl₃, 298 K) 8.00 (1H, d, ³J = 7.5 Hz, 10-CH), 7.90 (1H, d, ³J = 7.5 Hz, 8-CH), 7.86 (1H, t, ³J = 7.5 Hz, 9-CH), 7.60 (1H, d, ⁴J = 2.2 Hz, 14-CH), 7.53 (1H, d, ⁴J = 2.2 Hz, 13-CH), 7.45 (1H, s, 17-CH), 7.27 (2H, d, ³J = 8.2 Hz, 21-CH), 6.98 (2H, d, ³J = 8.2 Hz, 20-CH), 6.66 (1H, br s, 22-NH), 5.28 (2H, s, 16-CH₂), 4.59 (2H, t, ³J = 7.1 Hz, 18-CH₂), 4.02 (2H, s, 12-CH₂), 3.99 (3H, s, 11-CH₃), 3.98 (3H, s, 15-CH₃), 3.96 (2H, s, 7-CH₂), 3.58 (2H, t, ³J = 5.6 Hz, 4-CH₂), 3.53 (2H, t, ³J = 5.8 Hz, 5-CH₂), 3.46 (4H, s, 2-CH₂), 3.17 (2H, t, ³J = 7.1 Hz, 19-CH₂), 2.91 (2H, t, ³J = 5.8 Hz, 6-CH₂), 2.81 (2H, t, ³J = 5.6 Hz, 3-CH₂), 1.52 (9H, s, 23-C(CH₃)₃), 1.43 (18H, s, 1-C(CH₃)₃). ¹³C{¹H} NMR (100 MHz, CDCl₃, 298 K) 170.7 (3-C), 165.8 (15-, 20- and 23-C), 162.6 (10-C), 160.6 (18-C), 152.9 (34-C), 148.9 (22-C), 147.3 (14-C), 142.2 (26-C), 137.6 (33-C), 137.5 (12-C), 131.2 (30-C), 129.2 (32-C), 126.3 (11-C), 123.8 (27-C), 123.6 (13-C), 118.9 (31-C), 111.9 (19-C), 111.1 (21-C), 80.9 (2-C), 80.5 (35-C), 70.4 (7-C), 69.3 (6-C), 61.9 (25-C), 60.8 (17-C), 60.6 (9-C), 56.6 (4-C), 54.0 (5-C), 53.5 (8-C), 53.0 (16-C), 52.9 (24-C), 51.9 (28-C), 36.0 (29-C), 28.3 (36-C), 28.2 (1-C). ESI-MS (MeOH) 947.5 [C₄₈H₆₆N₈O₁₂ + H]⁺.



Compound (11) with ¹H and ¹³C NMR assignments, red and blue, respectively.

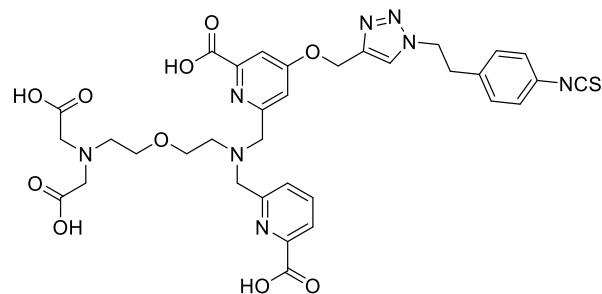
H₄noneunpaX-Ph-NH₂ (12). (tBu)₂(Me)₂noneunpaX(Ph-NHBoc) (200 mg, 0.211 mmol) was dissolved in 4 M HCl (3 mL) and heated at 60 °C overnight. Upon completion, the volatiles were evaporated in vacuo and the resulting residue purified via RP-HPLC (A: H₂O (0.1% TFA), B: MeCN; 95% A to 30% B over 40 min, R_t = 20.3–22.3 min). Purified H₄noneunpaX-triazole-Ph-NH₂ was coevaporated with 3 M HCl (3 × 2 mL) to give the corresponding HCl salt as a white solid (120 mg, 81%). ¹H NMR (400 MHz, D₂O, 298 K) 8.03 (1H, s, 14-CH), 7.94–7.83 (2H, m, 8- and 9-CH), 7.62 (1H, dd, ³J = 6.3 Hz, ⁴J = 2.0 Hz, 7-CH), 7.58 (1H, d, ⁴J = 2.7 Hz, 12-CH), 7.24 (1H, d, ⁴J = 2.7

Hz, 11-CH), 7.22 (2H, d, ³J = 7.4 Hz, 17-CH), 7.15 (2H, d, ³J = 7.4 Hz, 18-CH), 5.29 (2H, s, 13-CH₂), 4.74–4.65 (6H, m, 6-, 10- and 15-CH₂), 4.22 (4H, s, 1-CH₂), 3.97 (2H, t, 4-CH₂), 3.89 (2H, t, 3-CH₂), 3.76 (2H, t, 5-CH₂), 3.66 (2H, t, 2-CH₂), 3.23 (2H, t, 16-CH₂). ¹³C{¹H} NMR (100 MHz, D₂O, 298 K) 168.1 (17-C), 168.0 (1-C), 166.4 (13-C), 164.7 (20-C), 150.4 (8-C), 150.1 (15-C), 147.3 (12-C), 146.0 (19-C), 140.9 (22-C), 140.7 (10-C), 138.5 (29-C), 130.4 (27-C), 128.5 (26-C), 128.4 (9-C), 126.2 (23-C), 125.5 (11-C), 123.3 (28-C), 115.8 (16-C), 112.8 (18-C), 65.4 (5-C), 64.4 (4-C), 62.1 (21-C), 58.3 (7-C), 57.7 (14-C), 56.4 (3-C), 56.2 (6-C), 55.6 (2-C), 51.9 (24-C), 35.2 (25-C). LR-ESI-MS (H₂O) 707.6 [C₃₃H₃₈N₈O₁₀ + H]⁺.



H₄noneunpaX-Ph-NH₂ compound (12) with ¹H and ¹³C NMR assignments, red and blue, respectively.

H₄noneunpaX-Ph-NCS (13). Thiophosgene (120 μL, 1.56 mmol) in CHCl₃ (660 μL) was added to a solution of H₄noneunpaX-Ph-NH₂·4HCl (88 mg, 0.103 mmol) in deionized H₂O (1 mL). The biphasic mixture was stirred vigorously in the dark overnight at RT, after which the two immiscible layers were allowed to separate. The aqueous phase was collected, washed with CHCl₃ (2 × 1 mL), and then lyophilized to attain the crude isothiocyanate product. The off-white residue was purified via semipreparative RP-HPLC (A: H₂O (0.1%TFA), B: MeCN (0.1%TFA)): 0–6 min. (95% A to 24% B); 6–30 min. (24% B to 39% B); 30–35 min. (39% B to 100% B); R_t = 25.4 min. Appropriate fractions were pooled and lyophilized to give the purified product as an off-white aerated solid (67 mg, 87%). ESI-MS (H₂O/MeCN) 749.3 [C₃₄H₃₆N₈O₁₀S + H]⁺, 747.3 [C₃₄H₃₆N₈O₁₀ - H]⁻.



H₄noneunpaX-Ph-NCS compound (13).

Peptide Synthesis and Bioconjugation. Fmoc-Protected-Tyr³-TATE Derivatives. Fmoc-Ahx-Tyr³-TATE (16) and Fmoc-PEG₂-Tyr³-TATE (17) were prepared using a semiautomated peptide synthesizer (AAPPTec, Focus Xi) following standardized Fmoc-based SPPS methodology on Wang resin preloaded with Fmoc-Thr(tBu)-OH (substitution 0.68 mmol/g, 0.25 mmol). The resin-bound linear peptide was prepared according to the sequence: [D-Phe-Cys(ACM)-

Tyr(*t*Bu)-D-Trp(*t*Bu)-Lys(Boc)-Thr(*t*Bu)-Cys(ACM)-Thr(*t*Bu)-OH]. The preloaded resin was first swelled in DMF and then drained and dried under nitrogen prior to coupling of Fmoc- N_α -amino acids. N-terminus Fmoc group deprotection was achieved using 20% piperidine in DMF (15 mL) with mixing for 30 min, followed by washing with DMF, MeOH, and CH_2Cl_2 . Fmoc- N_α -protected amino acids (3 equiv) were preactivated separately using HBTU (3 equiv), HOBT (3 equiv), and DIPEA (6 equiv) in CH_2Cl_2 /DMF (1:4; 5 mL) 5 min prior to addition to the resin. Each coupling cycle followed a 2 h mixing cycle, with occasional nitrogen sparging, followed by washing with DMF, MeOH, and CH_2Cl_2 . Completion of each amino acid coupling was confirmed by a negative Kaiser test. After installation of the final Fmoc-protected amino acid, the N-terminus was deprotected as above, and either Fmoc-NH-Ahx- CO_2H or Fmoc-NH-PEG₂- CO_2H (3 equiv) was coupled to give the corresponding extended linear peptides. After preparation of the linear sequence, the resin-bound peptides were cyclized using I_2 (1 mg/mg resin) in DMF (10 mL) and stirred for 2 h at RT; the resin was then drained and washed with DMF (3×10 mL) and CH_2Cl_2 (3×10 mL) to remove traces of iodine. The cyclized peptide was cleaved from the resin using a standard cleavage cocktail consisting of TIPS (2.5%), deionized H_2O (2.5%), 1,2-ethanedithiol (2.5%), thioanisole (2.5%), and TFA (90%). The solution was stirred at RT for 3 h and filtered and the resin washed with DMF (1.5 mL). The filtrate was evaporated under a stream of N_2 to remove excess TFA and the resulting mixture divided into three equal aliquots (3×500 μL). The crude peptide was precipitated by dilution with diethyl ether (9.5 mL) and cooled to -70 $^\circ\text{C}$ for 1 h. The resulting white solid was separated by centrifuge (3500 rpm, 10 min), washed with diethyl ether (3×10 mL), and dried under a N_2 stream. The crude Fmoc-Ahx/PEG₂-Tyr³-TATE peptides were redissolved in H_2O (0.1% TFA)/MeCN (1:1) and purified via semipreparative RP-HPLC (A: H_2O (0.1% TFA), B: MeCN (0.1% TFA) (3 mL/min). Fmoc-Ahx-Tyr³-TATE (16) method: 0–6 min (95% A to 40% B); 6–25 min (40% B to 50% B); 25–30 min (50% B to 100% B); $R_t = 24.8$ min. Fmoc-PEG₂-Tyr³-TATE (17) method: 0–6 min (95% A to 40% B); 6–25 min (40% B to 48% B); 25–30 min (50% B to 100% B); $R_t = 22.8$ min. Appropriate fractions were pooled and lyophilized to give each peptide as a white powder. ESI-MS ($\text{H}_2\text{O}/\text{MeCN}$): Fmoc-Ahx-Tyr³-TATE 1384.4 $[\text{M} + \text{H}]^+$, 1382.7 $[\text{M} - \text{H}]^-$; Fmoc-PEG₂-Tyr³-TATE 1416.8 $[\text{M} + \text{H}]^+$, 1414.7 $[\text{M} - \text{H}]^-$.

Boc(Lys⁵)-Tyr³-TATE Derivatives. Di-*tert*-Butyl dicarbonate (34 mg, 0.156 mmol) was added to a solution containing Fmoc-Ahx-Tyr³-TATE (16) or Fmoc-PEG₂-Tyr³-TATE (17) dissolved in dry DMF (600 μL). The reaction mixtures were stirred vigorously for 10 min at RT before addition of DIPEA (10 μL , 0.057 mmol) and then kept under stirring for a further 4 h. Upon completion, the Fmoc-protected-Boc(Lys⁵)-Tyr³-TATE peptides were precipitated with diethyl ether (10 mL), cooled at -70 $^\circ\text{C}$ for 1 h, and separated via centrifuge (10 min, 3000 rpm). The crude peptides were then redissolved in dry DMF (500 μL), treated with 20% piperidine in DMF (1 mL), and stirred for 1 h. The deprotected Boc(Lys⁵)-Tyr³-TATE peptides were precipitated again with diethyl ether (10 mL), cooled for 1 h at -70 $^\circ\text{C}$, and isolated via centrifuge (10 min, 3000 rpm). The crude Boc(Lys)-Tyr³-TATE peptides were redissolved in H_2O (0.1% TFA)/MeCN (1:1) and purified via semipreparative RP-HPLC (A: H_2O (0.01% TFA), B: MeCN (3 mL/min). H_2N -Ahx-Boc(Lys⁵)-Tyr³-TATE (18) method: 0–6 min (95% A to 30% B); 6–30 min (30% B to 45% B); 30–35 min (45% B to 100% B); $R_t = 17.1$ min. H_2N -PEG₂-Boc(Lys⁵)-Tyr³-TATE (19) method: 0–6 min (95% A to 25% B); 6–25 min (25% B to 37% B); 25–30 min (37% B to 100% B); $R_t = 23.7$ min. Purified fractions were pooled and lyophilized to give the corresponding Boc(Lys⁵)-Tyr³-TATE derivatives (18 and 19). ESI-MS ($\text{H}_2\text{O}/\text{MeCN}$): H_2N -Ahx-Boc(Lys⁵)-Tyr³-TATE (18) 1262.9 $[\text{M} + \text{H}]^+$, 1260.8 $[\text{M} - \text{H}]^-$; H_2N -PEG₂-Boc(Lys⁵)-Tyr³-TATE (19) 1294.8 $[\text{M} + \text{H}]^+$, 1292.7 $[\text{M} - \text{H}]^-$.

H₄noneunpaX-Ahx-Tyr³-TATE. *H₄noneunpaX*-Ph-NCS (3.7 mg, 4.95 μmol) was added to a solution of H_2N -Ahx-Boc(Lys⁶)-Tyr³-TATE (6.3 mg, 4.95 μmol) in dry DMF (1 mL). The solution was stirred for 10 min at RT and then DIPEA (10 μL , 57 μmol) added. The resulting mixture was stirred O/N at RT and then treated with 20%

TFA in CH_2Cl_2 (1 mL) and stirred for a further 2 h. After completion, the volatiles were evaporated under a stream of N_2 gas and the resulting residue diluted with H_2O (0.1% TFA). The crude bioconjugate was purified via semipreparative RP-HPLC (A: H_2O (0.1% TFA), B: MeCN (0.1% TFA) (3 mL/min); method: 0–6 min (95% A to 29% B); 6–25 min (ISO 29% B); 25–30 min (29% B to 100% B); $R_t = 22.6$ min. Appropriate fractions were pooled and lyophilized to give *H₄noneunpaX-Ahx-Tyr³-TATE* as a white solid. ESI-MS ($\text{H}_2\text{O}/\text{MeCN}$ (1:1)) 1911.9 $[\text{M} + \text{H}]^+$.

H₄noneunpaX-PEG₂-Tyr³-TATE. *H₄noneunpaX*-Ph-NCS (2.3 mg, 3.07 μmol) was added to a solution of H_2N -PEG₂-Boc(Lys⁶)-Tyr³-TATE (4.0 mg, 3.07 μmol) in dry DMF (500 μL). The solution was stirred for 10 min at RT and then DIPEA (10 μL , 57 μmol) added. The resulting mixture was stirred O/N at RT and then treated with 20% TFA in CH_2Cl_2 (1 mL) and stirred for a further 2 h. The volatiles were evaporated under a stream of N_2 gas, and the resulting residue diluted with H_2O (0.1% TFA). The crude bioconjugate was purified via semipreparative RP-HPLC (A: H_2O (0.1% TFA), B: MeCN (0.1% TFA) (3 mL/min); method: 0–6 min (95% A to 29% B); 6–25 min (ISO 29% B); 25–30 min (29% B to 100% B); $R_t = 19.1$ min. Appropriate fractions were pooled and lyophilized to give *H₄noneunpaX-PEG₂-Tyr³-TATE* as a white solid. ESI-MS ($\text{H}_2\text{O}/\text{MeCN}$ (1:1)) 1943.3 $[\text{M} + \text{H}]^+$, 972.7 $[\text{M} + 2\text{H}]^{2+}$.

Radiochemistry. For concentration-dependent radiolabeling studies, the following protocol was applied for radiolabeling with different radiometal ions. Stock solutions of each respective chelating ligand were prepared in Ultrapure deionized H_2O at a concentration of 1×10^{-2} M. Serial dilution series for each chelator were prepared prior to radiolabeling studies, over a concentration range of 10^{-3} to 10^{-6} M. Aliquots (10 μL) of each stock solution were added to NaOAc (0.1 M), NH_4OAc (0.5 or 1.0 M), or MES buffer (1.0 M) (90 μL) to give sample reaction solutions. Aliquots (1–10 μL) of each respective radiolabel were added under the following conditions: [^{44}Sc]Sc³⁺ (1.2 MBq) in NaOAc (0.1 M, pH 4.5), [^{111}In]In³⁺ (1.0 MBq) in NH_4OAc (0.5 M, pH 5.8), [$^{132/135}\text{La}$]La³⁺ (400 kBq) in NH_4OAc (0.2 M, pH 7.0), [^{155}Tb]Tb³⁺ (40 kBq) in NH_4OAc (0.5 M, pH 6.0), [^{177}Lu]Lu³⁺ (150 kBq) in NH_4OAc (0.5 M, pH 6.0), [^{213}Bi]Bi³⁺ (680 kBq) in MES (1.0 M, pH 5.5), [^{225}Ac]Ac³⁺ (40 kBq) in NH_4OAc (1.0 M, pH 7.3). Reactions were carried out at RT and monitored over 10 min; [^{213}Bi]Bi³⁺ was monitored after 5 min within 10 min postgenerator elution ($n = 4–8$). Reactions with DOTA were carried out at elevated temperatures (85–90 $^\circ\text{C}$) and monitored over 30–60 min. RCYs were determined via iTLC using SA-paper plates and EDTA (50 mM, pH 5.0 or 7.0) as the eluent ($n = 4$). In the case of [^{213}Bi]Bi³⁺, RCYs were further confirmed through gamma spectroscopy measurements by analysis of the baseline and solvent front TLC peaks using a high-purity germanium (HPGe) detector and monitoring the 440 keV gamma emission line of ^{213}Bi . In all studies, separate control reactions were performed in parallel by addition of radioactivity to solutions containing buffer (90 μL) and deionized H_2O (10 μL). Radio-TLCs measurements were acquired to monitor for the formation of any hydroxo species under the stated conditions. Representative radio-TLC traces for each radiometal/radiolabeled compound are provided in Figures S113–S118. Radio-HPLC traces for the [^{111}In]In³⁺ and [^{155}Tb]Tb³⁺ radiolabeled complexes are provided in Figures S121–S123.

Human Serum Stability. For human serum stability measurements, samples of each radiolabeled complex or bioconjugate were prepared at high molar activity using the quantities given in Table S7. Radiolabeled complexes/bioconjugates were prepared by addition of each radionuclide (1–10 μL) to a solution of chelate/bioconjugate (0.5–1.0 μL , 1×10^{-3} M, 0.5–1.0 nmol) in the appropriate buffer (vide supra); $V_T = 100$ μL . Quantitative radiolabeling was confirmed by radio-TLC. The solutions were then divided into three equal aliquots (3×30 μL), diluted with pooled human serum (3×300 μL), and incubated at 37 $^\circ\text{C}$ for 5–7 days. The RCP was determined by iTLC using SA-paper plates and EDTA (50 mM, pH 5.5 or 7.0) as the eluent, whereby transchelated radioactivity migrates with the solvent front ($R_f = 1.0$) while intact metal complexes remain at the baseline (R_f

= 0). All studies were performed in triplicate and the average % RCP used for assessment of each compound.

Dose Escalation Studies. Dose escalation studies of [^{177}Lu][Lu-(noneunpaX-Ph-NH $_2$)] were carried out by sequential additions of H $_4$ noneunpaX-Ph-NH $_2$ (2–8 μL , 10^{-4} M, 20–80 pmol) to a solution containing [^{177}Lu][LuCl $_3$] (20 MBq) in NH $_4$ OAc buffer (40 μL , 0.5 M, pH 6.0). The reaction solution was allowed to stand for 10 min at RT between each addition, after which the RCY was determined by spotting 1 μL of solution onto SA-paper TLC plates and development with EDTA (50 mM, pH 5.5). Additional details are reported in Figure S120.

Log $D_{7.4}$ Measurements. Aliquots of [^{155}Tb]Tb $^{3+}$ or [^{225}Ac]Ac $^{3+}$ radiolabeled H $_4$ noneunpaX-Ahx-Tyr 3 -TATE or H $_4$ noneunpaX-PEG $_2$ -Tyr 3 -TATE (10 μL) were added to a biphasic mixture of *n*-octanol (700 μL) and PBS (700 μL , pH 7.4). The mixtures were vortexed for 2 min at RT and then separated via centrifuge (10 min, 3000 rpm). Aliquots of *n*-octanol (100 μL) and PBS (100 μL) were collected, and the activity in each portion determined via gamma spectroscopy. Log $D_{7.4}$ measurements were carried out with 5–6 replicates per radiotracer. The Log $D_{7.4}$ is defined as $\log_{10}[(n\text{-octanol phase})/(\text{buffer phase})]$.

Radiotracer Preparation. [^{155}Tb]Tb-noneunpaX-Ahx-Tyr 3 -TATE and [^{155}Tb]Tb-noneunpaX-PEG $_2$ -Tyr 3 -TATE were prepared with high molar activities (23.6 MBq/nmol and 22.5 MBq/nmol, respectively) suitable for in vivo SPECT/CT and biodistribution studies. An aliquot of [^{155}Tb]Tb $^{3+}$ (28 MBq, 40 μL) was added to a solution of H $_4$ noneunpaX-Ahx-Tyr 3 -TATE (6 μL , 2×10^{-3} M, 1.2 nmol) in NH $_4$ OAc buffer (10 μL , 0.5 M, pH 5.5). The pH was adjusted to neutral by addition of NaOH (1 M, 1 μL) and the resulting solution incubated at 37 $^\circ\text{C}$ for 15 min to ensure quantitative incorporation of radioactivity. The same radiolabeling protocol was applied to [^{155}Tb]Tb-noneunpaX-PEG $_2$ -Tyr 3 -TATE. Quality control measurements were performed via iTLC measurements and radio-HPLC; method: A: H $_2$ O (0.1% TFA), B: MeCN (0.1% TFA), 100% A to 60% B; 15 min, 1 mL/min, [^{155}Tb]Tb-noneunpaX-Ahx-Tyr 3 -TATE (t_R = 9.99 min, 99%), [^{155}Tb]Tb-noneunpaX-PEG $_2$ -Tyr 3 -TATE (t_R = 9.78 min, 96%). Radio-HPLC traces are shown in Figures S124 and S125. A small aliquot of each radiolabeled tracer was taken for quantification of radioactivity using gamma spectroscopy. No further purification was performed prior to administration of either radiotracer. Each of the radiolabeled bioconjugates was divided into two different stocks and diluted with PBS, to provide doses suitable for SPECT/CT imaging (10.2–13.5 MBq per subject) or biodistribution studies (~800 kBq per subject).

Tumor Implantation. Tumor implantation was performed at the BCCRC under the protocol approved by the Animal Care Committee (ACC) of the University of British Columbia (A20-0113). Male NRG mice were anesthetized by inhalation with 2% isoflurane in 2.0 L/min of oxygen and inoculated with a AR42J exocrine pancreatic tumor cell line, subcutaneously on the left shoulder. In vivo imaging and biodistribution studies were performed after tumor growth reached ~8–10 mm in diameter (2–3 weeks post inoculation).

Pre-Clinical SPECT/CT Imaging. Animal studies were performed in accordance with the Canadian Council on Animal Care (CCAC) using the protocol approved by the Animal Care Committee (ACC) of the University of British Columbia (A20-0132). Male NRG mice bearing AR42J exocrine pancreatic tumor xenografts were anesthetized with 5% isoflurane in an induction chamber and restrained in a Tail vein restrainer (Braintree Scientific) while under a continuous stream of 1–1.5% isoflurane. Mice were administered with either [^{155}Tb]Tb-noneunpaX-Ahx-Tyr 3 -TATE (10.2 MBq, 23.6 MBq/nmol) or [^{155}Tb]Tb-noneunpaX-PEG $_2$ -Tyr 3 -TATE (13.5 MBq, 22.5 MBq/nmol) in PBS (100 μL) via the lateral tail vein. Animal body temperature was maintained using a blanket on a heated bed, under continuous stream of 1.5–2% isoflurane, and the respiration rate monitored throughout the duration of each scan. Immediately following IV administration, whole-body SPECT/CT scans were acquired over the first 60 min using a multimodal VECTor/CT system (MILabs, Netherlands) with an XUHS 2 mm pinhole collimator. The mouse whole-body region was centered with a 14 mm axial field of

view and longitudinal imaging consisting of six frames of 10 min were acquired over the first 60 min, after which static SPECT/CT scans were recorded at 3, 5, and 24 h post injection using single frames of 20 min acquisitions. Energy windows centered on the 44, 85, and 106 keV photopeaks of ^{155}Tb were applied, with a spectral width of 25%. For quantitative analysis, the SPECT images were reconstructed using pixel-based ordered-subset expectation maximization reconstruction algorithm using a voxel size of 0.4 mm 3 , 16 subsets with 6 iterations (96 MLEM equivalent). SPECT scans were decay-corrected and attenuation factors applied based on CT acquisitions at each time-point.⁶⁸ A calibration factor relating (counts/voxel) to radioactivity concentration was previously determined by measurement of a known source of ^{155}Tb . Spherical volumes of interest (3 mm diameter) were drawn using AMIDE (v. 1.0.4) software to determine the pharmacokinetic profile of the tracer in target organs of interest. Mean standardized uptake values (SUV_{mean}) were subsequently extracted from the SPECT images. The standardized uptake value was defined according to the equation: $\text{SUV (g/mL)} = \text{radioactivity concentration (MBq/mL)} / [\text{administered dose (MBq)} / \text{body weight (g)}]$. Gaussian filtering (fwhm = 2 mm) and image rendering were carried out postreconstruction for data visualization purposes only.

Biodistribution Studies. Biodistribution studies with [^{155}Tb]Tb-noneunpaX-Ahx-Tyr 3 -TATE and [^{155}Tb]Tb-noneunpaX-PEG $_2$ -Tyr 3 -TATE were carried out in male NRG mice bearing AR42J exocrine pancreatic tumor xenografts. Prior to administration of each radiotracer (~800 kBq, 0.033 nmol) in PBS (~100 μL), mice were anesthetized by inhalation of 2% isoflurane and restrained using a tail vein restrainer (Braintree Scientific). Intravenous administration of each radiotracer occurred via the lateral tail vein. After administration, mice were allowed to roam freely in their cages and sacrificed at 5 or 24 h post injection by CO $_2$ asphyxiation under 2% isoflurane anesthesia. Cardiac puncture was performed immediately after sacrifice to recover blood, and organs of interest were collected, rinsed with PBS, and blotted dry. Each organ was weighed, and the radioactivity measured using a calibrated gamma counter (Packard Cobra II Autogamma counter, PerkinElmer, Waltham, MA, USA) with a 1 min acquisition time per sample. All radioactivity measurements were decay-corrected to the time of injection, and the injected dose per gram of tissue (% ID/g) calculated based on measured organ weights, with the exception of blood, bone, and muscle, which were scaled in accordance with literature values.⁶⁹

■ ASSOCIATED CONTENT

Supporting Information

The Supporting Information is available free of charge at <https://pubs.acs.org/doi/10.1021/acs.jmedchem.3c01151>.

Experimental synthetic and characterization details, NMR and mass spectral data, DFT-calculated structures and coordinates, radiochemistry, and in vivo SPECT/CT studies, biodistribution data (PDF)

Molecular formula strings (CSV)

■ AUTHOR INFORMATION

Corresponding Author

Chris Orvig – Medicinal Inorganic Chemistry Group,
Department of Chemistry, University of British Columbia,
Vancouver, British Columbia V6T 1Z1, Canada;
orcid.org/0000-0002-2830-5493; Email: orvig@chem.ubc.ca

Authors

Luke Wharton – Medicinal Inorganic Chemistry Group,
Department of Chemistry, University of British Columbia,
Vancouver, British Columbia V6T 1Z1, Canada; Life Sciences
Division, TRIUMF, Vancouver, British Columbia V6T 2A3,
Canada; orcid.org/0000-0002-0636-8741

Hua Yang – Life Sciences Division, TRIUMF, Vancouver, British Columbia V6T 2A3, Canada; Department of Chemistry, Simon Fraser University, Burnaby, British Columbia V5A 1S6, Canada; orcid.org/0000-0003-1833-9515

María de Guadalupe Jaraquemada-Peláez – Medicinal Inorganic Chemistry Group, Department of Chemistry, University of British Columbia, Vancouver, British Columbia V6T 1Z1, Canada; Molecular Oncology Group, British Columbia Cancer Research Centre (BCCRC), Vancouver, British Columbia V5Z 1L3, Canada; orcid.org/0000-0002-6204-707X

Helen Merkens – Molecular Oncology Group, British Columbia Cancer Research Centre (BCCRC), Vancouver, British Columbia V5Z 1L3, Canada

Gokce Engudar – Life Sciences Division, TRIUMF, Vancouver, British Columbia V6T 2A3, Canada

Aidan Ingham – Life Sciences Division, TRIUMF, Vancouver, British Columbia V6T 2A3, Canada

Helena Koniar – Life Sciences Division, TRIUMF, Vancouver, British Columbia V6T 2A3, Canada; Department of Physics and Astronomy, University of British Columbia, Vancouver, British Columbia V6T 1Z1, Canada

Valery Radchenko – Life Sciences Division, TRIUMF, Vancouver, British Columbia V6T 2A3, Canada; Department of Chemistry, University of British Columbia, Vancouver, British Columbia V6T 1Z1, Canada

Peter Kunz – Life Sciences Division, TRIUMF, Vancouver, British Columbia V6T 2A3, Canada

Paul Schaffer – Life Sciences Division, TRIUMF, Vancouver, British Columbia V6T 2A3, Canada; Department of Chemistry, Simon Fraser University, Burnaby, British Columbia V5A 1S6, Canada; Department of Radiology, University of British Columbia, Vancouver, British Columbia V5Z 1M9, Canada; orcid.org/0000-0002-6392-8792

François Bénard – Molecular Oncology Group, British Columbia Cancer Research Centre (BCCRC), Vancouver, British Columbia V5Z 1L3, Canada; Department of Radiology, University of British Columbia, Vancouver, British Columbia V5Z 1M9, Canada; orcid.org/0000-0001-7995-3581

Complete contact information is available at:
<https://pubs.acs.org/10.1021/acs.jmedchem.3c01151>

Author Contributions

The manuscript was written by L.W. with contributions from all authors. All authors contributed to the manuscript and approved the final version of the manuscript.

Notes

The authors declare the following competing financial interest(s): The authors, Dr. Luke Wharton and Dr. Chris Orvig, hold a patent application on H4noneunpaX.

ACKNOWLEDGMENTS

We thank the TR13 Operations Group, consisting of Toni Epp, Ryley Morgan, and Spencer Staiger and led by David Prevost, for irradiations of Ca and Ba targets. We are grateful to Maryam Osooly and Dr. Sathya Sekar for their assistance in performing SPECT/CT and biodistribution studies at the Centre for Comparative Medicine (CCM). We gratefully acknowledge the Natural Sciences and Engineering Research Council (NSERC) of Canada for a CREATE IsoSiM at TRIUMF research stipend

(L.W.). We acknowledge both NSERC and the Canadian Institutes of Health Research (CIHR) for financial support via a Collaborative Health Research Project (CHRP to P.S., F.B., C.O.) and NSERC Discovery (H.Y., V.R., P.S., C.O.). TRIUMF receives federal funding via a contribution agreement with the National Research Council of Canada. We thank WestGrid and Compute Canada for access to their computational resources and Canada Foundation for Innovation (project no. 24513) for its support of the imaging facility (<http://invivoimaging.ca>). C.O. dedicates this paper to the memory of John Hugh McNeill CM PhD FRSC (1938–2023) supportive mentor, brilliant collaborator, and dear friend.

ABBREVIATIONS

ACM, acetamido methyl; ADCs, antibody-drug conjugates; CN, coordination number; DFT, density functional theory; EA, elemental analysis; ECP, effective core potential; ESI, electrospray ionization; FDA, Food and Drug Administration; HPLC, high-performance liquid chromatography; MALDI, matrix-assisted laser desorption ionization; MIP, maximum intensity projection; MO, molecular orbital; MRI, magnetic resonance imaging; MS, mass spectrometry; NBO, natural bond orbital; NETs, neuroendocrine tumors; NMR, nuclear magnetic resonance; ox, oxinate; p.i., postinjection; pa, picolinate; PBE, Perdew–Burke–Ernzerhof; PCM, polarizability continuum model; PET, positron emission tomography; RCP, radiochemical purity; RCYs, radiochemical yields; ROI, region of interest; SPECT, single photon emission computed tomography; SPPS, solid phase peptide synthesis; SSTR2, somatostatin receptor subtype 2; SUV, standardized uptake value; TAT, targeted alpha therapy; TATE, Try³-octreotate; TLC, thin-layer chromatography

REFERENCES

- (1) Kostelnik, T. I.; Orvig, C. Radioactive Main Group and Rare Earth Metals for Imaging and Therapy. *Chem. Rev.* **2019**, *119* (2), 902–956.
- (2) Price, E. W.; Orvig, C. Matching Chelators to Radiometals for Radiopharmaceuticals. *Chem. Soc. Rev.* **2014**, *43* (1), 260–290.
- (3) Yang, H.; Zhang, C.; Yuan, Z.; Rodriguez-Rodriguez, C.; Robertson, A.; Radchenko, V.; Perron, R.; Gendron, D.; Causey, P.; Gao, F.; et al. Synthesis and Evaluation of a Macrocyclic Actinium-225 Chelator, Quality Control and In Vivo Evaluation of ²²⁵Ac-crown-αMSH Peptide. *Chem.—Eur. J.* **2020**, *26* (50), 11435–11440.
- (4) Wharton, L.; McNeil, S. W.; Merkens, H.; Yuan, Z.; Van de Voorde, M.; Engudar, G.; Ingham, A.; Koniar, H.; Rodriguez-Rodriguez, C.; Radchenko, V.; et al. Preclinical Evaluation of [155/161Tb]Tb-Crown-TATE—A Novel SPECT Imaging Theranostic Agent Targeting Neuroendocrine Tumours. *Molecules* **2023**, *28* (7), 3155.
- (5) Tripiet, R.; Tircsó, G.; Platas-Iglesias, C.; Harriswangler, C. Importance of Ligand Design in Lanthanide Azamacrocyclic Complexes Relevant to Biomedical Applications. *Handbook on the Physics and Chemistry of Rare Earths*; Elsevier Science, 2022; pp 129–220.
- (6) Thiele, N. A.; Macmillan, S. N.; Wilson, J. J. Rapid Dissolution of BaSO₄ by Macropa, an 18-Membered Macrocyclic with High Affinity for Ba²⁺. *J. Am. Chem. Soc.* **2018**, *140* (49), 17071–17078.
- (7) Hu, A.; MacMillan, S. N.; Wilson, J. J. Macrocyclic Ligands with an Unprecedented Size-Selectivity Pattern for the Lanthanide Ions. *J. Am. Chem. Soc.* **2020**, *142* (31), 13500–13506.
- (8) Thiele, N. A.; Woods, J. J.; Wilson, J. J. Implementing F-Block Metal Ions in Medicine: Tuning the Size Selectivity of Expanded Macrocycles. *Inorg. Chem.* **2019**, *58* (16), 10483–10500.

- (9) Hu, A.; Brown, V.; MacMillan, S. N.; Radchenko, V.; Yang, H.; Wharton, L.; Ramogida, C. F.; Wilson, J. J. Chelating the Alpha Therapy Radionuclides $^{225}\text{Ac}^{3+}$ and $^{213}\text{Bi}^{3+}$ with 18-Membered Macrocyclic Ligands MacroDipa and Py-MacroDipa $^{225}\text{Ac}^{3+}$ and $^{213}\text{Bi}^{3+}$ with 18-Membered Macrocyclic Ligands MacroDipa and Py-MacroDipa. *Inorg. Chem.* **2022**, *61* (2), 801–806.
- (10) Fiszbein, D. J.; Brown, V.; Thiele, N. A.; Woods, J. J.; Wharton, L.; MacMillan, S. N.; Radchenko, V.; Ramogida, C. F.; Wilson, J. J. Tuning the Kinetic Inertness of Bi^{3+} Complexes: The Impact of Donor Atoms on Diaza-18-Crown-6 Ligands as Chelators for ^{213}Bi Targeted Alpha Therapy ^{213}Bi Targeted Alpha Therapy. *Inorg. Chem.* **2021**, *60* (12), 9199–9211.
- (11) Hu, A.; Aluicio-Sarduy, E.; Brown, V.; MacMillan, S. N.; Becker, K. V.; Barnhart, T. E.; Radchenko, V.; Ramogida, C. F.; Engle, J. W.; Wilson, J. J. Py-MacroDipa: A Janus Chelator Capable of Binding Medicinally Relevant Rare-Earth Radiometals of Disparate Sizes. *J. Am. Chem. Soc.* **2021**, *143* (27), 10429–10440.
- (12) Abou, D. S.; Thiele, N. A.; Gutsche, N. T.; Villmer, A.; Zhang, H.; Woods, J. J.; Baidoo, K. E.; Escorcia, F. E.; Wilson, J. J.; Thorek, D. L. J. Towards the Stable Chelation of Radium for Biomedical Applications with an 18-Membered Macrocyclic Ligand. *Chem. Sci.* **2021**, *12* (10), 3733–3742.
- (13) Thiele, N. A.; Brown, V.; Kelly, J. M.; Amor-Coarasa, A.; Jermilova, U.; MacMillan, S. N.; Nikolopoulou, A.; Ponnala, S.; Ramogida, C. F.; Robertson, A. K. H.; et al. An Eighteen-Membered Macrocyclic Ligand for Actinium-225 Targeted Alpha Therapy. *Angew. Chem., Int. Ed.* **2017**, *56* (46), 14712–14717.
- (14) Cieslik, P.; Kubeil, M.; Zarschler, K.; Ullrich, M.; Brandt, F.; Anger, K.; Wadepohl, H.; Kopka, K.; Bachmann, M.; Pietzsch, J.; et al. Toward Personalized Medicine: One Chelator for Imaging and Therapy with Lutetium-177 and Actinium-225. *J. Am. Chem. Soc.* **2022**, *144* (47), 21555–21567.
- (15) Comba, P.; Jermilova, U.; Orvig, C.; Patrick, B. O.; Ramogida, C. F.; Rück, K.; Schneider, C.; Starke, M. Octadentate Picolinic Acid-Based Bispidine Ligand for Radiometal Ions. *Chem.—Eur. J.* **2017**, *23* (63), 15945–15956.
- (16) Price, E. W.; Cawthray, J. F.; Bailey, G. A.; Ferreira, C. L.; Boros, E.; Adam, M. J.; Orvig, C. H 4 Octapa: An Acyclic Chelator for 111 In Radiopharmaceuticals. *J. Am. Chem. Soc.* **2012**, *134* (20), 8670–8683.
- (17) Spreckelmeyer, S.; Ramogida, C. F.; Rousseau, J.; Arane, K.; Bratanovic, I.; Colpo, N.; Jermilova, U.; Dias, G. M.; Dude, I.; Jaraquemada-Peláez, M. d. G.; et al. P-NO 2 -Bn-H 4 Neunpa and H 4 Neunpa-Trastuzumab: Bifunctional Chelator for Radiometal pharmaceuticals and 111 In Immuno-Single Photon Emission Computed Tomography Imaging. *Bioconjugate Chem.* **2017**, *28* (8), 2145–2159.
- (18) Li, L.; Jaraquemada-Peláez, M. d. G.; Kuo, H.-T.; Merckens, H.; Choudhary, N.; Gitschtaler, K.; Jermilova, U.; Colpo, N.; Uribe-Munoz, C.; Radchenko, V.; et al. Functionally Versatile and Highly Stable Chelator for 111 In and 177 Lu: Proof-of-Principle Prostate-Specific Membrane Antigen Targeting. *Bioconjugate Chem.* **2019**, *30* (5), 1539–1553.
- (19) Wharton, L.; Kurakina, E.; Radchenko, V.; Schaffer, P.; Orvig, C. Chemical Promiscuity of Non-Macrocyclic Multidentate Chelating Ligands for Radiometal Ions: $\text{H}_4\text{Neunpa-NH}_2$ vs $\text{H}_4\text{Noneunpa}$. *Inorg. Chem.* **2021**, *60* (6), 4076–4092.
- (20) Wang, X.; Jaraquemada-Peláez, M. d. G.; Rodríguez-Rodríguez, C.; Cao, Y.; Buchwalder, C.; Choudhary, N.; Jermilova, U.; Ramogida, C. F.; Saatchi, K.; Häfeli, U. O.; et al. H 4 Octox: Versatile Bimodal Octadentate Acyclic Chelating Ligand for Medicinal Inorganic Chemistry. *J. Am. Chem. Soc.* **2018**, *140* (45), 15487–15500.
- (21) Southcott, L.; Wang, X.; Wharton, L.; Yang, H.; Radchenko, V.; Kubeil, M.; Stephan, H.; de Guadalupe Jaraquemada-Peláez, M.; Orvig, C. High Denticity Oxinate-Linear-Backbone Chelating Ligand for Diagnostic Radiometal Ions $[^{111}\text{In}]\text{In}^{3+}$ and $[^{89}\text{Zr}]\text{Zr}^{4+}$. *Dalton Trans.* **2021**, *50* (11), 3874–3886.
- (22) Price, E. W.; Zeglis, B. M.; Cawthray, J. F.; Ramogida, C. F.; Ramos, N.; Lewis, J. S.; Adam, M. J.; Orvig, C. H 4 Octapa-Trastuzumab: Versatile Acyclic Chelate System for 111 In and 177 Lu Imaging and Therapy. *J. Am. Chem. Soc.* **2013**, *135* (34), 12707–12721.
- (23) Kwekkeboom, D. J.; Kam, B. L.; van Essen, M.; Teunissen, J. J. M.; van Eijck, C. H. J.; Valkema, R.; de Jong, M.; de Herder, W. W.; Krenning, E. P. Somatostatin Receptor-Based Imaging and Therapy of Gastroenteropancreatic Neuroendocrine Tumors. *Endocr.-Relat. Cancer* **2010**, *17* (1), R53–R73.
- (24) Hennrich, U.; Kopka, K. Lutathera: The First FDA-and EMA-Approved Radiopharmaceutical for Peptide Receptor Radionuclide Therapy. *Pharmaceuticals* **2019**, *12*, 114.
- (25) Müller, C.; Van Der Meulen, N. P.; Benešová, M.; Schibli, R. Therapeutic Radiometals Beyond ^{177}Lu and ^{90}Y : Production and Application of Promising α -Particle, β^- -Particle, and Auger Electron Emitters. *J. Nucl. Med.* **2017**, *58*, 91S–96S.
- (26) Jaraquemada-Peláez, M. D. G.; Wang, X.; Clough, T. J.; Cao, Y.; Choudhary, N.; Emler, K.; Patrick, B. O.; Orvig, C. H 4 Octapa: Synthesis, Solution Equilibria and Complexes with Useful Radiopharmaceutical Metal Ions. *Dalton Trans.* **2017**, *46* (42), 14647–14658.
- (27) Hu, A.; Keresztes, I.; MacMillan, S. N.; Yang, Y.; Ding, E.; Zipfel, W. R.; DiStasio, R. A.; Babich, J. W.; Wilson, J. J. Oxyaapa: A Picolinate-Based Ligand with Five Oxygen Donors That Strongly Chelates Lanthanides. *Inorg. Chem.* **2020**, *59* (7), 5116–5132.
- (28) Jain, A. K.; Raut, R.; Tuli, J. K. Nuclear Data Sheets for A = 225. *Nucl. Data Sheets* **2009**, *110* (6), 1409–1472.
- (29) Shannon, R. D. Revised Effective Ionic Radii and Systematic Studies of Interatomic Distances in Halides and Chalcogenides. *Acta Crystallogr., Sect. A* **1976**, *32* (5), 751–767.
- (30) Deblonde, G. J. P.; Zavarin, M.; Kersting, A. B. The Coordination Properties and Ionic Radius of Actinium: A 120-Year-Old Enigma. *Coord. Chem. Rev.* **2021**, *446*, 214130.
- (31) Nica, N. Nuclear Data Sheets for A = 155. *Nucl. Data Sheets* **2019**, *160*, 1–404.
- (32) Webster, B.; Ivanov, P.; Russell, B.; Collins, S.; Stora, T.; Ramos, J. P.; Köster, U.; Robinson, A. P.; Read, D. Chemical Purification of Terbium-155 from Pseudo-Isobaric Impurities in a Mass Separated Source Produced at CERN. *Sci. Rep.* **2019**, *9* (1), 10884.
- (33) Müller, C.; Domnanich, K. A.; Umbricht, C. A.; van der Meulen, N. P. Scandium and Terbium Radionuclides for Radiotheranostics: Current State of Development towards Clinical Application. *Br. J. Radiol.* **2018**, *91* (1091), 20180074.
- (34) Naskar, N.; Lahiri, S. Theranostic Terbium Radioisotopes: Challenges in Production for Clinical Application. *Front. Med.* **2021**, *8*, 675014.
- (35) Gans, P.; Sabatini, A.; Vacca, A. Determination of Equilibrium Constants from Spectrophotometric Data Obtained from Solutions of Known PH: The Program PHAB. *Ann. Chim.* **1999**, *89*, 45–49.
- (36) Gans, P.; Sabatini, A.; Vacca, A. Investigation of Equilibria in Solution. Determination of Equilibrium Constants with the HYPERQUAD Suite of Programs. *Talanta* **1996**, *43* (10), 1739–1753.
- (37) Martell, A. E.; Smith, R. M. *Critical Stability Constants*; Springer US: Boston, MA, 1982.
- (38) Blachot, J. Nuclear Data Sheets for A = 111. *Nucl. Data Sheets* **2009**, *110* (6), 1239–1407.
- (39) Kurakina, E. S.; Wharton, L.; Hoehr, C.; Orvig, C.; Magomedbekov, E. P.; Filosofov, D.; Radchenko, V. Improved Separation Scheme for ^{44}Sc Produced by Irradiation of NatCa Targets with 12.8 MeV Protons. *Nucl. Med. Biol.* **2022**, *104–105*, 22–27.
- (40) Pujales-Paradela, R.; Rodríguez-Rodríguez, A.; Gayoso-Padula, A.; Brandariz, I.; Valencia, L.; Esteban-Gómez, D.; Platas-Iglesias, C. On the Consequences of the Stereochemical Activity of the $\text{Bi(III)} 6s^2$ Lone Pair in Cyclen-Based Complexes. The $[\text{Bi}(\text{DO3A})]$ Case. *Dalton Trans.* **2018**, *47* (39), 13830–13842.
- (41) Frisch, M. J.; Trucks, G. W.; Schlegel, H. B.; Scuseria, G. E.; Robb, M. A.; Cheeseman, J. R.; Scalmani, G.; Barone, V.; Petersson, G. A.; Nakatsuji, H.; et al. *Gaussian 16*, Rev. B.01; Gaussian, Inc.: Wallingford, CT, 2016.

- (42) Tomasi, J.; Mennucci, B.; Cammi, R. Quantum Mechanical Continuum Solvation Models. *Chem. Rev.* **2005**, *105* (8), 2999–3094.
- (43) Cao, X.; Dolg, M. Valence Basis Sets for Relativistic Energy-Consistent Small-Core Lanthanide Pseudopotentials. *J. Chem. Phys.* **2001**, *115* (16), 7348–7355.
- (44) Cao, X.; Dolg, M. Segmented Contraction Scheme for Small-Core Lanthanide Pseudopotential Basis Sets. *J. Mol. Struct.: THEOCHEM* **2002**, *581* (1–3), 139–147.
- (45) Stoll, H.; Metz, B.; Dolg, M. Relativistic Energy-Consistent Pseudopotentials? Recent Developments. *J. Comput. Chem.* **2002**, *23* (8), 767–778.
- (46) Horii, Y.; Damjanović, M.; Ajayakumar, M. R.; Katoh, K.; Kitagawa, Y.; Chibotaru, L.; Ungur, L.; Mas-Torrent, M.; Wernsdorfer, W.; Breedlove, B. K.; et al. Highly Oxidized States of Phthalocyaninato Terbium(III) Multiple-Decker Complexes Showing Structural Deformations, Biradical Properties and Decreases in Magnetic Anisotropy. *Chem.—Eur. J.* **2020**, *26* (39), 8621–8630.
- (47) Martynov, A. G.; Polovkova, M. A.; Gorbunova, Y. G.; Tsvadze, A. Redox-Triggered Switching of Conformational State in Triple-Decker Lanthanide Phthalocyaninates. *Molecules* **2022**, *27* (19), 6498.
- (48) Näslund, J.; Persson, I.; Sandström, M. Solvation of the Bismuth(III) Ion by Water, Dimethyl Sulfoxide, *N,N*′-Dimethylpropyleneurea, and *N,N*′-Dimethylthioformamide. An EXAFS, Large-Angle X-Ray Scattering, and Crystallographic Structural Study. *Inorg. Chem.* **2000**, *39* (18), 4012–4021.
- (49) Glendenning, E. D.; Reed, A. E.; Carpenter, J. E.; Weinhold, F. NBO 3.0; QCPE Bulletin, 1990, *10*, 58.
- (50) Wharton, L.; Jaraquemada-Peláez, M. d. G.; Zhang, C.; Zeisler, J.; Rodríguez-Rodríguez, C.; Osooly, M.; Radchenko, V.; Yang, H.; Lin, K.-S.; Bénard, F.; et al. H₄Picopa—Robust Chelate for ²²⁵Ac/¹¹¹In Theranostics. *Bioconjugate Chem.* **2022**, *33* (10), 1900–1921.
- (51) Wharton, L.; Zhang, C.; Zeisler, J.; Rodríguez-Rodríguez, C.; Osooly, M.; Radchenko, V.; Yang, H.; Lin, K.-S.; Bénard, F.; Schaffer, P.; et al. H₃TPAN-Triazole-Bn-NH₂: Tripicolinate Clicked-Bifunctional Chelate for [²²⁵Ac]/[¹¹¹In] Theranostics. *Bioconjugate Chem.* **2022**, *33*, 2381–2397.
- (52) Chong, H.-S.; Song, H. A.; Ma, X.; E. Milenic, D.; D. Brady, E.; Lim, S.; Lee, H.; Baidoo, K.; Cheng, D.; Brechbiel, M. W. Novel Bimodal Bifunctional Ligands for Radioimmunotherapy and Targeted MRI. *Bioconjugate Chem.* **2008**, *19* (7), 1439–1447.
- (53) Noor, A.; Van Zuylenkom, J. K.; Rudd, S. E.; Roselt, P. D.; Haskali, M. B.; Yan, E.; Wheatcroft, M.; Hicks, R. J.; Cullinane, C.; Donnelly, P. S. Imaging Somatostatin Positive Tumors with Tyr 3-Octreotate/Octreotide Conjugated to Desferrioxamine B Squaramide Radiolabeled with Either Zirconium-89 or Gallium-68. *Bioconjugate Chem.* **2021**, *32* (7), 1192–1203.
- (54) Borgna, F.; Barritt, P.; Grundler, P. V.; Talip, Z.; Cohrs, S.; Zeevaart, J. R.; Köster, U.; Schibli, R.; van der Meulen, N. P.; Müller, C. Simultaneous Visualization of ¹⁶¹Tb- and ¹⁷⁷Lu-Labeled Somatostatin Analogues Using Dual-Isotope SPECT Imaging. *Pharmaceutics* **2021**, *13* (4), 536.
- (55) Rousseau, E.; Lau, J.; Zhang, Z.; Uribe, C. F.; Kuo, H.-T.; Zhang, C.; Zeisler, J.; Colpo, N.; Lin, K.-S.; Bénard, F. Effects of adding an albumin binder chain on [¹⁷⁷Lu]Lu-DOTATATE/¹⁷⁷Lu]Lu-DOTA-TATE. *Nucl. Med. Biol.* **2018**, *66*, 10–17.
- (56) Müller, C.; Fischer, E.; Behe, M.; Köster, U.; Dorrer, H.; Reber, J.; Haller, S.; Cohrs, S.; Blanc, A.; Grünberg, J.; et al. Future Prospects for SPECT Imaging Using the Radiolanthanide Terbium-155—Production and Preclinical Evaluation in Tumor-Bearing Mice. *Nucl. Med. Biol.* **2014**, *41*, No. e58.
- (57) Roberts, M. S.; Magnusson, B. M.; Burczynski, F. J.; Weiss, M. Enterohaptic Circulation. *Clin. Pharmacokinet.* **2002**, *41* (10), 751–790.
- (58) Minor, G.; Kapalka, J.; Fisher, C.; Paley, W.; Chen, K.; Kinakin, M.; Earle, I.; Moss, B.; Bricault, P.; Gottberg, A. Remote Handling Systems for the ISAC and ARIEL High-Power Fission and Spallation ISOL Target Facilities at TRIUMF. *Nucl. Eng. Technol.* **2021**, *53* (4), 1378–1389.
- (59) Aluicio-Sarduy, E.; Hernandez, R.; Olson, A. P.; Barnhart, T. E.; Cai, W.; Ellison, P. A.; Engle, J. W. Production and in Vivo PET/CT Imaging of the Theranostic Pair ¹³²/135La. *Sci. Rep.* **2019**, *9* (1), 10658.
- (60) Ma, D.; McDevitt, M. R.; Finn, R. D.; Scheinberg, D. A. Breakthrough of ²²⁵Ac and its radionuclide daughters from an ²²⁵Ac/²¹³Bi generator: development of new methods, quantitative characterization, and implications for clinical use ²²⁵Ac and Its Radionuclide Daughters from an ²²⁵Ac/²¹³Bi Generator: Development of New Methods, Quantitative Characterization, and Implications for Clinical Use. *Appl. Radiat. Isot.* **2001**, *55* (5), 667–678.
- (61) Robertson, A. K. H.; McNeil, B. L.; Yang, H.; Gendron, D.; Perron, R.; Radchenko, V.; Zeisler, S.; Causey, P.; Schaffer, P. 232 Th Spallation-Produced ²²⁵Ac with Reduced ²²⁷Ac Content. *Inorg. Chem.* **2020**, *59* (17), 12156–12165.
- (62) Loening, A. M.; Gambhir, S. S. AMIDE: A Free Software Tool for Multimodality Medical Image Analysis. *Mol. Imaging* **2003**, *2* (3), 131–137.
- (63) Gran, G. Determination of the Equivalence Point in Potentiometric Titrations. Part II. *Analyst* **1952**, *77* (920), 661.
- (64) Huang, P. Understanding the Stability Trend Along Light Lanthanide Complexes with an Ehtylenediamine-Type Ligand: A Quantum Chemical Study. *ChemistrySelect* **2019**, *4* (42), 12368–12374.
- (65) Kovács, A.; Varga, Z. Metal-Ligand Interactions in Complexes of Cyclen-Based Ligands with Bi and Ac. *Struct. Chem.* **2021**, *32* (5), 1719–1731.
- (66) Hanwell, M. D.; Curtis, D. E.; Lonie, D. C.; Vandermeersch, T.; Zurek, E.; Hutchison, G. R. Avogadro: An Advanced Semantic Chemical Editor, Visualization, and Analysis Platform. *J. Cheminf.* **2012**, *4* (1), 17.
- (67) Lu, T.; Chen, F. Multiwfn: A Multifunctional Wavefunction Analyzer. *J. Comput. Chem.* **2012**, *33* (5), 580–592.
- (68) Branderhorst, W.; Vastenhouw, B.; Beekman, F. J. Pixel-Based Subsets for Rapid Multi-Pinhole SPECT Reconstruction. *Phys. Med. Biol.* **2010**, *55* (7), 2023–2034.
- (69) Foster, H. L.; Small, J. D.; Fox, J. G. *The Mouse in Biomedical Research*; Academic Press: New York, 1983.